ACSP · Analog Circuits And Signal Processing

Zhicheng Lin
Pui-In Mak (Elvis)
Rui Paulo Martins

Ultra-Low-Power and Ultra-Low-Cost Short-Range Wireless Receivers in Nanoscale CMOS

Springer

Analog Circuits and Signal Processing

Series editors

Mohammed Ismail, Dublin, USA
Mohamad Sawan, Montreal, Canada

More information about this series at http://www.springer.com/series/7381

Zhicheng Lin · Pui-In Mak (Elvis)
Rui Paulo Martins

Ultra-Low-Power and Ultra-Low-Cost Short-Range Wireless Receivers in Nanoscale CMOS

Springer

Zhicheng Lin
State-Key Laboratory of Analog and
Mixed-Signal VLSI and FST-ECE
University of Macau
Macao
China

Pui-In Mak (Elvis)
State-Key Laboratory of Analog and
Mixed-Signal VLSI and FST-ECE
University of Macau
Macao
China

Rui Paulo Martins
State-Key Laboratory of Analog and
Mixed-Signal VLSI and FST-ECE
University of Macau
Macao
China

and

Instituto Superior Técnico
Universidade de Lisboa
Lisbon
Portugal

ISSN 1872-082X ISSN 2197-1854 (electronic)
Analog Circuits and Signal Processing
ISBN 978-3-319-21523-5 ISBN 978-3-319-21524-2 (eBook)
DOI 10.1007/978-3-319-21524-2

Library of Congress Control Number: 2015944203

Springer Cham Heidelberg New York Dordrecht London

Printed on acid-free paper

Springer International Publishing AG Switzerland is part of Springer Science+Business Media (www.springer.com)

This book is dedicated
to our families

Preface

With the continued maturation of the Internet of things (IoT) for smart cities, a huge market has been opening up for short-range wireless communications, especially for ubiquitous wireless sensor networks (WSNs). It is expected that by 2020, the IoT market will be close to hundreds of billion dollars (annually $\sim$16 billions). These WSNs consist of spatial distribution of highly autonomous short-range radios to sense and collect the environmental data. The large number of units present in the network relaxes the sensitivity of a single receiver but, at the same time, demands ultra-low-power (ULP) and ultra-low-cost (ULC) radio chips to increase the density of elements and autonomous lifetime.

This book focuses on ULP and ULC receiver circuit techniques, and attempts to alleviate the trade-off between ULP and ULC. The rapid downscaling of CMOS offers sufficiently high f_T and low V_T favoring the design of ULP wireless receivers by: (1) cascading of radio frequency (RF) and baseband (BB) circuits under an ultra-low-voltage supply; (2) cascoding of RF and BB circuits in the current domain for current reuse. Based on these observations, two receivers according to the IEEE 802.15.4 (ZigBee/WPAN) standard have been designed, suitable for the worldwide available 2.4-GHz ISM band. Although current-reuse receivers can lead to power savings, they normally demand a high supply voltage and are optimized for narrowband only. To surmount this, by processing the RF and BB signals in an orthogonal approach, the third design is a function-reuse wideband-tunable receiver for sub-GHz multiple ISM bands. This is realized elegantly by employing an N-path passive mixer as the feedback path of the low-noise amplifier (LNA) to *concurrently* amplify the RF (common mode) and BB (differential mode) signals.

The described ULP and ULC architectures constitute attractive solutions for emerging WSNs suitable for different ISM bands. We hope you will enjoy reading this book.

Macao, China
May 2015

Zhicheng Lin
Pui-In Mak (Elvis)
Rui Paulo Martins

Contents

Abbreviations

BB	Baseband
Blixer	Balun-LNA-I/Q-Mixer
BPF	Bandpass Filter
BUF	Buffer
BW	Bandwidth
CG	Common Gate
CMOS	Complementary Metal–Oxide–Semiconductor
CoB	Chip-on-Board
CS	Common Source
DBM	Double-Balanced Mixer
DCB	Differential Current Balancer
DSB	Double Sideband
GB	Gain-Boosted
IB	In-Band
IF	Intermediate Frequency
IIP3	Input-Referred Third Order Interception Point
IM3	Third-Order Intermodulation
IoT	Internet of Things
IRR	Image Rejection Ratio
ISM	Industrial, Scientific and Medical
I/Q	In-Phase/Quadrature-Phase
LMV	LNA-Mixers-VCO
LNTA	Low-Noise Transconductance Amplifier
LO	Local Oscillator
LPF	Lowpass Filter
LPTV	Linear Periodically Time-Variant
NB	Narrowband
NF	Noise Figure
NTF	Noise Transfer Function
OB	Out-of-Band
PCB	Printed Circuit Board

PSD	Power Spectral Density
RF	Radio Frequency
RX	Receiver
SC	Switched Capacitor
SFDR	Spurious-Free Dynamic Range
SSB	Single Sideband
STF	Signal Transfer Function
TIA	Transimpedance Amplifier
ULC	Ultra-Low Cost
ULP	Ultra-Low Power
ULV	Ultra-Low Voltage
UWB	Ultra-Wide-Band
VCO	Voltage Controlled Oscillator
VGA	Variable-Gain Amplifier
WPAN	Wireless Personal Area Network
WSN	Wireless Sensor Networks

Chapter 1
Introduction

The immense scope of Internet of Things (IoT) potentiates huge market opportunities for short-range wireless connectivity. To achieve this, it is highly desirable to use ultra-low-power (ULP) and ultra-low-cost (ULC) short-range radios. Nevertheless, ULP and ULC are a fundamental trade-off between each other. This book attempts to develop advanced circuit techniques alleviating or decoupling such trade-off, especially in the design of RF and analog front-ends. In Sect. 1.1, a brief definition of short-range wireless communications is presented. Several short-range wireless standards are studied. Section 1.2 discusses the system-level design considerations of ULP and ULC short-range wireless receivers (RXs), including the supply voltage, carrier frequency and signal bandwidth.

1.1 Short-Range Wireless Communications

Here, short-range communication systems are categorized according to different scenarios, technologies and requirements. Although there is no formal definition of such short-range systems, they can always be classified according to their targeted coverage ranges [1]. According to [1, 2], short-range wireless communications are defined as the systems providing wireless connectivity within a local sphere of interaction. It involves transfer of information from millimeters to a few hundreds of meters. According to the operating range, a convenient way to classify short-range operation is shown in Fig. 1.1. It includes Near Field Communications (NFC) for very close connectivity (range in the order of millimeters to centimeters), Radio Frequency Identification (RFID) ranging from centimeters up to a few hundred meters, Wireless Body Area Networks (WBAN) providing wireless access in the close vicinity of a person, a few meters typically, Wireless Personal Area Networks (WPAN) serving users in their surroundings of up to ten meters or similar, Wireless Local Area Networks (WLAN), provide local connectivity for indoor scenario covering typically up to hundred meters around the access point, Bluetooth Low Energy (BLE) for mobile phones, personal computers, watches etc. and Wireless Sensor Networks (WSN), reaching even further [1].

Z. Lin et al., *Ultra-Low-Power and Ultra-Low-Cost Short-Range Wireless Receivers in Nanoscale CMOS*, Analog Circuits and Signal Processing,
DOI 10.1007/978-3-319-21524-2_1

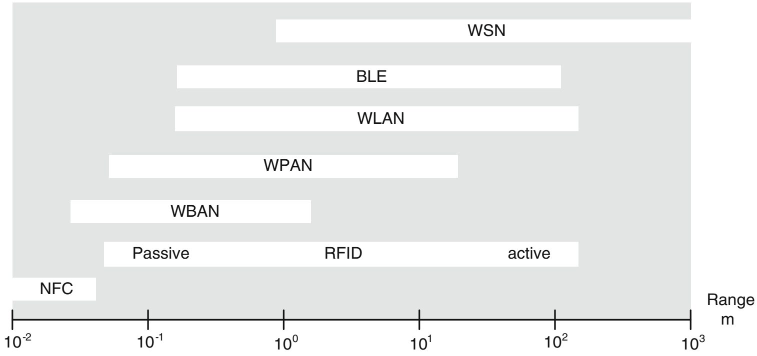

Fig. 1.1 Short-range communication systems and their operation ranges

All aforesaid short-range wireless communication systems have their own specifications such as data throughput, power consumption and operation range to meet the requirements of different applications. As a result, different preferred frequency bands are defined, required bandwidth, and transmitted power. A number of short-range wireless communication standards have been developed in the last decade, and even more in recent years, to cover all possible short-range applications. Here, three popular short-range wireless standards for ULP applications are reviewed.

1.1.1 The IEEE 802.15.4/ZigBee, IEEE 802.15.6 and Bluetooth Low Energy ULP Standards

Applications such as wireless health/fitness sensors, smart tags, home/office automation and low-duty-cycle machine-to-machine M2M communications etc., require ULP and ULC radios. When compared with the Bluetooth (Version 1), Enhanced Data Rate Bluetooth (EDR: Version 2) and IEEE 802.15.3 (HR-WPAN), the IEEE 802.15.4/ZigBee, IEEE 802.15.6 and Bluetooth Low Energy (BLE) Standards exhibit much lower peak power and average power consumption, which render them more suitable for ULP applications. Their features are briefly described next. For more details, the readers are referred to [3–12].

The IEEE 802.15.4/ZigBee Standard—The IEEE 802.15.4/ZigBee (LR-WPAN) emerged in the end of 2000 and was completely released in 2003. It is a low-rate WPAN (LR-WPAN) standard optimized for low data rate and low-power applications. The IEEE 802.15.4 defines the Physical (PHY) layer and Media Access Control (MAC) layer. It is tailored to operate at a very low duty cycle (<1 %) for low power consumption and covers three different frequency bands. While for the upper network layers, they are defined and supported by ZigBee alliance. For ZigBee, its routing protocol is designed to run over 802.15.4 [3]. For the three bands supported by IEEE 802.15.4/ZigBee, the first band is located at 868 MHz with only one channel. It supports 20 kbps bit rate using binary phase-shift keying (BPSK) modulation. This band is adopted in Europe only. The second band is located at 915 MHz. It has 10 channels, each of which supports 40 kbps using BPSK modulation. This band is adopted in North America, Australia, New Zealand, and some countries in South America [4]. The third frequency band is located at 2.4 GHz, it has a total of 16 channels with 250 kbps each. Unlike the previous two bands, the third band exploits offset quadrature phase-shift keying (OQPSK) with half sine-wave shaping as its modulation scheme. This results in a minimum-shift keying (MSK) signal. Its unlicensed frequency allocation is available worldwide [5]. Beyond these three bands, the IEEE 802.15.4c study group considered newly opened 314–316, 430–434, and 779–787 MHz bands to be adopted in China, while the IEEE 802.15 Task Group 4d defined an amendment to the standard version of 802.15.4-2006 to support the new 950–956 MHz band in Japan. First standard amendments by these groups have been released in April 2009.

IEEE 802.15.6 Standard—The IEEE 802.15.6 working group was formed in 2008 to develop an international standard for short-range (i.e., human body range), low power and highly reliable wireless communications for use in the close proximity to, or inside, the human body. The resulting standard IEEE 802.15.6 for WBAN was ratified in February 2012 [6]. It defines new PHY and MAC layers. The defined three PHY layers are [7, 8]: (1) narrow band (NB) PHY, which is optimized for ULP WBAN applications. It utilizes differential binary phase-shift keying (DBPSK), differential quadrature phase-shift keying (DQPSK), and differential 8-phase-shift keying (D8PSK) modulation techniques, except 420–450 MHz which uses the Gaussian minimum-shift keying (GMSK) technique; (2) ultra wide band (UWB) PHY, for higher data rate entertainment applications. It operates in two frequency bands: low and high bands. Each band is sub-divided into channels, all of them characterized by a bandwidth of 499.2 MHz; (3) human body communications (HBC) PHY, which utilizes the human body as the channel. HBC PHY operates in two frequency bands centered at 16 and 27 MHz, with a bandwidth of 4 MHz.

Bluetooth Low Energy (BLE)—BLE is a prospective short-range wireless specification that appeared in the market, having been ratified at the end of 2009. Although written by the Bluetooth Special Interest Group, it is a fundamentally different radio standard from the Bluetooth (Version 1), Enhanced Data Rate Bluetooth (EDR: Version 2), both in terms of how it works and the applications it will enable. By itself, BLE is a completely new radio and protocol stack. It was adopted towards the backend of 2010 [9].

BLE supports 40 channels in the 2.4 GHz band, each of which is 2 MHz wide. It is based on Gaussian frequency-shift keying (GFSK) for modulation with an index of 0.5, which relaxes and helps to increase the operating range when compared with Bluetooth EDR. The overall radio-frequency (RF) specification is similar to that of other ULP proprietary radios.

The basic tenets of BLE for low power consumption are summarized as follows [9]: (1) it exploits small packet size standards for intermittent events, thus, it does not efficiently transfer large amounts of data; (2) it uses an autonomous controller to extract as much as possible from the devices, allowing them to stay asleep for power savings; (3) low duty-cycle operation and small latency are adopted and optimized to lower the power consumption; (4) at the two ends of the link, the slave and master devices are asymmetric, which allows the use of very simple low-power devices.

In summary, when compared with IEEE 802.15.6, BLE has a modest advantage in terms of power consumption for episodic data transmission and market penetration. For the former, it is partly due to its simpler-to-implement amplitude modulation (AM) free GFSK modulation. While for the later, it is primarily due to the huge success of Bluetooth in the mobile platforms. Yet, the PHY of IEEE 802.15.6 has specific advantages over BLE in medical WBANS: (1) it can utilize multiple frequency bands, e.g. the sub-GHz industrial, scientific and medical (ISM) bands, while BLE only works in 2.4 GHz ISM band, in particular the quiet medical body area networks (MBANs) spectrum allocated to medical devices only in the U.S. from 2.36 to 2.4 GHz; (2) it has more RF channels available; (3) it has significant higher data throughput and better range/link budget at the same output power and data rate [8].

The differences between BLE and ZigBee are: (1) from the market perspective, ZigBee is more mature and has gone through some iterations with market mindshare. Regrettably, it does not have as many shipments as Bluetooth [10]; (2) from the network perspective, BLE is designed for ULP PAN/BAN (Personal Area Network/Body Area Network), with a simple star network topology. Differently, ZigBee is more for low-power LAN (Local Area Network), supporting mesh networking. Thus, ZigBee can cover a large network area with flexible routing, making it suitable for relatively stationary networks [11, 12]; (3) from power consumption perspective, BLE uses a synchronous connection, which implies that both master and slave wake up synchronously. This helps lowering the power on both sides. ZigBee, however, is based on an asynchronous scheme, meaning that the routers stay awake all the time and thus its power is relatively high. The end-nodes can wake up at any time to send their data for power savings.

Overall, the above three standards have their pros and cons. To best-suit the market and applications, multi-standard ULP TRXs seems more prospective for the future. The dual-mode MBAN/BLE TRX in [8] is an example. It achieves a power consumption of 6.5 mW in RX and 5.9 mW in TX. Another example [13] is the BLE/ZigBee/IEEE 802.15.6 for personal/body-area network that supports three modes. It consumes 3.8 mW in RX and 5.4/4.6 mW in TX. For the RX path, both work in the 2.4 GHz ISM band and are shared between different modes. The RX specifications such as NF, IIP3 and IRR are similar for different modes. Thus, this book will focus on the RX-path circuit techniques and will target only the ZigBee as the reference standard for demonstration.

1.2 Design Considerations for ULP and ULC Short-Range Wireless RXs

Here, the supply voltage, the carrier frequency and the selection of narrow band (NB) versus ultra-wide-band (UWB) will be considered.

1.2.1 Power Supply (V_{DD})

Short-range TRXs should run preferably from a tiny battery, thus sub-2V supply voltages are highly desired. Radio TRXs that work down to 1.2 V allow additional flexibility in sensors' design and reduce the power management constraints [14]. Besides, low peak current consumption and V_{DD} also benefit wireless sensors that run from harvested energy sources which will enhance flexibility, simplify the design and extend the applications. For example, on-chip solar cells only can provide an output voltage between 200 and 900 mV, while thermoelectric generators exhibit an even lower supply voltage (50–300 mV) [15]. Although boost converters can be employed to boost up the output voltage, their efficiency is limited. For example, the peak efficiency of the boost converters in [16–19] has a maximum of 75 % only. The minimum input voltage range is from 20 to 330 mV. Besides, a low peak current consumption will benefit the design of power management circuitry. Furthermore, radio operating at higher voltage is only required when a higher output power is entailed. This is not the case for short-range applications, as the output power rarely exceeds 0 dBm. Thus, low supply voltage is revealed as a simple way to reduce the power consumption at the system level. There are many RXs/TRXs [20–22] that were designed in this way, and their corresponding techniques will be reviewed in Chap. 2–5.

In a low V_{DD} design, however, due to the limited dynamic range, for the given parameters such as third-order intercept point (IIP3), noise-figure (NF), gain etc., the current should be larger than that with a high V_{DD}. For example, for the given NF requirement, the current-reuse P-type metal-oxide-semiconductor (PMOS) and N-type metal-oxide-semiconductor (NMOS) self-biased amplifier with a V_{DD} of 1 V consumes half of the current of a single NMOS (or PMOS) without current-reuse and with a V_{DD} of 0.5 V. This constraint is even tighter if a small chip area and/or no/limited external components are imposed for ULC purposes. As an example, inductors can help to boost the speed and bias the circuit with lower voltage headroom consumption and noise. If they must be avoided for area savings, only resistors or transistors can be adopted. This imposes a hard trade-off with IIP3, NF and bandwidth (BW). Thus, to balance the supply voltage, current, area and external components with the key performance metrics (NF and out-of-band (OB) IIP3), effective circuit innovations for the RX design are highly demanded.

1.2.2 Carrier Frequency

The 2.4 GHz ISM band is available worldwide. For the sub-GHz ISM bands, they are composed by a number of bands for different countries. Thus, a radio either supports the single 2.4 GHz ISM band or the sub-GHz multi-ISM band of interest. The factors to be considered can be listed as follows:

Range and signal lost—As an electromagnetic wave (i.e. the radio wave) propagates through space, it will be attenuated or weakened in terms of signal power, this is commonly known as path loss. This can be induced by reflection, diffraction or absorption etc., and it can be calculated using the formula [23, 24]

$$L = 10n \log_{10}(d) + C \tag{1.1}$$

where L is the path loss in decibels, n is the path loss exponent, d is the distance between the transmitter and the receiver and C is a constant which accounts for system losses. Here, n accounts for the influence of different environments for path loss. For example, in the free space, $n = 2$ while for some indoor environments, it can increase to a value from 4 to 6. Thus, in highly congested environments, the 2.4 GHz transmission can weaken rapidly, which adversely affects signal quality. To quantify the influence of frequency on path loss, we can use the simplified Friis transmission equation [23, 24]

$$L = 20\log_{10}\left(\frac{4\pi d}{\lambda}\right) \tag{1.2}$$

where L is the path loss in decibels, λ is the wavelength and d the transmitter-receiver distance. Obviously, the path loss increases with frequency. Hence, the 2.4 GHz signal should weaken faster than others in the sub-GHz range. As an example, it can be calculated that the path loss at 2.4 GHz is 8.5 dB higher than that at 900 MHz. This translates into a 2.67 times longer range for a 900 MHz radio. Since the range approximately doubles with every 6 dB increase in power (from Eq. (1.1) for free space), a 2.4 GHz solution will need an increment of power budget (by 8.5 dB), in order to match the range of a 900 MHz radio. Besides, in a human environment like in WBAN applications, biological tissues absorb RF energy as a function of frequency. Lower frequencies can penetrate the body easily without being absorbed, meaning a better RF link or less power consumption for a sub-GHz link when compared to 2.4 GHz [25].

Interference—The 2.4 GHz ISM band has a high chance to come across interferences as discussed in Sect. 1.1 due to the co-existence in this band of many wireless standards, which will reduce the communication reliability. As an example, the IEEE 802.11 (WiFi) can transmit an output power 10–100 times higher than the ZigBee. Signals from Bluetooth-enabled computer, cell phone peripherals and microwave ovens can also be considered as “jammers” for BLE and IEEE 802.15.6/WBAN, which have a much lower output power. Sub-GHz ISM bands are mostly used for proprietary low-duty-cycle links and are not as likely to interfere with each other. A quieter spectrum means easier transmissions and fewer retries, which is more efficient to save the battery power.

Antenna size—Range, low interference and low power consumption are the basic advantages of sub-GHz applications over its 2.4 GHz counterpart. One disadvantage of sub-GHz operation is the larger antenna size since many antenna types are designed to be resonant at their intended operation frequency. The advantage of an antenna at resonance is that it presents a pure resistance to the feed line that connects to the transmitter or receiver [26]. While off resonance it will present a reactance, such as a capacitance or an inductance, influencing input impedance matching and the maximum power transfer. Since the antenna size is inversely proportional to the frequency, a small node size would have the highest priority, being the 2.4 GHz more appropriate.

1.2.3 NB Versus UWB

Narrow-band ULP TRXs are usually operated in the 2.4 GHz or sub-GHz ISM bands and implemented according to well-known standards such as ZigBee [22, 27–29], Bluetooth low energy [8, 13–31] or IEEE 802.15.6 [8, 13, 25]. They are tolerant to interference, and hence inter-operability is possible with other services due to the complex baseband channel-selection filter. Moreover, such TRXs can connect easily to the existing handheld terminals, providing a second dimension of autonomy, apart from the battery lifetime. Additionally, the link layer, such as BLE, supports advanced encryption standard (AES) and key exchange algorithms to protect the highly sensitive personal data from unauthorized access.

Wide-band super-regenerative receivers [32–36] are promising in terms of power consumption. Yet, they occupy a much larger bandwidth than absolutely necessary for their respective data rates and are prone to interference. On the other hand, the impulse-radio ultra wide-band (IR-UWB) transceivers transmit extremely short RF pulses, and hence occupy a larger bandwidth, in the order of several GHz [37–45]. Both super-regenerative receivers and IR-UWB provide a low to moderate link budget.

1.3 Main Targets

Typically, the power budget of short-range wireless systems is dominated by the wireless link. Hence many efforts have been directed toward the implementation of power efficient TRXs in the last decade [11]. Unlike the designs in [32–47], where proprietary wireless are employed to achieve power efficiency for energy-per-bit with less spectral inefficiency, the objective of this book is to reduce the power consumption for NB receivers (see Sect. 1.2.3), with 802.15.4/ZigBee as the reference standard (see Sect. 1.1). The methodology to reduce the power consumption is focused on the design and optimization at the circuit level. Also, low cost is an important factor when designing short-range systems. For the specifications imposed by this standard, like the blocking requirements, operation frequency and sensitivity requirements, etc., which have been well studied in [27, 28], in this book those specifications are followed and there will be a special focus, simultaneously, on ULP and ULC implementation. A special attention is paid to a single low-V_{DD} design in Chap. 5 in order to incorporate it with future alternative harvesting energy sources. Two target ISM bands were implemented, one for 2.4 GHz and another for sub-GHz multi-bands. A detailed overview of state-of-the-art solutions will be given in Chaps. 2–5. It is noteworthy to emphasize that the techniques proposed are not limited to narrowband RXs design, because most of them are promising for wideband and high performance RXs.

1.4 Organization

The book is organized as follows:

1. Chapter 2 will present the design of a 2.4 GHz ZigBee RX using the typical cascade architecture. The selection of this architecture is supported by the detailed analysis of the key RX's metrics. New circuit techniques are then proposed to implement such architecture. The RX [48] exhibits a measured comparable performance with respect to the state-of-the-art.
2. Unlike the cascade architecture in Chap. 2, Chap. 3 describes a new extensive current-reuse architecture that reuses most of the current from RF-to-baseband. A 3rd-order channel selection is realized in the current domain before signal amplification. This architecture achieves high OB-IIP3, high and robust image rejection ratio (IRR), small area and low-power with zero external components. To verify the concept, a 2.4 GHz ZigBee RXs was implemented in a 65 nm complementary metal-oxide-semiconductor (CMOS) technology [49, 50].
3. In Chap. 4, a novel local-oscillator (LO)-defined N-path gain-boosted bandpass filter (GB-BPF) is studied as the core technique of the function-reuse RX that will be described in Chap. 5. Both the power and area efficiencies are improved when compared with the traditional passive N-path filter. A design example of 4-path LO tunable GB-BPF will be given [51].
4. Unlike the current-reuse RX as in Chap. 3, Chap. 5 describes a function-reuse RX for sub-GHz multi-ISM-band ZigBee applications. This architecture achieves small area, very low supply voltage and multi-band LO tunable matching with zero external components. To demonstrate the idea, the RX was implemented in 65 nm CMOS [52, 53].
5. Chapter 6 will present the conclusions of this book, highlighting the most important contributions. Also, an outlook to possible future work will be given.

References

1. R. Kraemer, M.D. Katz, *Short-Range*, *Wireless Communications Emerging Technologies and Applications* (Wiley, United Kingdom, 2009)
2. Wireless World Research Forum, http://www.wireless-world-research.org
3. IEEE Std 802.15.4. New York: IEEE (2003)
4. J.A. Gutiérrez, E.H. Callaway, R.L. Barrett, *Low-rate Wireless Personal Area Networks* (IEEE, New York, 2004)
5. F. Abdel-Latif, E.A. Hussiec, Ultra Low Power IEEE 802.15.4/ZigBee Compliant Transceiver, Ph.D. thesis, Texas A&M University, Dec 2009
6. IEEE Standard for Local and Metropolitan Area Networks—Part 15.6: Wireless Body Area Networks, IEEE 802 LAN/MAN Standards Committee, 6 Feb 2012
7. K.S. Kwak, S. Ullah, N. Ullah, An overview of IEEE 802.15.6 standard, in *Proceedings 3rd International Symposium on Applied Sciences in Biomedical and Communication Technologies (ISABEL)*, Nov 2010
8. A. Wang, M. Dawkins, G. Devita et al., A 1 V 5 mA multimode IEEE 802.15.6/bluetooth low-energy WBAN transceiver for biotelemetry applications. IEEE J. Solid-State Circ. **48**(1), 186–198 (2010)
9. N. Hunn, *WiFore Consulting*, *Essentials of Short-Range Wireless* (Cambridge University Press, Cambridge, 2010)
10. J. Decuir, Standards Architect, Bluetooth 4.0: Low Energy, CSR plc, 2010
11. http://e2e.ti.com/blogs_/b/connecting_wirelessly/archive/2010/03/09/bluetooth-low-energy-versus-zigbee.aspx
12. ZigBee Compared with Bluetooth Low Energy. Green Peak Technologies
13. Y. Liu, X. Huang, M. Vidojkovic, et al., A 1.9 nJ/b 2.4 GHz multistandard (bluetooth low energy/Zigbee/IEEE802.15.6) transceiver for personal/body-area networks. ISSCC Dig. Tech. Papers, pp. 446–447, Feb 2013
14. R. Rajan, *Ultra-Low Power Short-Range Radio Transceiver*, Microsemi Corporation, May 2012
15. S. Bandyopadhyay, A. Chandrakasan, Platform architecture for solar, thermal and vibration energy combining with MPPT and single inductor, in *Proceedings of the Symposium on VLSI circuits*, pp. 238–239, June 2011
16. E. Carlson, K. Strunz, B. Otis, A 20 mV input boost converter with efficient digital control for thermoelectric energy harvesting. IEEE J. Solid-State Circ. **45**(4), 741–750 (2010)
17. Y.-C. Shih, B. Otis, An inductorless dc-dc converter for energy harvesting with a 1.2 W bandgap-referenced output controller. IEEE Trans. Circuits Syst. II, Exp. Briefs **58**(12), 832–836 (2011)
18. K. Kadirvel, Y. Ramadass, U. Lyles, et al., A 330 nA energy harvesting charger with battery management for solar and thermoelectric energy harvesting. ISSCC Dig. Tech. Papers, pp. 106–108, Feb 2012
19. J.-P. Im, S.-W. Wang, K.-H. Lee, et al., A 40 mV transformer reuse self-startup boost converter with MPPT control for thermoelectric energy harvesting. ISSCC Dig. Tech. Papers, pp. 104–106, Feb 2012
20. F. Zhang, Y. Miyahara, B. Otis, Design of a 300 mV 2.4 GHz receiver using transformer-coupled techniques. IEEE J. Solid-State Circ. **48**(12), 3190–3205 (2013)
21. B. Cook, A. Berny, A. Molnar et al., Low-power 2.4 GHz transceiver with passive RX front-end and 400 mV supply. IEEE J. Solid-State Circ. **41**(12), 2757–2766 (2006)
22. A. Balankutty, S.-A. Yu, Y. Feng, P. Kinget, A 0.6 V zero-IF/low-IF receiver with integrated fractional-N synthesizer for 2.4 GHz ISM-band applications. IEEE J. Solid-State Circ. **45**(3), 538–553 (2010)
23. T.S. Rappaport, *Wireless communications principles and practices* (Prentice-Hall, New Jersey, 2002)
24. J.S. Seybold, *Introduction to RF propagation* (Wiley, Hoboken, 2005)

25. J. Bae, K. Song, H. Lee et al., A 0.24 nJ/b wireless body-area-network transceiver with scalable double-FSK modulation. IEEE J. Solid-State Circ. **47**(1), 310–321 (2012)
26. R.S. Elliott, *Antenna Theory and Design*, Revised edn. (Wiley, New York, 2003)
27. A. Liscidini, M. Tedeschi, R. Castello, Low-power quadrature receivers for ZigBee (IEEE 802.15.4) applications. IEEE J. Solid-State Circ. **45**, 1710–1719 (2010)
28. W. Kluge, F. Poegel, H. Roller et al., A fully integrated 2.4 GHz IEEE 802.15.4-compliant transceiver for ZigBee TM applications. IEEE J. Solid-State Circ. **41**, 2767–2775 (2006)
29. M. Camus, B. Butaye, L. Garcia et al., A 5.4 mW 0.07 mm^2 2.4 GHz front-end receiver in 90 nm CMOS for IEEE 802.15.4 WPAN stand. IEEE J. Solid-State Circ. **43**, 1372–1383 (2008)
30. J. Masuch, M. Delgado-Restituto, A 1.1 mW-RX—81.4 dBm sensitivity CMOS transceiver for bluetooth low energy. IEEE Trans. Microw. Theor. Tech. **61**(4), 1660–1674 (2013)
31. M. Contaldo, B. Baneriee, D. Ruffieux et al., A 2.4 GHz BAW-based transceiver for wireless body area networks. IEEE Trans. Biomed. Circ. Syst. **4**(6), 391–399 (2010)
32. J. Ayers, N. Panitantum, K. Mayaram, et al., A 2.4 GHz wireless transceiver with 0.95 nJ/b link energy for multi-hop battery-free wireless sensor networks, in *Proceedings of the Symposium on VLSI Circuits*, pp. 29–30, June 2010
33. B. Otis, Y. Chee, J. Rabaey, A 400 μW-RX, 1.6 mW-TX super—regenerative transceiver for wireless sensor networks. ISSCC Dig. Tech. Pap. **1**, 396–606 (2005)
34. P. Popplewell, V. Karam, A. Shamim et al., A 5.2 GHz BFSK transceiver using injection-locking and an on-chip antenna. IEEE J. Solid-State Circ. **43**(4), 981–990 (2008)
35. M. Vidojkovic, X. Huang, P. Harpe et al., A 2.4 GHz ULP OOK single-chip transceiver for healthcare applications. IEEE Trans. Biomed. Circ. Syst. **5**(6), 523–534 (2011)
36. A. Zahabi, M. Anis, M. Ortmanns, 3.1 GHz–3.8 GHz integrated transmission line super-regeneration amplifier with degenerative quenching technique for impulse-FM-UWB transceiver, in *Proceedings of European Solid-State Circuits Conference*, pp. 387–390, Sept 2011
37. M. Anis, R. Tielert, N. When, A 10 Mb/s 2.6 mW 6-to-10 GHz UWB impulse transceiver. in *Proceedings of IEEE International Conference on Ultra-Wideband (ICUWB)*, vol. 1, pp. 129–132, Sept 2008
38. M. Crepaldi, L. Chen, J. Fernandes et al., An ultra-wideband impulse-radio transceiver chipset using synchronized-OOK modulation. IEEE J. Solid-State Circ. **46**(10), 2284–2299 (2011)
39. R.K. Dokania, X. Wang, S. Tallur et al., A low power impulse radio design for body-area-networks. IEEE Trans. Circ. Syst. I, Reg. Pap. **58**(7), 1458–1469 (2011)
40. S. Gambini, J. Crossley, E. Alon et al., A fully integrated, 290 pJ/bit UWB dual-mode transceiver for cm-range wireless interconnects. IEEE J. Solid-State Circ. **47**(3), 586–598 (2012)
41. S. Solda, M. Caruso, A. Bevilacqua et al., A 5 Mb/s UWB-IR Transceiver front-end for wireless sensor networks in 0.13 μm CMOS. IEEE J. Solid-State Circ. **46**(7), 1636–1647 (2011)
42. X. Wang, Y. Yikun, B. Busze, et al., A meter-range UWB transceiver chipset for around-the-head audio streaming. ISSCC Tech. Papers, pp. 450–452, Feb 2012
43. D.D. Wentzloff, F.S. Lee, D.C. Daly, et al., Energy efficient pulsed-UWB CMOS circuits and systems, in *Proceedings of IEEE International Conference on Ultra-Wideband (ICUWB)*, pp. 282–287, Sept 2007
44. Y. Zheng, T. Yan, W. Chyuen, et al., A CMOS carrier less UWB transceiver for WPAN applications. ISSCC Dig. Tech. Papers, pp. 378–387, Feb 2006
45. M. Anis, M. Ortmanns, N. Wehn, A 2.5 mW 2 Mb/s fully integrated impulse-FM-UWB transceiver in 0.18 μm CMOS. IEEE MTT-S Int. Microwave Symp. Dig. pp. 1–3, June 2011
46. S. Geng, D. Liu, Y. Li, et. al., A 13.3mW 500 Mb/s IR-UWB transceiver with link-margin enhancement technique for meter-range communications. ISSCC Dig. Tech. Papers, pp. 160–161, Feb 2014
47. X. Wang, Y. Yu, B. Busze, et al., A meter-range UWB transceiver chipset for around-the-head audio streaming. ISSCC Dig. Tech. Papers, pp. 450–451, Feb 2012

48. Z. Lin, P.-I. Mak, R.P. Martins, A 0.14 mm^2, 1.4 mW, 59.4 dB-SFDR, 2.4 GHz ZigBee/WPAN receiver exploiting a "Split-LNTA + 50 % LO" topology in 65 nm CMOS. IEEE Trans. Microw. Theory Tech. **62**, 1525–1534 (2014)
49. Z. Lin, P.-I. Mak, R. P. Martins, A 1.7 mW 0.22 mm^2 2.4 GHz ZigBee RX exploiting a current-reuse blixer + hybrid filter topology in 65 nm CMOS. ISSCC Dig. Tech. Papers, pp. 448–449, Feb 2013
50. Z. Lin, P.-I. Mak, R.P. Martins, A 2.4-GHz ZigBee receiver exploiting an RF-to-BB-current-reuse blixer + hybrid filter topology in 65 nm CMOS. IEEE J. Solid-State Circ. **49**, 1333–1344 (2014)
51. Z. Lin, P.-I. Mak, R.P. Martins, Analysis and modeling of a gain—boosted N-path switched-capacitor bandpass filter. IEEE Trans. Circ. Syst. I **9**, 2560–2568, Sept 2014
52. Z. Lin, P.-I. Mak, R.P. Martins, A 0.5 V 1.15 mW 0.2 mm^2 sub-GHz ZigBee receiver supporting 433/860/915/960 MHz ISM bands with zero external components. ISSCC Dig. Tech. Papers, pp. 164–165, Feb 2014
53. Z. Lin, P.-I. Mak, R.P. Martins, A sub-GHz multi-ISM-band ZigBee receiver using function-reuse and gain-boosted N-path techniques for IoT applications. IEEE J. Solid-State Circ. **49**, 2990–3004 (2014)

Chapter 2
Design and Implementation of Ultra-Low-Power ZigBee/WPAN Receiver

In recent years, the proliferation of short-range wireless applications for Internet of Things and personal healthcare calls for ultra-low power and cost CMOS radios [1]. Ultra-low voltage (ULV) designs have been one of the key directions to approach a better power efficiency [2–5]. Regrettably, an ULV supply will limit the voltage swing, and device's f_T and overdrives, deteriorating the spurious-free dynamic range (SFDR) while necessitating area-hungry inductors (or transformers) to assist the bias and tune out the parasitic capacitances. This chapter describes the design and implementation of a compact, low-power and high-SFDR receiver suitable for ZigBee or wireless personal area network (WPAN) applications. The research background can be outlined as follows.

Four potential ultra-low-power receiver architectures are shown in Fig. 2.1. The first (Fig. 2.1a) employs a single low-noise transconductance amplifier (single-LNTA) followed by two passive I/Q mixers and transimpedance amplifiers (TIAs). If a 50 %-duty-cycle local oscillator (50 % LO) is applied, this topology can suffer from image current circulation between the I and Q paths, inducing I/Q crosstalk, unequal high-side and low-side gains, IIP2 and IIP3 [6]. Lowering the LO duty cycle to 25 % (Fig. 2.1b) can alleviate such issues [7], at the expense of extra sine-to-square LO buffers and logic operation. Another alternative is to add two signal buffers before the mixers (Fig. 2.1c), but they must be linear enough (i.e., more power) to withstand the voltage gain of the low-noise amplifier (LNA) [8, 9]. The basis of our proposed solution (Fig. 2.1d) is to split the LNTA into two, such that a single-ended RF input is maintained, while allowing isolated passive mixing that facilitates the use of a 50 % LO for power savings.

This chapter is organized as follows: Sect. 2.1 will give an overview of the operating principle of the proposed "split-LNTA + 50 % LO" receiver. An analytical comparison of it with the existing "single-LNTA + 25 % LO" architecture will be presented in Sect. 2.2. In Sect. 2.3, a number of circuit techniques will be proposed, including: (1) a low-power voltage-mode transimpedance amplifier (TIA) to enhance the out-channel linearity both at RF and baseband (BB); (2) a mixed-supply (V_{DD}) design approach [10] to alleviate the design trade-offs in RF LNTA (power, gain and noise) and BB TIA (power, linearity and signal swing); (3) a low-power LO generation scheme that consists of a LC voltage-controlled oscillator (VCO) and an input-impedance-boosted Type-II RC-CR network. They

Z. Lin et al., *Ultra-Low-Power and Ultra-Low-Cost Short-Range Wireless Receivers in Nanoscale CMOS*, Analog Circuits and Signal Processing,
DOI 10.1007/978-3-319-21524-2_2

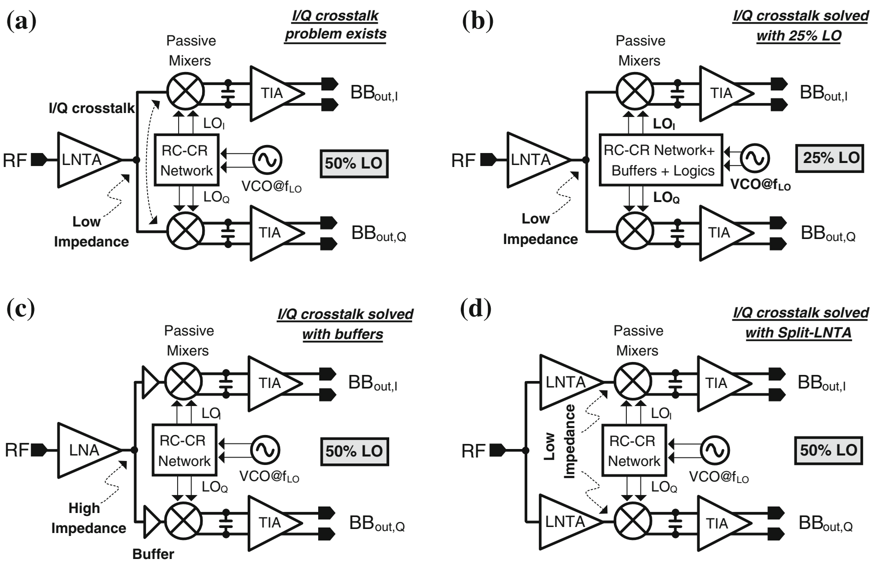

Fig. 2.1 Four potential receiver architectures: **a** Single-LNTA + 50 % LO. **b** Single-LNTA + 25 % LO. **c** Single-LNA + 50 % LO + signal buffers. **d** Split-LNTA + 50 % LO (proposed)

optimize the VCO's output swing with the LC tank's quality factor, while offering adequate I/Q accuracy at low power. The measured experimental results will be reported in Sect. 2.4.

2.1 Proposed "Split-LNTA + 50 % LO" Receiver

The split-LNTA (Fig. 2.2) is based on two self-biased inverter-based amplifiers (M_1, M_2 and R_F), which have no inner parasitic pole. They also can take the speed advantage of fine linewidth CMOS to lower the device overdrive voltages, featuring a high g_m-to-I_d efficiency at low V_{DD} ($V_{DD06} = 0.6$ V). Its single-ended RF input avoids the RF balun and its associated insertion loss. In front of the split- LNTA, a proper co-design between the RF input capacitance (C_{in}) and bond wire (L_{bw}) facilitates the input impedance matching, while offering a passive pre-gain (Av) decisively important to the NF and power efficiency. The two LNTAs convert the RF signal (v_{in}) into two equal currents $i_{out,I}$ and $i_{out,Q}$ for the I and Q channels, respectively. To avoid the parasitic and area impact from AC coupling, $i_{out,I}$ and $i_{out,Q}$, are directly DC-coupled to the passive mixers (M_3 and M_4). As long as the DC current passing through M_3 and M_4 is kept small, the 1/f noise induced by the mixers can be minimized [11]. This aim can be achieved by matching the output common-mode level of the LNTA to that of the BB TIA.

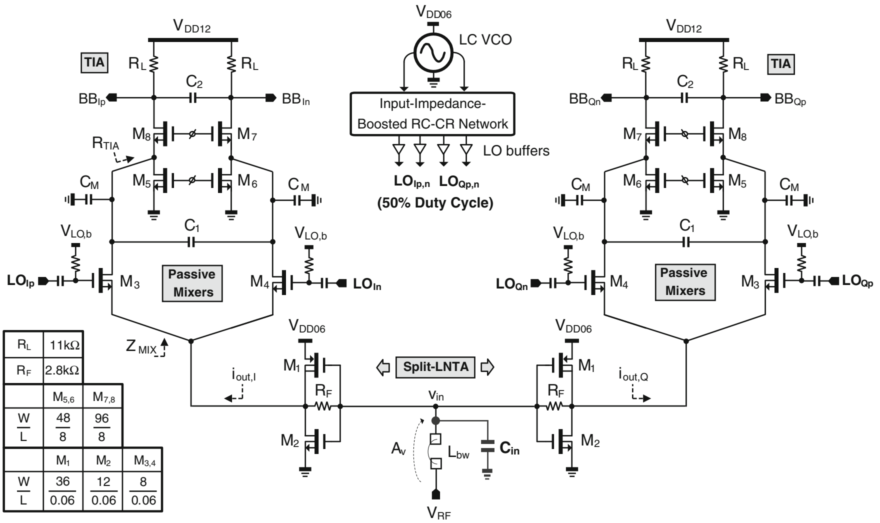

Fig. 2.2 Schematic of the proposed receiver exploiting passive pre-gain, split-LNTA, passive mixers, 50 % LO and common-gate TIAs

The 50 % 4-phase LO ($LO_{\mathrm{Ip,n}}$ and $LO_{\mathrm{Qp,n}}$) is generated by a 2.4-GHz *LC* VCO followed by a new type-II *RC-CR* network, which features a capacitor divider at the input to boost the input impedance. When driving the LO to the mixers (M_3 and M_4), a proper DC level ($V_{\mathrm{LO,b}}$) can optimize the switching time. The down converted low-IF (2 MHz) signal is further amplified by a common-gate TIA ($M_{5\text{-}8}$ and R_{L}), which uses a 1.2 V (V_{DD12}) supply to accommodate more signal swing and enhance linearity. Here, we assume a complex low-IF filter will follow the BB TIA, rendering the *1/f* noise and IIP2 not significant and will not be further addressed. Due to the bidirectional transparency of passive mixers [7, 8], the BB capacitors (C_1 and C_{M}) can enhance the selectivity at both RF (the output of the LNTA) and BB, improving the out-band linearity. The grounded C_{M} also helps to suppress the common-mode RF feed through, which is limited by the bond wire inductance that appears in series with C_{M} under common-mode operation.

2.2 Comparison of “Split-LNTA + 50 % LO” and “Single-LNTA + 25 % LO” Architectures

This Section presents an analytical comparison of the two architectures: “split-LNTA + 50 % LO” and “single-LNTA + 25 % LO”. For brevity, “50 % LO” and “25 % LO” are exploited to represent them, respectively. Figure 2.3a, b show their simplified equivalent circuits. For a fair comparison, the two LNTAs in Fig. 2.3a are modeled as g_{m} (transconductance) and $2R_{\mathrm{out}}$ (output resistance),

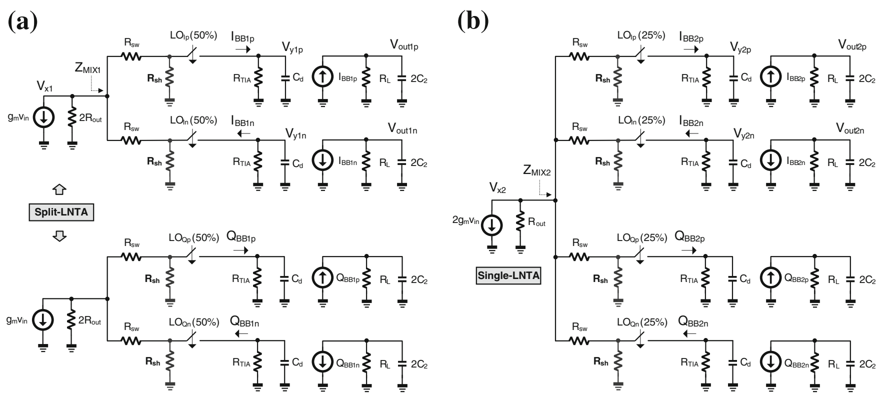

Fig. 2.3 Small-signal equivalent circuits. **a** Split-LNTA + 50 % LO. **b** Single-LNTA + 25 % LO

whereas the single LNTA in Fig. 2.3b is modeled as $2g_m$ and R_{out}. These models are developed under the same approach described in [12–14], where the harmonic up-conversion in passive mixers is modeled as R_{sh}. The impedances looking into the 50 %-LO and 25 %-LO mixers are denoted as Z_{MIX1} and Z_{MIX2}, respectively. Each mixer features an on-resistance of R_{sw}. R_{TIA} is the input resistance of the TIA. The single-ended differential mode capacitance is denoted as C_d (=C_M + $2C_1$).

2.2.1 Gain

For Fig. 2.3a, we summarize in (2.1)–(2.5) the derived expressions of both Z_{MIX1} and the voltage gain (A_{Vx1}) at V_{x1} at the LO + IF frequency (ω_{LO} + ω_{IF}); the baseband output current (I_{BB1}) with respect to v_{in}; the voltage gain (A_{Vy1}) at $V_{y1p,n}$, and finally the voltage gain (A_{Vout1}) at $V_{out1p,n}$,

$$Z_{MIX1}|@(\omega_{LO}+\omega_{IF}) \approx R_{sw} + \left(\frac{2Z_{BB}}{\pi^2}//R_{sh}\right) \tag{2.1}$$

$$\text{where } Z_{BB} = \frac{1}{s(2C_1+C_M)}//R_{TIA};\, R_{sh} \approx \frac{2}{3}(2R_{out}+R_{sw})$$

$$A_{Vx1}@(\omega_{LO}+\omega_{IF}) \approx g_m(2R_{out}//Z_{MIX1}) \tag{2.2}$$

$$\frac{I_{BB1}}{v_{in}}@DC = \frac{I_{BB1p}-I_{BB1n}}{v_{in}} \approx g_m\frac{2R_{out}}{R_{TIA}+2(2R_{out}+R_{sw})}\frac{4}{\pi} = G_{m1} \tag{2.3}$$

$$A_{Vy1}@DC = A_{Vy1p} - A_{Vy1n} \approx G_{m1}R_{TIA} \tag{2.4}$$

$$A_{Vout1}@DC = A_{Vout1p} - A_{Vout1n} \approx G_{m1}R_L \tag{2.5}$$

Similarly, for Fig. 2.3b, we have (2.6)–(2.10) the derived expressions of both Z_{MIX2} and the voltage gain (A_{Vx2}) at V_{x2} at the LO + IF frequency (ω_{LO} + ω_{IF}); the baseband output current (I_{BB2}) with respect to v_{in}; the voltage gain (A_{Vy2}) at $V_{y2p,n}$, and finally the voltage gain (A_{Vout2}) at $V_{out2p,n}$,

$$Z_{MIX2}|@(\omega_{LO} + \omega_{IF}) \approx R_{sw} + \left(\frac{2Z_{BB}}{\pi^2}//R_{sh}\right) \tag{2.6}$$

where $Z_{BB} = \frac{1}{s(2C_1 + C_M)}//R_{TIA}; R_{sh} \approx 4(R_{out} + R_{sw})$

$$A_{Vx2}@(\omega_{LO} + \omega_{IF}) \approx 2g_m(R_{out}//Z_{MIX2}) \tag{2.7}$$

$$\frac{I_{BB2}}{v_{in}}@DC = \frac{I_{BB2p} - I_{BB2n}}{v_{in}} \approx 2g_m \frac{R_{out}}{R_{TIA} + 4(R_{out} + R_{sw})}\frac{4\sqrt{2}}{\pi} = G_{m2} \tag{2.8}$$

$$A_{Vy2}@DC = A_{Vy2p} - A_{Vy2n} \approx G_{m2}R_{TIA} \tag{2.9}$$

$$A_{Vout2}@DC = A_{Vout2p} - A_{Vout2n} \approx G_{m2}R_L \tag{2.10}$$

Note that the output capacitance of the LNTA was neglected. In fact, the output capacitance of LNTA will induce C_{out} and $2C_{out}$ for the g_m and $2g_m$ LNTA stages, respectively. This will render the output impedance ratio at V_{x1} and V_{x2} slightly larger than 2. Besides, the parasitic capacitor will affect R_{sh} too. The proposed separated gm stage imposes a smaller C_{out} and thus lowers the degradation of gain and NF when compared with those predicted by Eqs. (2.11) and (2.12). With proper sizing, it would be possible to achieve $R_{sw} \ll R_{out}$ and $R_{sw} \ll R_{TIA}$ and R_L, such that the gain difference between 25 % LO and 50 % LO at different RF and BB nodes can be estimated as,

$$\begin{aligned}
\Delta A_{Vx1,2}@\omega_{LO} &= 20\log A_{Vx2} - 20\log A_{Vx1} \approx 20\log\frac{2(R_{out}//\frac{2R_{TIA}}{\pi^2}//4R_{out})}{2R_{out}//\frac{2R_{TIA}}{\pi^2}//\frac{4R_{out}}{3}} = 6\,\text{dB} \\
\Delta A_{Vy1,2}@DC &= 20\log A_{Vy2} - 20\log A_{Vy1} = 20\log\left(\sqrt{2}\frac{R_{TIA} + 4R_{out} + 2R_{sw}}{R_{TIA} + 4R_{out} + 4R_{sw}}\right) \approx 3\,\text{dB} \\
\Delta A_{Vout1,2}@DC &= 20\log A_{Vout2} - 20\log A_{Vout1} = 20\log\left(\sqrt{2}\frac{R_L + 4R_{out} + 2R_{sw}}{R_L + 4R_{out} + 4R_{sw}}\right) \approx 3\,\text{dB}
\end{aligned} \tag{2.11}$$

From (2.11), the 25 % LO should have a higher gain at both RF and BB nodes than the 50 % LO. However, as analyzed in Sect. 2.3.3, a higher gain at RF will penalize the IIP3, while a higher BB gain can be achieved easily by using a larger R_L. Regarding the impact of these gain differences to the NF it will be analyzed next.

2.2.2 NF

The NF is analyzed according to the equivalent LTI noise model [12–14]. As shown in Fig. 2.4a, b, the four noise sources are the thermal noises from $R_s(V^2_{n,Rs} = 4kTR_s)$, LNTA $(I^2_{n,g_m} = 4kT\gamma_1 g_m \text{ or } I^2_{n,2g_m} = 4kT\gamma_1 2g_m)$, $R_{sw}(V^2_{n,sw} = 4kTR_{sw})$ and the noise from TIA is $V^2_{n,TIA} \approx {}^{4kT\gamma_2}/_{g_{m\_TIA}} \approx 4kT\gamma_2 R_{TIA}$, given that the output impedance of the mixer is sufficiently large. Here, g_{m_TIA} is the transconductance of the bias transistor for the TIA, while the noise from the CG device is degenerated. An accurate model of the TIA noise can be found in [11]. The noise of R_F is ignorable and the noise coupling between the I and Q paths under a 50 % LO is minor (confirmed by simulations), easing the NF calculation of each path separately. The noise factor (F) can be found by dividing the total output noise by the portion related with R_s contribution,

$$F = 1 + \frac{\gamma_1}{R_s A_v^2 G_m} + \frac{R_{sw}}{R_s A_v^2 G_m^2 R^2} + \frac{(R + R_{sw})^2}{R_s A_v^2 G_m^2 R^2 \beta \gamma_2 R_{TIA}} + \frac{a\gamma_1}{R_s A_v^2 G_m} + a + \frac{aR_{sw}}{R_s A_v^2 G_m^2 R^2} \tag{2.12}$$

where $\beta = \frac{2}{\pi^2}$ is the down conversion scaling factor and a is the harmonic folding factor,

$$a = \left(\frac{\pi^2}{4} - 1\right), G_m = g_m \text{ and } R = 2R_{out} \text{ for Fig.2.4(a)}$$
$$a = \left(\frac{\pi^2}{8} - 1\right), G_m = 2g_m \text{ and } R = R_{out} \text{ for Fig.2.4(b)}$$

In (2.12), the 2nd term is from the LNTA, the 3rd term is from the mixer, and the 4th term is from the TIA. The rest of the terms are the noise folding from the odd harmonics of the LO for LNTA, R_s and R_{SW}, respectively. The NF calculated from

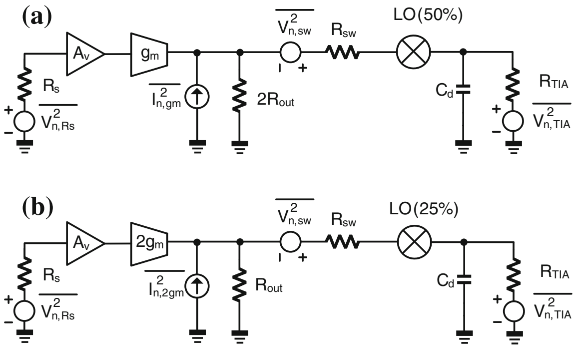

Fig. 2.4 Equivalent LTI noise model with pre-gain for **a** 50 % LO (Fig. 2.3a) and **b** 25 % LO (Fig. 2.3b)

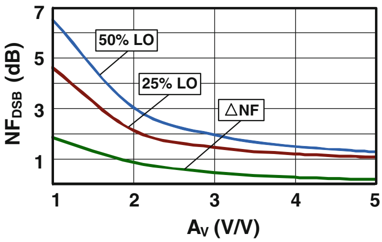

Fig. 2.5 Simulated NF_{DSB} and **ΔNF** against A_v for 50 % LO and 25 % LO

(2.12) for 50 % LO is single sideband (SSB). For a double sideband (DSB) NF, it is 3 dB less. Since the harmonic's power of 50 % LO is larger than that of 25 % LO, the folding terms of 50 % LO are also higher. From (2.12), the DSB NF of 50 % LO and 25 % LO are plotted in Fig. 2.5 as a function of A_V, where $\Delta NF = NF_{50\%} - NF_{25\%}$ R_{sw} = 50 Ω, $\gamma_1 = \gamma_2 = 1$, g_m = 9 mS, R_{out} = 200 Ω and R_{TIA} = 2.5 kΩ. It can be seen that ΔNF is reduced to 0.91 dB (0.51 dB) when A_V is just 2 V/V (3 V/V), which is easily achievable in practice. In fact, a moderated A_V can even eliminate the need of the LNTA (or LNA) [3]. However, when considering also the input matching and LO-to-RF isolation, both pre-gain and LNTA should be employed concurrently. The simulated LO-to-RF isolation is <–100 dBm. Due to the passive pre-gain, the IIP3 of the receiver is more demanding than the NF, promoting the use of a 50 % LO. Together with its power advantage (i.e. lower VCO frequency and no divider), our proposed topology (i.e., pre-gain + split-LNTA + 50 % LO) should ease the tradeoff between NF, IIP3, area and power.

2.2.3 IIP3

The 3rd-order intermodulation (IM3) distortion is analyzed to assess the linearity. The aim is to find the in-band IIP3 of the receiver under 50 % LO and 25 % LO in response to two-tone excitation. Assuming that the nonlinearity of the receiver is dominated by the LNTA, its nonlinearity contributions are considered as:

(a) 3rd-order LNTA nonlinearity due to input excitation v_{in} [α_2 (I/V^3)].
(b) 3rd-order LNTA nonlinearity due to output excitation v_x [α_3 (I/V^3)].

Thus, $i_{ds} = \alpha_1 v_{in} + \alpha_2 v_{in}^3 + \alpha_3 v_X^3$. If the coefficients α_1, α_2 and α_3 are assumed to be proportional to the device *W/L*,

For 50 % LO, $\alpha_1 = g_m$, $\alpha_2 = g_{m3}$, $\alpha_3 = g_{o3}$;
For 25 % LO, $\alpha_1 = 2g_m$, $\alpha_2 = 2g_{m3}$, $\alpha_3 = 2g_{o3}$.

where g_{m3} and g_{03} are the 3rd-order nonlinear transconductance and conductance, respectively. With a two-tone excitation of amplitude A and the 1st-order voltage gain and current gain given in (2.1)–(2.11), the IM3 output voltage for each of the nonlinear coefficients listed above can be written as,

$$v_{o3\alpha2} = \frac{3}{4} g_{m3} A^3 I_{BB1} R_L;\ v_{o3\alpha3} = \frac{3}{4} g_{o3} A_{V\times1}^3 A^3 I_{BB1} R_L$$

for a 50 % LO. Thus,

$$IM_{3\_50\%} = \frac{v_{o3\alpha2} + v_{o3\alpha3}}{v_{01\alpha1}} = \frac{\frac{3}{4} g_{m3} A^3 I_{BB1} R_L + \frac{3}{4} g_{o3} A_{Vx1}^3 A^3 I_{BB1} R_L}{A g_m I_{BB1} R_L}$$

$$\text{Let} \qquad IM_{3\_50\%} = 1 \rightarrow IIP_{3\_50\%} = \sqrt{\frac{4 g_m}{3(g_{m3} + g_{o3} A_{Vx1}^3)}} \tag{2.13}$$

Following the same procedure, the IIP3 for 25 % LO can be derived as,

$$IIP_{3\_25\%} = \sqrt{\frac{4 g_m}{3(g_{m3} + g_{o3} A_{Vx2}^3)}} \tag{2.14}$$

Since $A_{Vx2} > A_{Vx1}$, we can find that, from (2.13)–(2.14), the LNTA's 3rd-order nonlinearity term is larger for a 25 % LO. Thus, the IIP3 of 50 % LO should be better than that of 25 % LO, benefiting the SFDR since both architectures will feature a similar NF after adding the pre-gain.

2.2.4 Current- and Voltage-Mode Operations

Both 25 % LO and 50 % LO architectures can be intensively designed for current-mode or voltage-mode operation. For a high-performance design like [7, 8, 12], $R_{TIA} \ll R_{out}$ and $R_{sw} \ll R_{out}$ are preferred to keep the signals in the deep current mode. As such, (2.3) and (2.8) can be simplified as $G_{m1} = \frac{2g_m}{\pi}$ and $G_{m2} = \frac{2\sqrt{2}g_m}{\pi}$, respectively. Both of them are higher when compared to themselves in the voltage-mode operation. In terms of IIP3 and NF, the current mode is also preferable since $A_{Vx1} \approx g_m(R_{sw} + \frac{2}{\pi^2} R_{TIA})$ and $A_{Vx2} \approx 2g_m(R_{sw} + \frac{2}{\pi^2} R_{TIA})$ will be lower, and the noise due to the folding term and TIA will be also smaller as noted in (2.12).

Nevertheless, the current-mode operation also brings up two sizing constraints being less attractive for *low-power* design: (1) a low R_{sw} entails a large device *W/L* and a higher overdrive voltage for the mixers; both calling for a larger power budget in the LO path, and (2) a low R_{TIA} implies that the TIA has to draw a large bias current. For example, if a low R_{TIA} of 50 Ω is required from the 1.2-V TIA (a common-gate amplifier), its bias current is as high as I_{bias} = 2 mA for a typical overdrive voltage of 200 mV. Thus, for ultra-low-power applications like

Table 2.1 Proposed Receiver under current- and voltage-mode operations

Mode	Gain	NF	In-Band IIP3	Power	Suitable for
Current mode (Small R_{sw} & R_{TIA})	$\nearrow$	$\searrow$	$\nearrow$	$\nearrow$	High performance
Voltage mode (Large R_{sw} & R_{TIA})	$\searrow$	$\nearrow$	$\searrow$	$\searrow$	Ultra low power

ZigBee/WPAN that has relaxed NF and linearity requirements, higher R_{sw} and R_{TIA} are preferable to operate the receiver more on the voltage mode. A summary of performance differences in current- and voltage-mode operations is given in Table 2.1.

2.3 Circuit Techniques

2.3.1 Impedance Up Conversion Matching

From Sect. 2.2, we expect a passive pre-gain A_v of 2 to 3 V/V. As shown in Fig. 2.6a, A_v can be derived under $R_{in} = R_s$,

$$\frac{V_{out}^2}{2R_{out}} = \frac{V_s^2}{8R_s}, V_{out} = V_{in}A_v, V_{in} = 0.5V_s \Rightarrow A_v = \sqrt{\frac{R_{out}}{R_{in}}}$$

Thus, an up-conversion matching network is entailed to ensure $A_v > 1$. A convenient way to achieve it is to use L_{bw} to resonate with C_{in}. The schematic is shown in Fig. 2.6b. The parallel connection of C_{in} and R_{out} can be transformed into

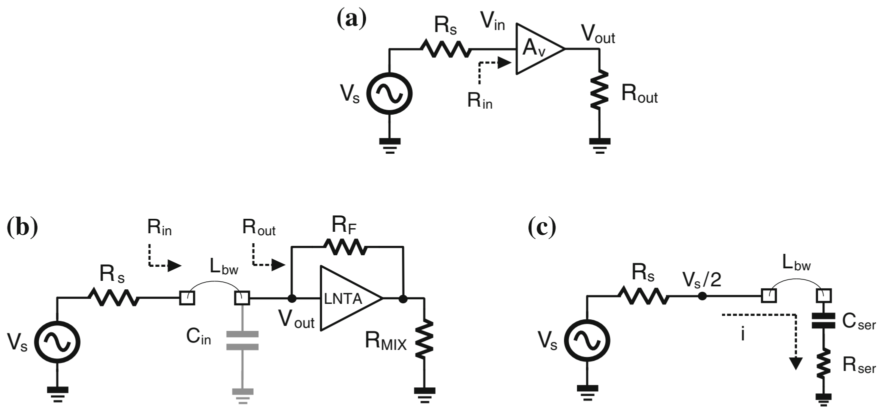

Fig. 2.6 Input impedance matching: **a** A_v converts R_{out} to R_{in} to match with R_s, **b** L_{bw} C_{in} as an impedance conversion network and its **c** narrowband equivalent circuit

a series connection of C_{ser} and R_{ser}, as shown in Fig. 2.6c. At $L_{bw}C_{ser}$ resonance, and with $R_{ser} = R_s$ and $i = \frac{V_s}{2R_{ser}}$, we have,

$$V_{out} = V_{R_{ser}} + V_{C_{ser}} = \frac{V_S}{2}(1 - j\frac{Q_C}{2})$$

where,

$$V_{R_{ser}} = -j\frac{Q_C V_s}{2} sC_{ser}R_{ser} = \frac{V_s}{2}$$

$$V_{C_{ser}} = \frac{1}{j\omega_0 C_{ser}}\frac{V_s}{2R_{ser}} = -j\frac{Q_C}{2}V_s,$$

$$\omega_0 = \frac{1}{\sqrt{L_{bw}C_{ser}}} \text{ and } Q_C = \frac{\sqrt{L_{bw}/C_{ser}}}{R_{ser}}$$

Interestingly, such a voltage boosting factor $\sqrt{1 + Q_c^2/4}$ is larger than the conventional inductively-degenerated LNA, which is only $\frac{Q_C}{2}$. In fact, when the capacitance of the PCB trace is accounted, the Q of the matching network will be higher, easing the impedance matching.

2.3.2 Mixer-TIA Interface Biased for Impedance Transfer Filtering

For the employed single-balanced passive mixers, the RF-to-IF feed through has to be addressed. Based on Fig. 2.7, we can calculate the currents i_{M7} and i_{M8} with respect to the RF current i_{RF} as given by,

$$i_{M7} = \frac{i_{RF}}{2}[1 - \text{sign}(\cos\omega_{LO}t)] \quad (2.15)$$

$$i_{M8} = \frac{i_{RF}}{2}[1 + \text{sign}(\cos\omega_{LO}t)] \quad (2.16)$$

They imply that the currents can be decomposed into the differential mode (Fig. 2.7a) with amplitude of $2i_{RF}/\pi$ at BB, and into the common mode (Fig. 2.7b) with amplitude of $0.5i_{RF}$ at RF. To suppress the latter, C_M was added to create a lowpass pole ($C_M//R_{TIA}$). For the differential IF signal, the pole is located at ($C_M + 2C_1$)//R_{TIA}, which suppresses the out-of-channel interferers before they enter the TIA. As such, the TIA can be biased under a very small bias current. The resultant high input impedance of the TIA, indeed, benefits both BB and RF

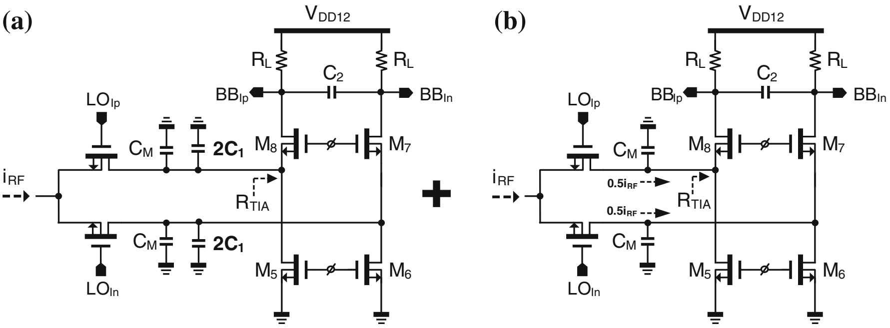

Fig. 2.7 Equivalent circuits of the mixer-TIA interface for **a** the differential low-IF signal and **b** the common-mode RF feed through

filtering because of the bidirectional impedance-translation property of the passive mixers [7, 8]. Figure 2.8 shows the simulated out-band IIP3, which is subject to the allowed total capacitance of $C_M + 2C_1$. For instance, when $C_M + 2C_1$ is increased from 16 to 42 pF, the out-band IIP3 raises from +2.5 to +4.7 dBm, at the expense of the die area. For the on- resistance of the mixer switches (R_{sw}), it involves a tradeoff of the LO path's power to the out-band IIP3 and NF. As shown in Fig. 2.9, if R_{sw} is increased from 50 to 150 Ω for power savings, the NF and out-band IIP3 will be penalized by $\sim$1 dB.

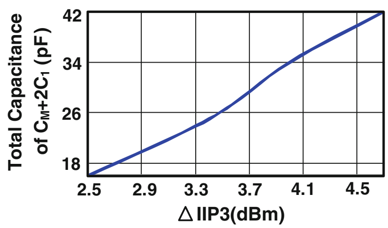

Fig. 2.8 Out-band IIP3 can be improved by allowing more total capacitance of $C_M + 2C_1$

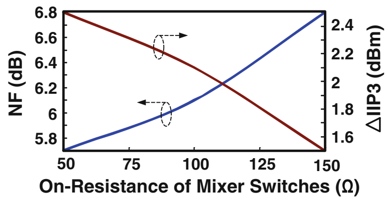

Fig. 2.9 The on-resistance of the mixer switches represents a tradeoff among the LO-path's power, out-band IIP3 and NF

2.3.3 RC-CR Network and VCO Co-Design

The *LC* VCO (Fig. 2.10a) employs a complementary *NMOS-PMOS* ($M_{1\text{-}4}$) negative transconductor. For power savings, M_1 and M_2 are based on AC-coupled gate bias ($V_{vco,b}$) to lower the supply to 0.6 V. Here, we implement a capacitive divider (C_{M1} and C_{M2}) to boost the input impedance of its subsequent two-stage *RC-CR* network (Fig. 2.10b). The optimization details are presented next.

RC-CR network is excellent for low-power and narrowband *I/Q* generation. With a Type-II architecture, both phase balancing and insertion loss can be better optimized than its Type-I counterpart [15]. For instance, the simulated insertion loss of a two-stage Type-II *RC-CR* network is roughly 2 dB as shown in Fig. 2.11, which will be raised to 4 to 5 dB if a Type-I topology is applied (not shown). For low-power LO buffering, the amplitude balancing is critical because its imbalance will lead to inconsistent zero-crossing points, resulting in AM to duty-cycle

	$M_{1,2}$	$M_{3,4}$	L_P	C_{M1}	C_{M2}	R_{N1}	C_{N1}	R_{N2}	C_{N2}
$\frac{W}{L}$	$\frac{12}{0.12}$	$\frac{24}{0.12}$	4.6nH	530fF	280fF	450Ω	35fF	900Ω	120fF

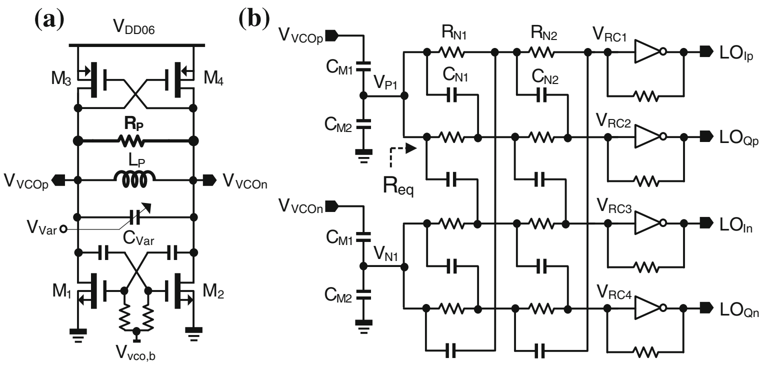

Fig. 2.10 **a** LC VCO and **b** the proposed input-impedance-boosted two-stage Type-II RC-CR network for 4-phase 50 % LO generation

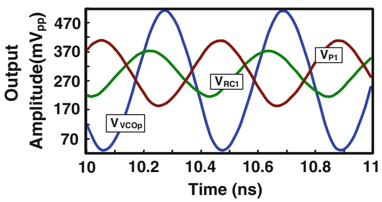

Fig. 2.11 Simulated time-domain signals at the output of the VCO (V_{vcop}), capacitor divider (V_{p1}) and the RC-CR network (V_{RC1})

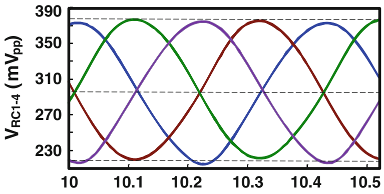

Fig. 2.12 Simulated time-domain signals at $V_{RC1\text{-}4}$

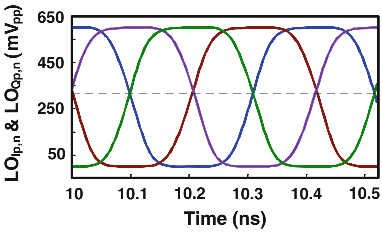

Fig. 2.13 Simulated time-domain signals at $LO_{Ip,n}$ and $LO_{Qp\text{-}n}$

distortion. Figures 2.12 ($V_{RC1\text{-}4}$) and 2.13 ($LO_{Ip,n}$ and $LO_{Qp,n}$) are the simulated transient waveforms, showing the consistent duty cycle and zero-crossing points achieved in the proposed design.

For a *RC-CR* network operated at 2.4 GHz, if we select R_{N1} = 1 kΩ, C_{N1} is just 66 fF, which benefits the area, VCO tuning range and phase noise, but the *I*/*Q* accuracy over PVT variations should be considered [16]

$$\frac{\sigma(\text{Image Out})}{\text{Desired Out}} = 0.25\sqrt{\left(\frac{\sigma_R}{R}\right)^2 + \left(\frac{\sigma_C}{C}\right)^2} \tag{2.17}$$

Since ZigBee/WPAN applications call for a low image- rejection ratio (IRR) of 20–30 dB [17], according to (2.17), the matching of the resistors (σ_R) and capacitors (σ_C) can be relaxed to 2.93 % for a 30-dB IRR (3σ). The sizes of $C_{N1,2}$ and $R_{N1,2}$ are summarized in Fig. 2.10. The poles from $C_{N1,2}$ and $R_{N1,2}$ are distributed around 2.4 GHz to cover the PVT variations. The impact of R_{N1} to the VCO can be analyzed as follows:

When the VCO's inductor is 4 nH with a Q of 20 ($R_P \approx 1.2$ kΩ), we have $R_{tank} \approx 0.5R_P//0.5R_{N1}$. Thus, directly connecting the *RC-CR* network to the VCO will limit the *LC* tank's Q_{tank} degrading the phase noise [18, 19]. To alleviate this, we boost up the equivalent input resistance of the *RC-CR* network (R_{eq}) by adding a capacitive divider (C_{M1} and C_{M2}). For the total tank capacitance C_{tank}, it can be approximated as

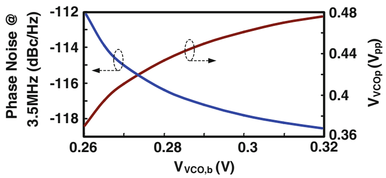

Fig. 2.14 Trade-off between VCO output amplitude and phase noise with respect to $V_{vco,b}$

$$C_{tank} \approx 2C_{Var} + \frac{(C_{M2} + 2C_{N1})C_{M1}}{C_{M1} + C_{M2} + 2C_{N1}} \tag{2.18}$$

By defining an input-impedance boosting factor n,

$$n = \frac{C_{M1}}{C_{M1} + C_{M2} + 2C_{N1}} \tag{2.19}$$

we have

$$V_{P1} \approx nV_{VCOp} \tag{2.20}$$

It means that the signal swing (V_{P1}) delivered to the *RC-CR* network are in trade-off with n. Handily, in our V_{CO}, sweeping $V_{vco,b}$ can track the phase noise with the output swing (Fig. 2.14). Given a bias current and a phase noise target, R_{tank} can be set from $V_{VCOp} \approx 2I_{bias}R_{tank}$, and n can be set from (2.21) with a specific R_p and R_{eq},

$$R_{tank} \approx \frac{R_{eq}}{n} \parallel \frac{R_P}{2} \tag{2.21}$$

In this work, n = 0.6 is selected to balance the output swing with C_{tank} and the total tank resistance (R_{tank}).

2.4 Experimental Results

The receiver (Fig. 2.15) fabricated in 65-nm CMOS occupies an active area of 0.14 mm^2 and is encapsulated in a 44-pin CQFP package for PCB-based measurements. The estimated bond wire inductance is ~7 nH for the provided package (13.5 × 13.5 mm). Figure 2.16 shows that the measured S_{11} is –8 dB within 2.24–2.46 GHz (for a different package, external inductor or capacitor can be added to optimize S_{11}). The simulation results with and without considering the PCB trace capacitances are also given. The measured voltage gain is 32.8–28.2 dB and the DSB NF is between 8.6–9 dB for an IF spanning from 1 to 3 MHz, as shown in Fig. 2.17. We also measured the gain and NF from 2.2 to 2.6 GHz (Fig. 2.18).

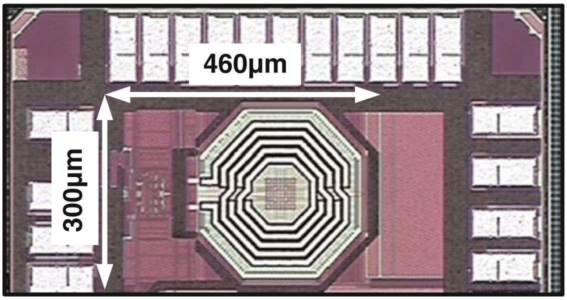

Fig. 2.15 Chip micrograph of the fabricated receiver

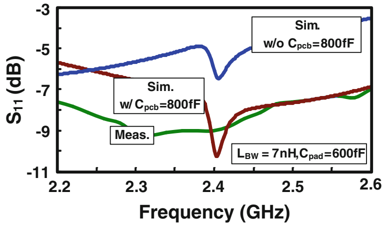

Fig. 2.16 Measured S_{11}, and simulated S_{11} with and without C_{pcb}

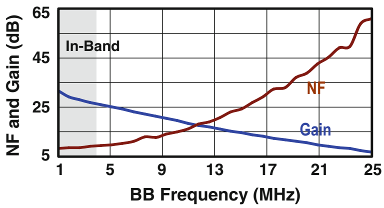

Fig. 2.17 Measured receiver gain and NF versus BB frequency

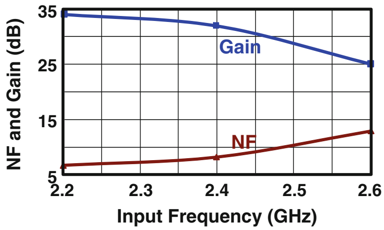

Fig. 2.18 Measured receiver gain and NF versus input signal frequency

For a narrowband receiver, the linearity is mainly justified by the out-channel linearity tests. According to the case given in [17, 20], two tones are applied at [f_{LO} + 10 MHz, f_{LO} + 22 MHz] with a power level sweeping from –24 to –32 dBm. Because of the RF and baseband filtering associated with the bidirectional property of passive mixers, the out-band IIP3 (Fig. 2.19) achieves –7 dBm and the P_{1dB} is –26 dBm.

For the VCO, it measures 21 % tuning range from 2.623 to 2.113 GHz, as shown in Fig. 2.20. At 3.5-MHz offset, the phase noise (Fig. 2.21) is –112.46 dBc/Hz,

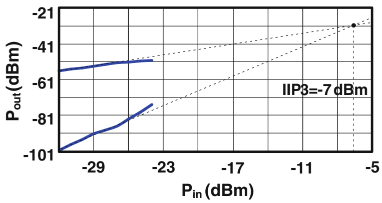

Fig. 2.19 Measured out-of-band IIP3

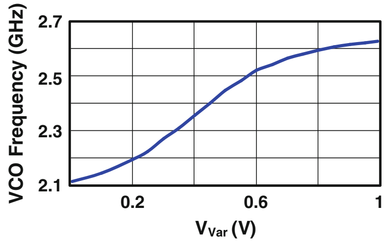

Fig. 2.20 Measured VCO turning range

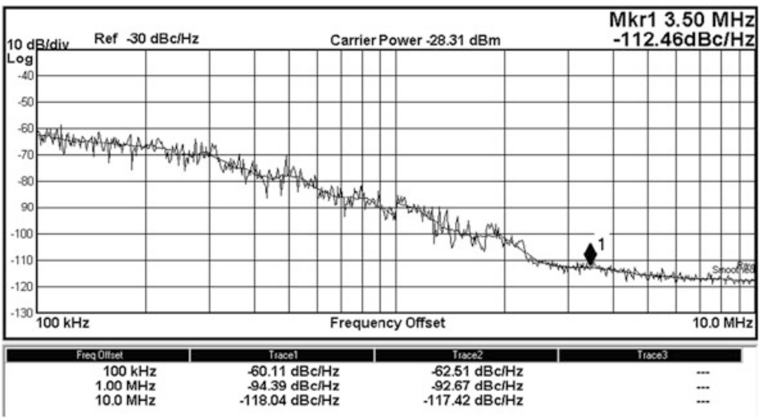

Fig. 2.21 Measured VCO phase noise at 2.4 GHz

fulfilling the specification (–102 dBc/Hz [17, 20]) with an adequate margin. From frequency 100 kHz to 1 MHz, the result fits the $^1/_{f^3}$ slope, and from 1 to 10 MHz, it starts to be saturated, primarily limited by the small output amplitude (–28.31 dBm) of the test buffer.

Based on transient measurements, the I/Q BB differential outputs (Fig. 2.22) has $\sim$0.08 dB gain mismatch and 2° phase match, corresponding to an IRR of $\sim$25 dB.

The performance summary and benchmark are given in Table 2.2 [5, 17, 21–27]. This work [28] succeeds in achieving the highest power and area efficiencies via proposing a mixed-V_{DD} topology co-optimized with a number of circuit techniques. Only one on-chip inductor is entailed in the VCO. The achieved NF and out-band IIP3 correspond to a competitive SFDR of 59.4 dB according to [17, 19],

$$\mathrm{SFDR} = \frac{2(\mathrm{P_{IIP3}} + 174\mathrm{dBm} - \mathrm{NF} - 10\log\mathrm{B})}{3} - \mathrm{SNR_{min}} \quad (2.22)$$

where SNR_{min} = 4 dB is the minimum signal-to-noise ratio required by the application, and B = 2 MHz is the channel bandwidth. As presented in Figs. 2.8 and 2.9, the SFDR can be further optimized by allowing more budgets in area (bigger $C_M + 2C_1$) and/or power (smaller on-resistance of the mixer switches), being a design-friendly architecture easily adaptable to different specifications.

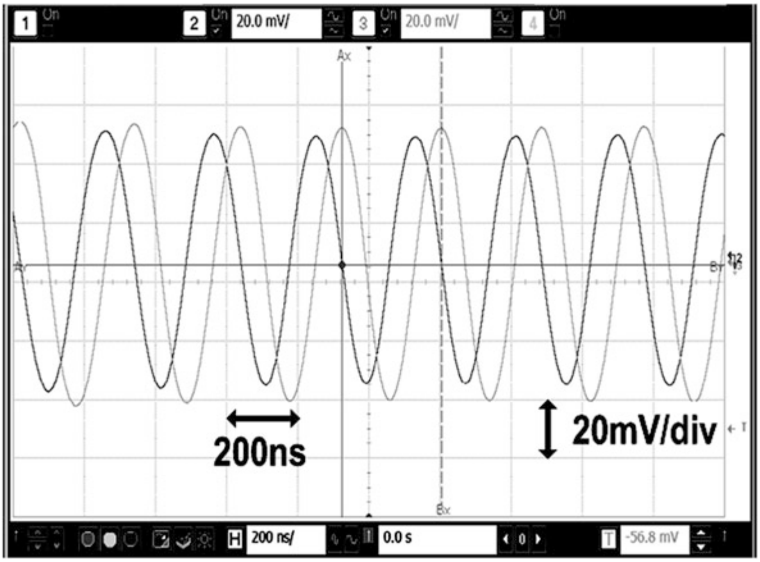

Fig. 2.22 Measured I/Q BB transient outputs

Table 2.2 Performance summary and benchmark with the state-of-the-art

Parameters	JSSC'08 [21]	JSSC'10 [22]	TCAS-I'10 [24]	TMTT'11 [23]	TMTT'11 [26]	TMTT'06 [27]	ISSCC'13 [5]	ISSCC'13 [25]	This work
Gain (dB)	35	67	24.5	51	22.5	30	83	55	32
DSB NF (dB)	7.5	16	16.5 (SSB)	3.2	7 (SSB)	7.3 (SSB)	6.1	9	8.8
Out-band IIP3 (dBm)	–10	–10.5	–19 (in-band data)	–32 (in-band data)	–21.5 (in-band data)	–8	–21.5	–6	–7
SFDR (dB)	58.3	52.3	38.3	36.5	51	59.8	51.6	60	59.4
VCO phase noise (dBc/$\sqrt{\text{Hz}}$)	N/A	–127 @ 3 MHz	N/A	N/A	N/A	N/A	–112 @ 1 MHz	–115 @ 3.5 MHz	–111.4 @ 3.5 MHz
Power (mW)	5.4 (w/o VCO)	32.5 (w/VCO)	2.52 (w/o VCO)	8.1 (w/o VCO)	1.06 (w/o VCO)	1.8 (w/o VCO)	1.6 (w/VCO)	2.7 (w/VCO)	1.4[b] (w/VCO)
No. of inductor or transformer	2	3	3	5	3	2	4	2	1
Die area (mm^2)	0.23 (w/o VCO)	2.88 (w/VCO)	N/A	1.27 (w/o VCO)	1.1 (w/o VCO)	2.07[a] (w/o VCO)	2.5[a] (w/VCO)	0.26[a] (w/VCO)	0.14 (w/VCO)
Supply (V)	1.35	0.6	1.8	1.8	1.2	1.8	0.3	0.6/1.2	0.6/1.2
CMOS Tech.	90 nm	90 nm	0.18 µm	0.18 µm	0.18 µm	0.18 µm	65 nm	65 nm	65 nm

[a]Include more BB gain stages and filters. [b]The power breakdown is LNTA: 0.4 mW, TIA: 0.18 mW and VCO + Buffer: 0.82 mW

2.5 Conclusions

A mixed-V_{DD} 2.4-GHz ZigBee/WPAN receiver measuring state-of-the-art performances has been described. It features passive pre-gain, a split-LNTA, a high-input-impedance BB TIA and a low-power 50 % LO generation scheme. They together lead to improved power and area efficiencies, as well as a high SFDR while eliminating the need of a RF balun. These beneficial features render this work as a superior receiver candidate for cost and power reduction of ZigBee/WPAN radios in nanoscale CMOS.

References

1. P. Choi, H. Park, I. Nam et al., An experimental coin-sized radio for extremely low-power WPAN (IEEE 802.15.4) application at 2.4GHz. IEEE J. Solid-State Circ. **38**, 2258–2268 (2003)
2. C.-H. Li, Y.-L. Liu, C.-N. Kuo, A 0.6-V 0.33-mW 5.5-GHZ receiver front-end using resonator coupling technique. IEEE Trans. Microw. Theory Tech. **59**(6), 1629–1638 (2011)
3. B.W. Cook, A. Berny, A. Molnar et al., Low-power, 2.4-GHz transceiver with passive RX front-end and 400-mV supply. IEEE J. Solid-State Circ. **41**, 2767–2775 (2006)
4. A.C. Herberg, T.W. Brown, T.S. Fiez et al., A 250-mV, 352-μW GPS receiver RF front-end in 130-nm CMOS. IEEE J. Solid-State Circ. **46**, 938–949 (2011)
5. F. Zhang, K. Wang, J. Koo et al., A 1.6mW 300 mV-Supply 2.4 GHz Receiver with –94dBm Sensitivity for Energy-Harvesting Applications, in *ISSCC Digital Technical Papers*, pp. 456–457, Feb 2013
6. A. Mirzaei, H. Darabi, J.C. Leete et al., Analysis and optimization of current-driven passive mixers in narrowband direct-conversion receivers. IEEE J. Solid-State Circ. **44**, 2678–2688 (2009)
7. A. Mirzaei, H. Darabi, J.C. Leete et al., Analysis and optimization of direct-conversion receivers with 25 % duty-cycle current- driven passive mixers. IEEE Trans. Circ. Syst. I, Reg. Papers **57**, 2353–2366 (2010)
8. A. Balankutty, P.R. Kinget, An ultra-low voltage, low-noise, high linearity 900-MHz receiver with digitally calibrated in-band feed-forward interferer cancellation in 65-nm CMOS. IEEE J. Solid-State Circ. **46**, 2268–2283 (2011)
9. Y. Feng, G. Takemura, S. Kawaguchi et al., Digitally assisted IIP2 Calibration for CMOS direct-conversion receivers. IEEE J. Solid-State Circ. **46**, 2253–2267 (2011)
10. P.-I. Mak, R.P. Martins, A 0.46-mm^2 4-dB NF unified receiver front-end for full-band mobile TV in 65-nm CMOS. IEEE J. Solid-State Circ. **46**, 1970–1984 (2011)
11. N. Poobuapheun, W.-H. Chen, Z. Boos et al., A 1.5-V 0.7-2.5-GHz CMOS quadrature demodulator for multiband direct-conversion receivers. IEEE J. Solid-State Circ. **42**, 1669–1677 (2007)
12. C. Andrews, A.C. Molnar, A passive mixer-first receiver with digitally controlled and widely tunable RF interface. IEEE J. Solid-State Circ. **45**, 2696–2708 (2010)
13. C. Andrews, A.C. Molnar, Implications of passive mixer transparency for impedance matching and noise figure in passive mixer-first receivers. IEEE Trans. Circ. Syst. I, Reg. Papers **57**, 3092–3103 (2010)
14. A. Molnar, C. Andrews, Impedance, Filtering and Noise in N-phase Passive CMOS Mixers, in *Proceedings of IEEE CICC*, pp. 1–8, Sept 2012

15. J. Kaykovuori, K. Stadius, J. Ryynanen, Analysis and design of passive polyphase filters. IEEE Trans. Circ. Syst. I, Reg. Papers **55**, 3023–3037 (2008)
16. F. Behbahani, Y. Kishigami, J. Leete et al., CMOS mixers and polyphase filters for large image rejection. IEEE J. Solid-State Circ. **36**, 873–887 (2001)
17. A. Liscidini, M. Tedeschi, R. Castello, Low-power quadrature receivers for ZigBee (IEEE 802.15.4) applications. IEEE J. Solid-State Circ. **45**, 1710–1719 (2010)
18. T.H. Lee, in *The Design of CMOS Radio-Frequency Integrated Circuits*, 2nd edn. (Cambridge University Press, Cambridge, 2004)
19. B. Razavi, *RF Microelectronics*, 2nd edn. (Prentice-Hall, Upper Saddle River, 2011)
20. W. Kluge, F. Poegel, H. Roller et al., A fully integrated 2.4-GHz IEEE 802.15.4-compliant transceiver for ZigBee TM applications. IEEE J. Solid-State Circ. **41**, 2767–2775 (2006)
21. M. Camus, B. Butaye, L. Garcia et al., A 5.4mW/0.07 mm^2 2.4 GHz front-end receiver in 90 nm CMOS for IEEE 802.15.4 WPAN stand. IEEE J. Solid-State Circ. **43**, 1372–1383 (2008)
22. A. Balankutty, S. Yn, Y. Feng et al., A 0.6-V Zero-IF/Low-IF receiver with integrated fractional-N synthesizer for 2.4-GHz ISM-band applications. IEEE J. Solid-State Circ. **45**, 538–553 (2010)
23. J.-S. Syu, C. Meng, C.-L. Wang, 2.4-GHz low-noise direct- conversion receiver with deep N-well vertical-NPN BJT operating near cutoff frequency. IEEE Trans. Microw. Theory Tech. **45**, 538–553 (2010)
24. J. Kaykovuori, K. Stadius, J. Ryynanen, An energy-aware CMOS receiver front end for low-power 2.4-GHz applications. IEEE Trans. Circ. Syst. I, Reg. Papers **57**, 2675–2684 (2010)
25. Z. Lin, P.-I. Mak, R.P. Martins, A 1.7mW 0.22 mm^2 2.4 GHz ZigBee RX Exploiting a Current-Reuse Blixer + Hybrid Filter Topology in 65 nm CMOS, in *ISSCC Digital Technical Papers*, pp. 448–449, Feb 2013
26. J.L. Gonzalez, H. Solar, I. Adin et al., A 16-kV HBM RF ESD protection codesign for a 1-mW CMOS direct conversion receiver operating in the 2.4-GHz ISM band. IEEE Trans. Microw. Theory Tech. **59**, 2318–2330 (2011)
27. T.-K. Nguyen, V. Krizhanovskii, J. Lee et al., A low-power RF direct-conversion receiver/transmitter for 2.4-GHz-band IEEE 802.15.4 standard in 0.18 μm CMOS technology. IEEE Trans. Microw. Theory Tech. **54**, 4062–4071 (2006)
28. Z. Lin, P.-I. Mak, R.P. Martins, A 0.14-mm^2, 1.4-mW, 59.4 dB-SFDR, 2.4-GHz ZigBee/WPAN receiver exploiting a “Split-LNTA + 50 % LO” topology in 65-nm CMOS. IEEE Trans. Microw. Theory Tech. **62**, 1525–1534 (2014)

Chapter 3
A 2.4-GHz ZigBee Receiver Exploiting an RF-to-BB-Current-Reuse Blixer + Hybrid Filter Topology in 65-nm CMOS

3.1 Introduction

Ultra-low-power (ULP) radios have essentially underpinned the development of short-range wireless technologies [1] such as personal/body-area networks and Internet of Things. The main challenges faced by those ULP radios are the stringent power and area budgets, and the pressure of minimum external components to save cost and system volume. Balancing them with the performance metrics such as noise figure (NF), linearity and input matching involves many design tradeoffs at both architecture and circuit levels.

Ultra-low-voltage receivers have been extensively studied for short-range ZigBee, Bluetooth and energy-harvesting applications [2–5]. Yet, the lack of voltage headroom will limit the signal swing and transistor's f_T, imposing the need of bulky inductors or transformers to facilitate the biasing and tune out the parasitics. Thus, the die area is easily penalized, such as 5.76 mm^2 in [4] and 2.5 mm^2 in [5]. In fact, the current-reuse topologies should benefit more from technology scaling when the NF is less demanding. Advanced process nodes such as 65-nm CMOS feature sufficiently high-f_T and low-V_T transistors for GHz circuits to operate at very small bias currents. Unsurprisingly, when cascoding the building blocks for current reuse, such as the low-noise amplifier (LNA) plus mixer [6], the RF bandwidth and linearity can be improved as well, by avoiding any high-impedance nodes at their interface.

Several NF-relaxed current-reuse receivers have been reported. The LNA-Mixers-VCO (LMV) cell [7] is illustrated in Fig. 3.1. Sharing the bias current among more blocks successfully saves the power (2.4 mW), but the NF, gain and S_{11} are sensitive to its external high-Q inductor (L_{ext}) for narrowband input matching and passive pre-gain. Also, under the same bias current, it is hard to optimize the LNA's NF (RF path) with the phase noise of the VCO (LO path). Finally, although a single VCO can save area, the narrow-band I/Q generation has

Z. Lin et al., *Ultra-Low-Power and Ultra-Low-Cost Short-Range Wireless Receivers in Nanoscale CMOS*, Analog Circuits and Signal Processing,
DOI 10.1007/978-3-319-21524-2_3

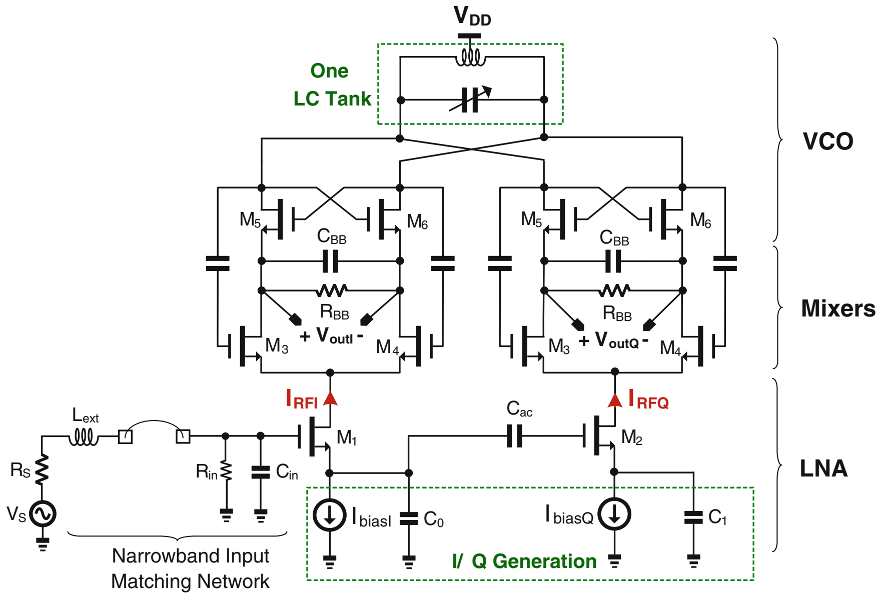

Fig. 3.1 LMV cell [6]. L_{ext} is external for *narrowband* input matching and pre-gain. One LC-tank VCO saves the chip area, but putting the I/Q generation in the LNA (M_1–M_2) degrades NF. Only single-balanced mixers (M_3–M_4) can be used

to be embedded into the LNA, rendering the I/Q accuracy more susceptible to process variations.

To return the I/Q generation back to the LO path, [8] adopted two VCOs to tailor a quadrature LMV (QLMV) cell. Although its power is further optimized (1 mW), three on-chip inductors and one off-chip balun are entailed, penalizing the die size and system cost. Also, both LMV and QLMV cells share the same pitfall that only a 50 %-duty-cycle LO (50 % LO) can be used for the mixing, which is less effective than 25 % LO in terms of gain (i.e., 3 dB higher), NF and I/Q isolation [6]. Finally, as their baseband (BB) channel selection and image rejection are out of their current-reuse paths, any large out-band blockers will be converted into voltages before filtering. This fact constitutes a hard tradeoff between noise, linearity and power (i.e., 1.2-mW BB power in [7] and 5.2-mW BB power in [8]).

Another example is the current-reuse circuit-reuse receiver reported in [9] which merges the RF LNA and BB transimpedance amplifier (TIA) in one cell Fig. 3.2a. A conceptual view of its operation is given in Fig. 3.2b. Without the VCO, and by using passive mixers, this topology can reserve more voltage headroom for the dynamic range. A RF balun is nevertheless entailed for its fully-differential operation, and several constraints limit its NF and linearity: (1) the LNA and TIA must be biased at the same current; (2) the LNA's NF should benefit more from short-channel devices for M_{1-2}, but the BB TIA prefers long-channel transistors to

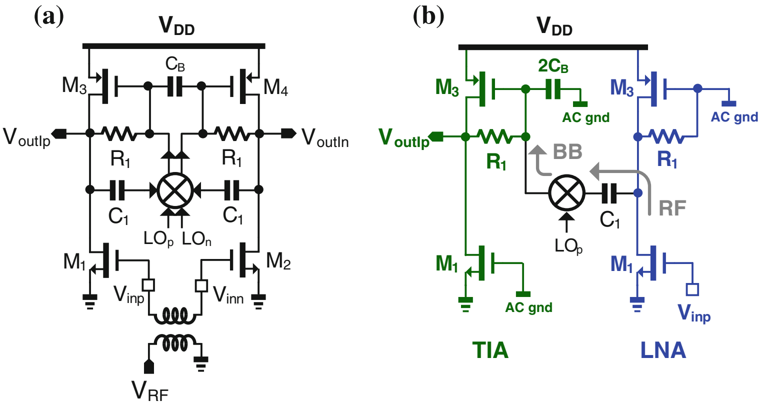

Fig. 3.2 **a** Circuit-reuse receiver merging RF LNA and BB TIA [9]. **b** Its single-ended equivalent circuit illustrating its RF-to-BB operation conceptually (from *right* to *left*)

lower the 1/f noise; and (3) any out-band blockers will be amplified at the LNA's (TIA's) output before deep BB filtering.

This chapter describes the details of an extensive-current-reuse ZigBee receiver [10] with most RF-to-BB functions merged in one cell, while avoiding any external components for input-impedance matching. Together with a number of ULP circuits and optimization techniques, the receiver fabricated in 65-nm CMOS measures high performances in terms of IIP3, S_{11}-bandwidth, power and area efficiencies with respect to the prior art.

Section 3.2 overviews the receiver architecture. Section 3.3 details the implementation of key building blocks. Measurement results and performance benchmarks are summarized in Sect. 3.4, and conclusions are drawn in Sect. 3.5.

3.2 Proposed Current-Reuse Receiver Architecture

The block diagram is depicted in Fig. 3.3. As discussed above and detailed in [8] for the QLMV cell, merging the LO path with the signal path is not that desirable, as they will add noise to each other and induce signal loss. In fact, stacking of building blocks should be in conformity with the signal flow from RF to BB, such that all bias currents serve only the signal currents. In this work, the LO path is separated, which also facilitates the use of a 25 % LO for better overall performance than in its 50 % counterpart. The single-ended RF input (VRF) is taken by a low-Q input-matching network before reaching the Balun-LNA-I/Q-Mixer (Blixer). Merging the latter with the hybrid filter not only saves power, but also reduces the voltage swing at internal nodes benefitting the linearity. The wideband input-matching network is also responsible for the pre-gain to enhance the NF. Unlike the LMV cell that only can utilize single-balanced mixers [7], here the

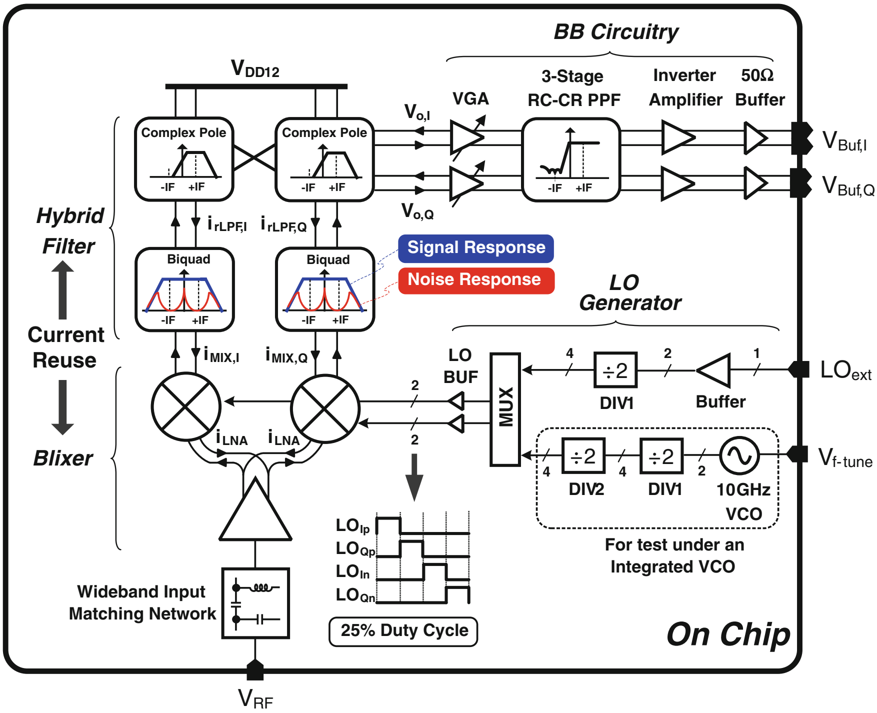

Fig. 3.3 Proposed RF-to-BB-current-reuse ZigBee receiver

balun-LNA featuring a differential output ($\pm i_{LNA}$) allows the use of double-balanced mixers (DBMs). Driven by a 4-phase 25 % LO, the I/Q-DBMs with a large output resistance robustly correct the differential imbalances of $\pm i_{LNA}$. The balanced BB currents ($\pm i_{MIX,I}$ and $\pm i_{MIX,Q}$) are then filtered directly in the current domain by a current-mode Biquad stacked atop the DBM. The Biquad features in-band noise-shaping centered at the desired intermediate frequency (IF, 2 MHz). Only the filtered output currents ($\pm i_{rLPF,I}$ and $\pm i_{rLPF,Q}$) are returned as voltages ($\pm V_{o,I}$ and $\pm V_{o,Q}$) through the complex-pole load, which performs both image rejection and channel selection. Out of the current-reuse path there is a high-swing variable-gain amplifier (VGA). It essentially deals with the gain loss of its succeeding 3-stage RC-CR polyphase filter (PPF), which is responsible for large and robust image rejection over mismatches and process variations. The final stage is an inverter amplifier before 50-Ω test buffering. The 4-phase 25 % LO can be generated by an external 4.8-GHz reference (LO_{ext}) after a divide-by-2 (DIV1) that features 50 %-input 25 %-output, or from an integrated 10-GHz VCO after DIV1 and DIV2 (25 %-input 25 %-output) for additional testability.

3.3 Circuit Implementation

3.3.1 Wideband Input-Matching Network

Its schematic is illustrated in Fig. 3.4a. A low-Q inductor (L_M) and two tapped capacitors (C_p and C_M) are employed for impedance down-conversion resonant and passive pre-gain. A high-Q inductor is unnecessary since the Q of the LC matching is dominated by the low input resistance of the LNA. Thus, a low-Q inductor results in area savings, while averting the need of an external inductor for cost savings. L_M also serves as the bias inductor for M_1. R_p is the parallel shunt resistance of L_M. C_p stands for the parasitic capacitance from the pad and ESD diodes. R_{in} and C_{in} are the equivalent resistance and capacitance at node V_{in}, respectively. R'_{in} is the down-conversion resistance of R_{in}. L_{BW} is the bondwire inductance and R_s is the source resistance. To simplify the analysis, we first omit L_{BW} and C_{in}, so that L_M, C_p, C_M, R_S and R_T (=R_p//R_{in}) together form a tapped capacitor facilitating the input matching. Generally, $S_{11} \leq -10$ dB is required and the desired value of R'_{in} is from 26 to 97 Ω over the frequency band of interest. Thus, given the R_T and C_M values, the tolerable C_p can be derived from $R'_{in} = R_T\left(\frac{C_M}{C_M+C_p}\right)^2$. The pre-gain value ($A_{pre,amp}$) from V_{RF} to V_{in} is derived from $\frac{V_{in}^2}{2R_T} = \frac{V_{RF}^2}{2R_S}$, which can be simplified as $A_{pre,amp} = \sqrt{\frac{R_T}{R_S}}$. The –3-dB bandwidth of $A_{pre,amp}$ is related to the network's quality factor (Q_n) as given by: $Q_n = \frac{R_T}{2\omega_0 L_M} = \frac{\omega_0}{\omega_{-3dB}}$, with $\omega_0 = \frac{1}{\sqrt{L_M C_{EQ}}}$ and $C_{EQ} = \frac{C_M C_p}{C_M+C_p}$.

In our design (R_T = 150 Ω, C_M = 1.5 pF, L_M = 4.16 nH, R_p = 600 Ω, C_p = 1pF and R_{in} = 200 Ω), $A_{pre,amp}$ has a passband gain of ∼4.7 dB over a 2.4-GHz bandwidth (at RF = 2.4 GHz) under a low Q_n of 1. Thus, the tolerable C_p is sufficiently wide (0.37–2.1 pF). The low-Q L_M is extremely compact (0.048 mm^2) in the layout and induces a small parasitic capacitance (∼260 fF, part of C_{in}). Figure 3.4b demonstrates the robustness of S_{11}-bandwidth against L_{BW} from 0.5 to 2.5 nH. The variation of C_{in} to S_{11}-bandwidth was also studied. From simulations, the tolerable C_{in} is 300–500 fF at L_{BW} = 1.5 nH. The correlation between S_{11}-bandwidth and Q_n is derived in Appendix A.

3.3.2 Balun-LNA with Active Gain Boost and Partial Noise Canceling

The common-gate (CG) common-source (CS) balun-LNA [11] avoids the off-chip balun and achieves a low NF by noise canceling, but the asymmetric CG-CS transconductances and loads make the output balancing not wideband consistent. Both [6, 12] have addressed this issue. In [6], output balancing is achieved by scaling M_{5-8} with cross-connection at BB, but that is incompatible with this work

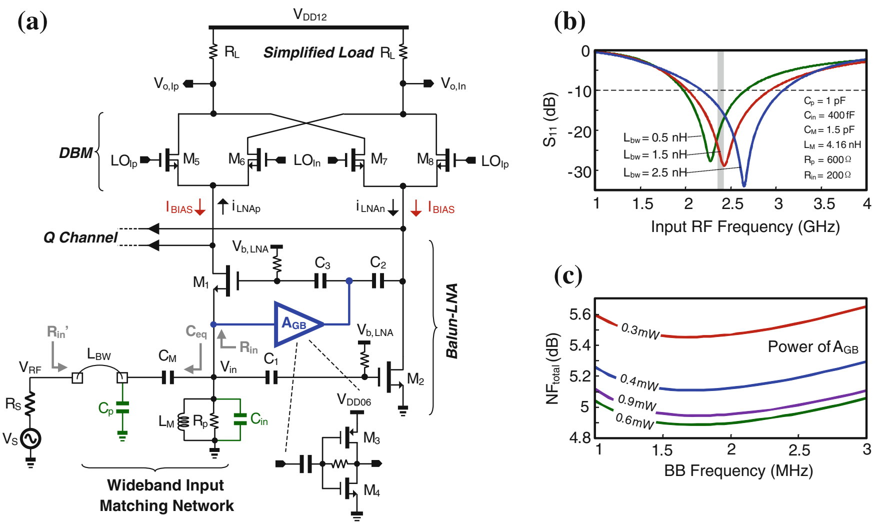

Fig. 3.4 **a** Proposed wideband input matching network, balun-LNA and I/Q-DBMs (Q channel is omitted and the load is simplified as R_L). **b** Variation of S_{11}-bandwidth with bondwire inductance L_{BW}. **c** Power of A_{GB} versus NF

that includes a hybrid filter. In [12], by introducing an AC-coupled CS branch and a differential current balancer (DCB), the same load is allowed for both CS and CG branches for wideband output balancing. Thus, the NF of such a balun-LNA can be optimized independently. This technique is transferred to this ULP design, but only with the I/Q-DBMs inherently serving as the DCB, avoiding a high voltage supply [12]. The detailed schematic is depicted in Fig. 3.4a. To maximize the voltage headroom, M_1 (with $g_{m,CG}$) and M_2 (with $g_{m,CS}$) were sized with non-minimum channel length (L = 0.18 μm) to lower their V_T. The AC-coupled gain stage is a self-biased inverter amplifier (A_{GB}) powered at 0.6-V (V_{DD06}) to enhance its transconductance ($g_{m,AGB}$)-to-current ratio. It gain-boosts the CS branch while creating a loop gain around M_1 to enhance its effective transconductance under less bias current (I_{BIAS}). This scheme also allows the same I_{BIAS} for both M_1 and M_2, requiring no scaling of load (i.e., only R_L). Furthermore, a small I_{BIAS} lowers the supply requirement, making a 1.2-V supply (V_{DD12}) still adequate for the Blixer and hybrid filter, while relaxing the required LO swing (L_{OIP} and L_{OIn}). $C_{1\text{-}3}$ for biasing are typical metal-oxide-metal (MoM) capacitors to minimize the parasitics.

The balun-LNA features partial-noise canceling. To simplify the study, we ignore the noise induced by DBM (M_5–M_8) and the effect of channel-length modulation. The noise transfer function (TF) of M_1's noise ($I_{n,CG}$) to the BB differential output ($V_{o,Ip}$–$V_{o,In}$) can be derived when LO_{Ip} is high, and the input impedance is matched,

$$\mathrm{TF}_{\mathrm{I_{n,CG}}} = -\frac{1}{2}\left(\mathrm{R_L} - \mathrm{R_{in}G_{m,CS}R_L}\right) \tag{3.1}$$

where $G_{m,CS} = g_{m,CS} + g_{m,AGB}$. The noise of M_1 can be fully canceled if $R_{in}G_{m,CS} = 1$ is satisfied. However, as analyzed in Sect. 3.3.1, $R_{in} \approx 200\ \Omega$ is desired for input matching at low power. Thus, $G_{m,CS}$ should be ≈5 mS, rendering the noises of $G_{m,CS}$ and R_L still significant. Thus, device sizing for full noise cancellation of M_1 should not lead to the lowest total NF (NF_{total}). In fact, a more optimized $G_{m,CS}$ can be obtained (via $g_{m,AGB}$) for stronger reduction of noise from $G_{m,CS}$ and R_L, instead of that from M_1. Although this noise-canceling principle has been discussed in [13] for its single-ended LNA, the output balancing was not a concern there. In this work, the optimization process is alleviated since the output balancing and NF are decoupled. The simulated NF_{total} up to the $V_{o,Ip}$ and $V_{o,In}$ nodes against the power given to the A_{GB} is given in Fig. 3.4c. NF_{total} is reduced from 5.5 dB at 0.3 mW to 4.9 dB at 0.6 mW, but is back to 5 dB at 0.9 mW. Due to the use of passive pre-gain and a larger R_p that is ~3 times of R_{in}, the noise contribution of the inductor is <1 % from simulations. The simulated NF at the outputs of the LNA and test buffer are 5.3 and 6.6 dB, respectively. The relationship of $G_{m,CS}$ and NF_{total} is derived in Appendix B, which is also applicable to the balun-LNA in [12].

3.3.3 Double-Balanced Mixers Offering Output Balancing

As analyzed in [12] the active-gain-boosted balun-LNA can only generate unbalanced outputs. Here, the output balancing is inherently done by the I/Q-DBMs under a 4-phase 25 % LO. For simplicity, this principle is described for the I channel only under a 2-phase 50 % LO, as shown in Fig. 3.5, where the load is simplified as R_L. During the first-half LO cycle when LO_{Ip} is high, i_{LNAp} goes up and appears at $V_{o,Ip}$ while i_{LNAn} goes down and appears at $V_{o,In}$. In the second-half

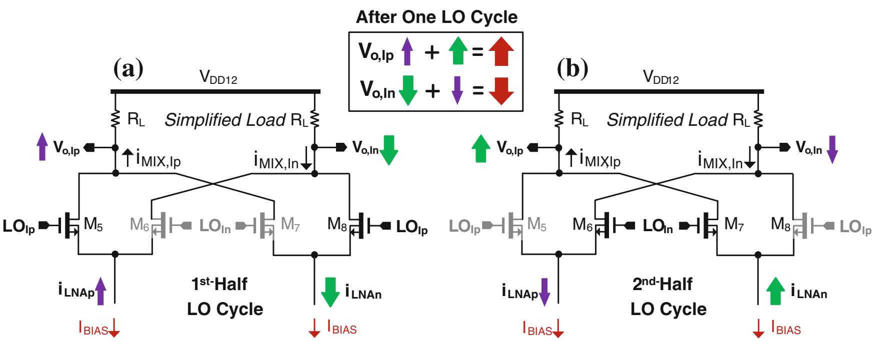

Fig. 3.5 Operation of the I-channel DBM. It inherently offers output balancing after averaging in one LO cycle as shown in their **a** 1st-half LO cycle and **b** 2nd-half LO cycle

LO cycle, both of the currents' sign and current paths of i_{LNAp} and i_{LNAn} are flipped. Thus, when they are summed at the output during the whole LO cycle, the output balancing is robust, thanks to the large output resistance (9 kΩ) of M_5–M_8 enabled by the very small I_{BIAS} (85 μA). To analytically prove the principle, we let $i_{LNAp} = \alpha I_A \cos(\omega_s t + \varphi_1)$ and $i_{LNAn} = -I_A \cos(\omega_s t + \varphi_2)$, where I_A is the amplitude, ω_s is the input signal frequency, α. The unbalanced gain factor and φ_1 and φ_2 are their arbitrary initial phases. When there is sufficient filtering to remove the high-order terms, we can deduce the BB currents $i_{MIX,Ip}$ and $i_{MIX,In}$ as given by,

$$
\begin{aligned}
i_{MIX,Ip} &= \frac{2}{\pi}\alpha I_A \cos(\omega_s t + \varphi_1) \times \cos\omega_0 t + \frac{2}{\pi} I_A \cos(\omega_s t + \varphi_2) \times \cos\omega_0 t \\
&= \frac{\alpha I_A}{\pi}\cos(\omega_s t - \omega_0 t + \varphi_1) + \frac{I_A}{\pi}\cos(\omega_0 t - \omega_s t + \varphi_2)
\end{aligned} \tag{3.2}
$$

$$
i_{MIX,In} = -\frac{I_A}{\pi}\cos(\omega_s t - \omega_0 t + \varphi_2) - \frac{\alpha I_A}{\pi}\cos(\omega_0 t - \omega_s t + \varphi_1) = -i_{MIX,Ip} \tag{3.3}
$$

and a consistent proof for I/Q-DBMs under a 4-phase 25 % LO is obtained. Ideally, from (3.2) to (3.3), the DBM can correct perfectly the gain and phase errors from the balun-LNA, independent of its different output impedances from the CG and CS branches. In fact, even if the conversion gain of the two mixer pairs (M_5, M_8 and M_6, M_7) does not match (e.g., due to non-50 % LO duty cycle), the double-balanced operation can still generate balanced outputs (confirmed by simulations). Of course, the output impedance of the DBM can be affected by that of the balun-LNA Fig. 3.4a, but is highly desensitized due to the small size of R_L (i.e., the input impedance of the hybrid filter) originally aimed for current-mode operation. Thus, the intrinsic imbalance between $V_{o,\,Ip}$ and $V_{o,\,In}$ is negligibly small (confirmed by simulations).

For devices sizing, a longer channel length (L = 0.18 μm) is preferred for $M_{5\text{–}8}$ to reduce their 1/f noise and V_T. Hard-switch mixing helps to desensitize the I/Q-DBMs to LO gain error, leaving the image rejection ratio (IRR) mainly determined by the LO phase error that is a tradeoff with the LO-path power. Here, the targeted LO phase error is relaxed to ~4°, as letting the BB circuitry (i.e., the complex-pole load and 3-stage RC-CR PPF) to handle the IRR is more power efficient, as detailed in Sects. 3.3.5 and 3.3.6.

3.3.4 Hybrid Filter 1st Half—Current-Mode Biquad with IF Noise-Shaping

The current-mode Biquad Fig. 3.6a proposed in [14] is an excellent candidate for current-reuse with the Blixer for channel selection. However, this Biquad only can generate a noise-shaping zero spanning from DC to $\sim 2\pi 0.1 Q_B \omega_{0B}$ MHz for M_{f1}–M_{f2},

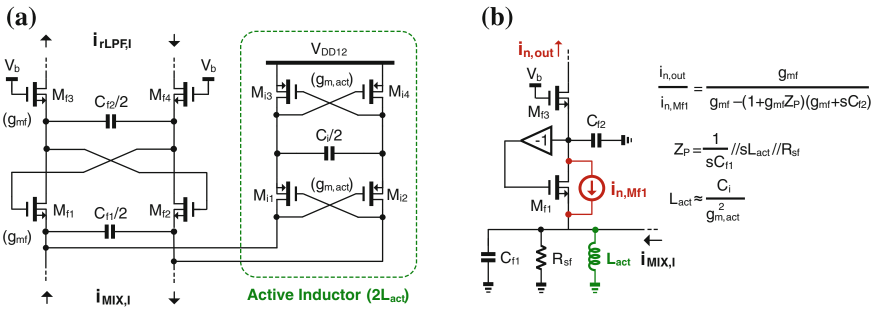

Fig. 3.6 **a** Proposed IF-noise-shaping Biquad and **b** its small-signal equivalent circuit showing the noise TF of M_{f1}

where Q_B and ω_{0B} are the Biquad's quality factor and –3-dB cutoff frequency, respectively. This noise shaping is hence ineffective for our low-IF design having a passband from ω_1 to ω_2 ($=\omega_{0B}$), where $\omega_1 > 0.1Q_B\omega_{0B}$. To address this issue, an active inductor (L_{act}) is added at the sources of M_{f1}–M_{f2}. The $L_{act}C_{f1}$ resonator shifts the noise-shaping zero to the desired IF. The cross-diode connection between M_{i1}–M_{i4} (all with $g_{m,act}$) emulate $L_{act} \approx C_i/g_{m,act}^2$ [15, 16]. The small-signal equivalent circuit to calculate the noise TF of $i_{n,Mf1}/i_{n,out}$ is shown in Fig. 3.6b. The approximated impedance of Z_P in different frequencies related to ω_{0r} is summarized in Fig. 3.7a, where $\omega_{0r} = \frac{\omega_1+\omega_2}{2}$ is the resonant frequency of $L_{act}C_{f1}$ at IF. The simulated $i_{n,Mf1}/i_{n,out}$ is shown in Fig. 3.7b. At the low frequency range, Z_P behaves inductively, degenerating further $i_{n,Mf1}$ when the frequency is increased. At the resonant frequency, $Z_P = R_{sf}$, where R_{sf} is the parallel impedance of the active inductor's shunt resistance and DBM's output resistance. The latter is much higher when compared with R_L thereby suppressing $i_{n,Mf1}$. At the high frequency range, Z_P is more capacitive dominated by C_{f1}. It implies $i_{n,Mf1}$ can be leaked to the output via C_{f1}, penalizing the in-band noise. At even higher frequencies, the output noise decreases due to C_{f2}, being the same as its original form [14].

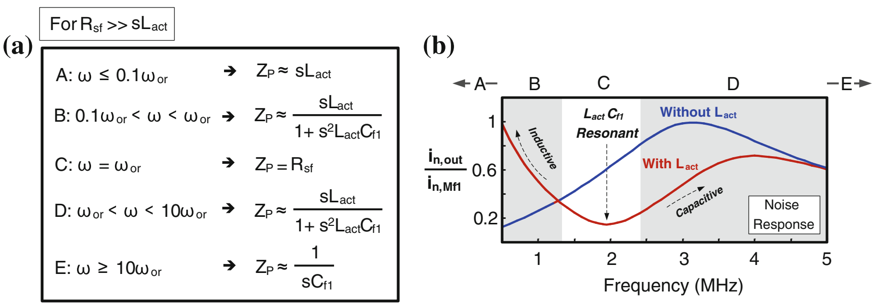

Fig. 3.7 **a** Equivalent impedance of Z_P versus ω_{or}, and **b** simulated noise TF of $\frac{i_{n,out}}{i_{n,Mf1}}$ with and without L_{act}

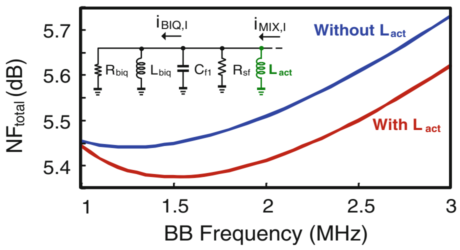

Fig. 3.8 Simulated NF_{Total} (at $V_{o,Ip}$ and $V_{o,In}$) with and without L_{act}

The signal TF can be derived from Fig. 3.8. Here $R_L = \frac{1}{g_{mf}}, L_{biq} = \frac{C_{f2}}{g_{mf}^2}$. For an effective improvement of NF, $L_{act} >> L_{biq}$ should be made. The simulated NF_{total} at $V_{o,Ip}$ and $V_{o,In}$ with and without the L_{act} is shown Fig. 3.8, showing about 0.1 dB improvement at the TT corner (reasonable contribution for a BB circuit). For the SS and FF corners, the NF improvement reduces to 0.04 and 0.05 dB, respectively. These results are expected due to the fact that at the FF corner, the noise contribution of the BB is less significant due to a larger bias current; while at the SS corner, the IF noise-shaping circuit will add more noise by itself, offsetting the NF improvement. Here M_{f1}–M_{f4} use isolated P-well for bulk-source connection, avoiding the body effect while lowering their V_T.

3.3.5 Hybrid Filter 2nd Half—Complex-Pole Load

Unlike most active mixers or the original Blixer [6] that only use a RC load, the proposed "load" synthesizes a 1st-order complex pole at the positive IF (+IF) for channel selection and image rejection. The circuit implementation and principle are shown in Fig. 3.9a, b, respectively. The real part (R_L) is obtained from the diode-connected M_L, whereas the imaginary part ($g_{m,Mc}$) is from the I/Q-cross-connected M_C. The entire hybrid filter (i.e., Figs. 3.7a and 3.9b) offers 5.2-dB IRR, and 12-dB (29-dB) adjacent (alternate) channel rejection as shown in Fig. 3.10 (the channel spacing is 5 MHz). Similar to g_m-C filters the center frequency is defined by $g_{m,Mc}R_L$. When sizing the –3-dB bandwidth, the output conductances of M_C and M_L should be taken into account.

3.3.6 Current-Mirror VGA and RC-CR PPF

Outside the current-reuse path, $V_{o,I}$ and $V_{o,Q}$ are AC-coupled to a high swing current-mirror VGA formed with M_L (Fig. 3.9a) and a segmented M_{VGA} (Fig. 3.11), offering gain controls with a 6-dB step size. To enhance the gain

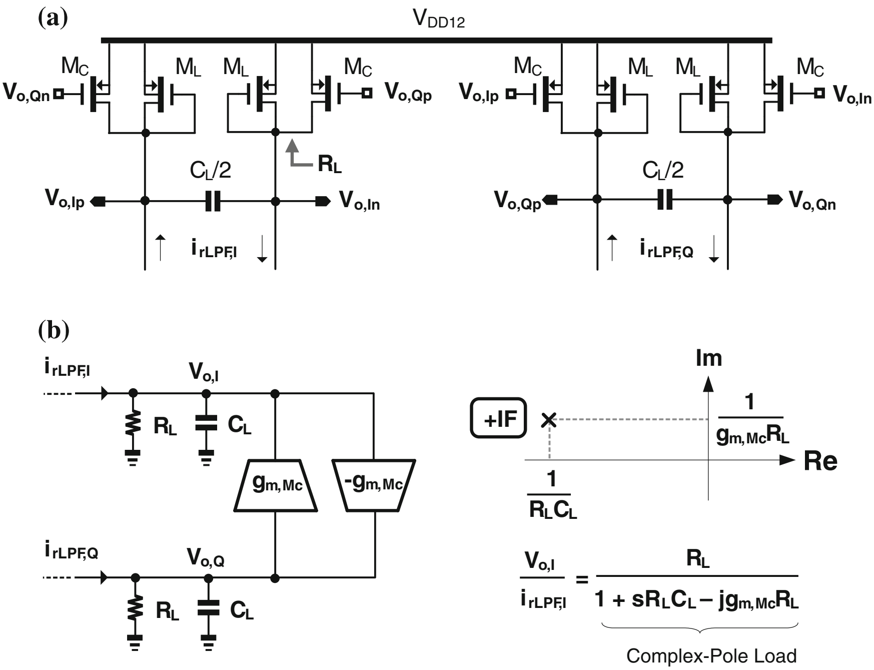

Fig. 3.9 **a** Proposed complex-pole load and **b** its small-signal equivalent circuit and pole plot

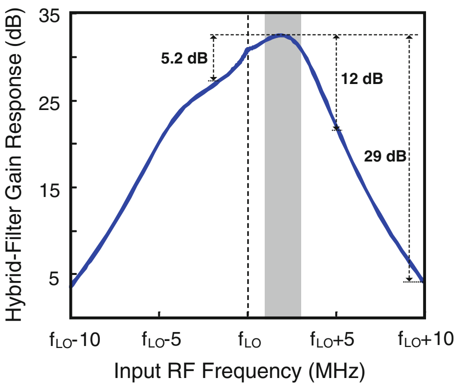

Fig. 3.10 Simulated hybrid-filter gain response

precision, the bias current through M_{VGA} is kept constant, so as its output impedance. With the gain switching of M_{VGA}, the input-referred noise of M_{VGA} will vary. However, when the RF signal level is low the gain of the VGA should be high, rendering the gain switching not influencing the receiver's sensitivity. The VGA is responsible for compensating the gain loss (30 dB) of the 3-stage passive RC-CR PPF that provides robust image rejection of >50 dB (corner

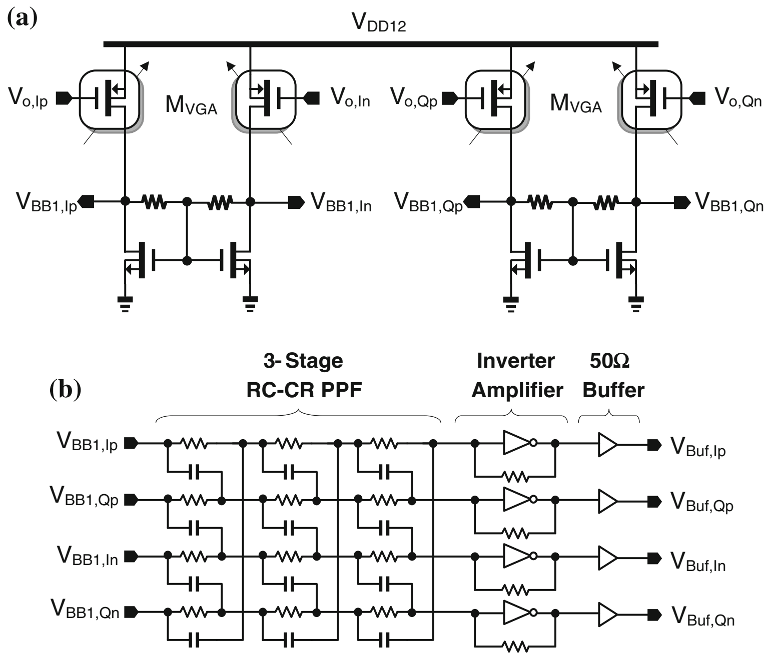

Fig. 3.11 Schematics of the BB **a** VGA, and **b** 3-stage RC-CR PPF, inverter amplifier and 50-Ω buffer

simulations). With the hybrid filter rejecting the out-band blockers the linearity of the VGA is further relaxed, so as its power budget (192 μW, limited by the noise and gain requirements).

A 3-stage RC-CR PPF can robustly meet the required IRR in the image band (i.e., the -IF), and cover the ratio of maximum to minimum signal frequencies [17, 18]. In our design, the expected IRR is 30–40 dB and the ratio of frequency of the image band is f_{max}/f_{min} (=3). However, counting the RC variations as large as ±25 %, the conservative $\Delta f_{eff} = f_{max\_eff}/f_{min\_eff}$ should be close to 5. The selected RC values are guided by [18]

$$\frac{\sigma(\text{Image Out})}{\text{Desired Out}} = 0.25\sqrt{\left(\frac{\sigma_R}{R}\right)^2 + \left(\frac{\sigma_C}{C}\right)^2} \tag{3.4}$$

Accordingly, the matching of the resistors (σ_R) and capacitors (σ_C) can be relaxed to 0.9 % (2.93 %) for 40-dB (30-dB) IRR with a 3σ yield. Here, ~150-kΩ resistors are chosen to ease the layout with a single capacitor size (470 fF), balancing the noise, area and IRR. The simulated worst IRR is 36 dB without LO mismatch, and still over 27 dB at a 4° LO phase error checked by 100× Monte-Carlo simulations. Furthermore, if the 5-dB IRR offered by the complex-pole load is added the minimum IRR of the IF chain should be 32 dB.

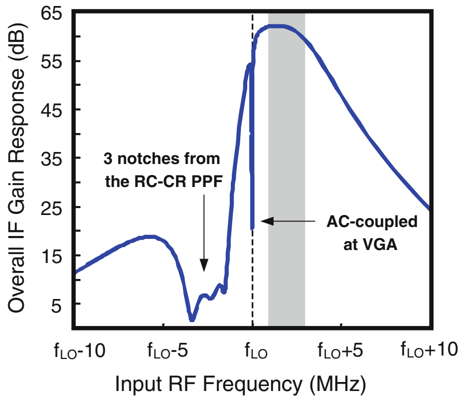

Fig. 3.12 Simulated overall IF gain response

The final stage before 50-Ω output buffering is a self-biased inverter amplifier (power = 144 μW), which embeds one more real pole for filtering. The simulated overall IF gain response is shown in Fig. 3.12, where the notches at DC offered by the AC-coupling network, and around the -IF offered by the 3-stage RC-CR PPF, are visible. The IRR is about 57 dB [=52 dB (RC-CR PPF) +5 dB (complex-pole load)] under an ideal 4-phase 25 % LO for the image band from (f_{LO} − 3, f_{LO} − 1) MHz.

3.3.7 VCO, Dividers and LO Buffers

To fully benefit the speed and low-V_T advantages of fine linewidth CMOS, the entire LO path is powered at a lower supply of 0.6 V to reduce the dynamic power. For additional testability, an on-chip VCO is integrated. It is optimized at ~10 GHz to save area and allows division by 4 for I/Q generation. The loss of its LC tank is compensated by complementary NMOS-PMOS negative transconductors.

The divider chain (Fig. 3.13a) cascades two types of div-by-2 circuits (DIV1 and DIV2) to generate the desired 4-phase 25 % LO, from a 2-phase 50 % output of the VCO. The two latches (D1 and D2) are employed to build DIV1 that can directly generate a 25 % output from a 50 % input [19], resulting in power savings due to less internal logic operation (i.e. AND gates [20]) and load capacitances. Each latch consists of two sense devices, a regenerative loop and two pull up devices. For 25 %-input 25 %-output division, DIV2 is proposed that it can be directly interfaced with DIV1. The 25 % output of DIV1 are combined by M_{D1}–M_{D4} to generate a 50 % clock signal for D3 and D4.

For testing under an external LO_{ext} source at 4.8 GHz, another set of D1 and D2 is adopted. The output of these two sets of clocks are combined by transmission gates and then selected. Although their transistor sizes can be reduced aggressively to save power, their drivability and robustness in process corners can be degraded.

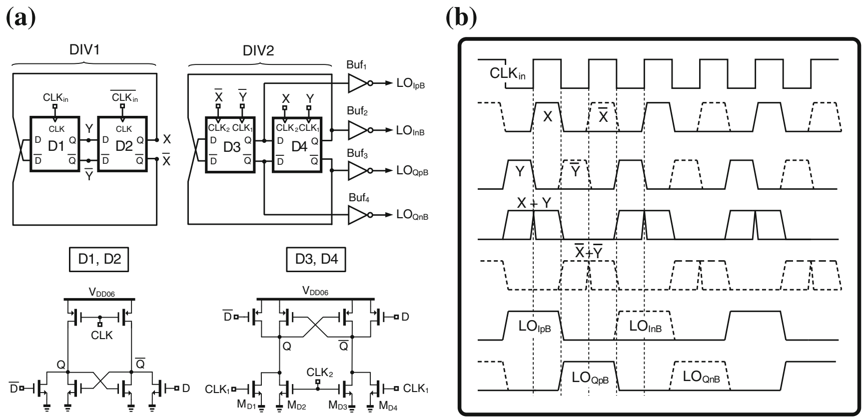

Fig. 3.13 **a** Schematics of DIV1 and DIV2, and **b** their timing diagrams

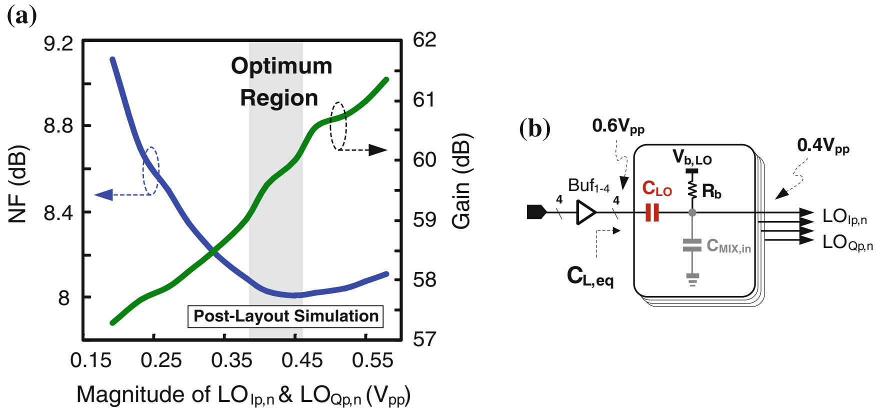

Fig. 3.14 **a** Post-layout simulation of NF and gain versus LO's amplitude, and **b** additional C_{LO} generates the optimum LO's amplitude

From simulations, the sizing can be properly optimized. The four buffers ($Buf_{1–4}$) serve to reshape the pulses from DIV2 and enhance the drivability. The timing diagram is shown in Fig. 3.13b. Due to the very small I_{BIAS} for the I/Q-DBMs, a LO amplitude of around 0.4 V_{pp} is found to be more optimized in terms of NF and gain as simulated and shown in Fig. 3.14a. To gain benefits from it C_{LO} is added to realize a capacitor divider with $C_{MIX,in}$ (input capacitance of the mixer) as shown in Fig. 3.14b. This act brings down the equivalent load ($C_{L,eq}$) of $Buf_{1–4}$ by $\sim$33 %.

3.4 Experimental Results

The ZigBee receiver was fabricated in 65-nm CMOS (Fig. 3.15) and optimized with dual supplies (1.2 V: Blixer + hybrid filter, 0.6 V: LO and BB circuitries). The die area is 0.24 mm^2 (0.3 mm^2) without (with) counting the LC-tank VCO. Since there is no frequency synthesizer integrated, the results in Fig. 3.16a–d were measured under LO_{ext} for accuracy and data repeatability. The S_{11}-BW (≤10 dB) is ~1.3 GHz for both chip-on-board (CoB) and CQFP-packaged tests (Fig. 3.16a), which proves its immunity to board parasitics and packaging variations. The gain (55–57 dB) and NF (8.3–11.3 dB) are also wideband consistent (Fig. 3.16b). The gain peak at around 2.4–2.5 GHz is from the passive pre-gain. Following the linearity test profile of [7], two tones at [LO + 12 MHz, LO + 22 MHz] are applied, measuring an IIP3out-band of –6 dBm (Fig. 3.16c) at the maximum gain of 57 dB (there is 24-dB gain loss in Fig. 3.16c associated with the test buffer and used 1:8 transformer). This high IIP3 is due to the direct current-mode filtering at the mixer's output before signal amplification. The asymmetric IF response (Fig. 3.16d) shows 22-dB (43-dB) rejection at the adjacent (alternate) channel, and 36-dB IRR. Differing from the simulated IF frequency response that has three notches at the image band under an ideal LO, the measured notches are merged. Similar to [18], this discrepancy is likely due to the LO gain and phase mismatches, and the matching and variations of the RC-CR networks. The layout design is similar to [18] that uses dummy to balance the parasitic capacitances. The filtering rejection profile is around 80 dB/decade. The spurious free dynamic range (SFDR) is close to 60 dB according to [7, 21],

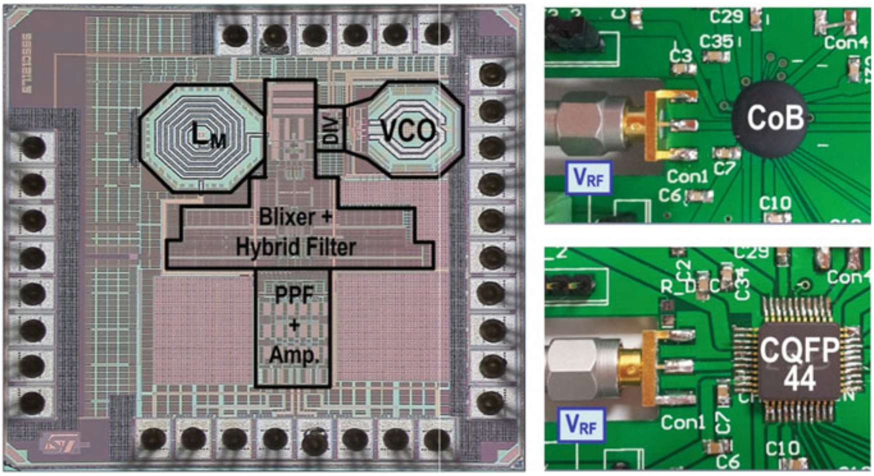

Fig. 3.15 Chip micrograph of the receiver. It was tested under CoB and CQFP44 packaging. No external component is entailed for input matching

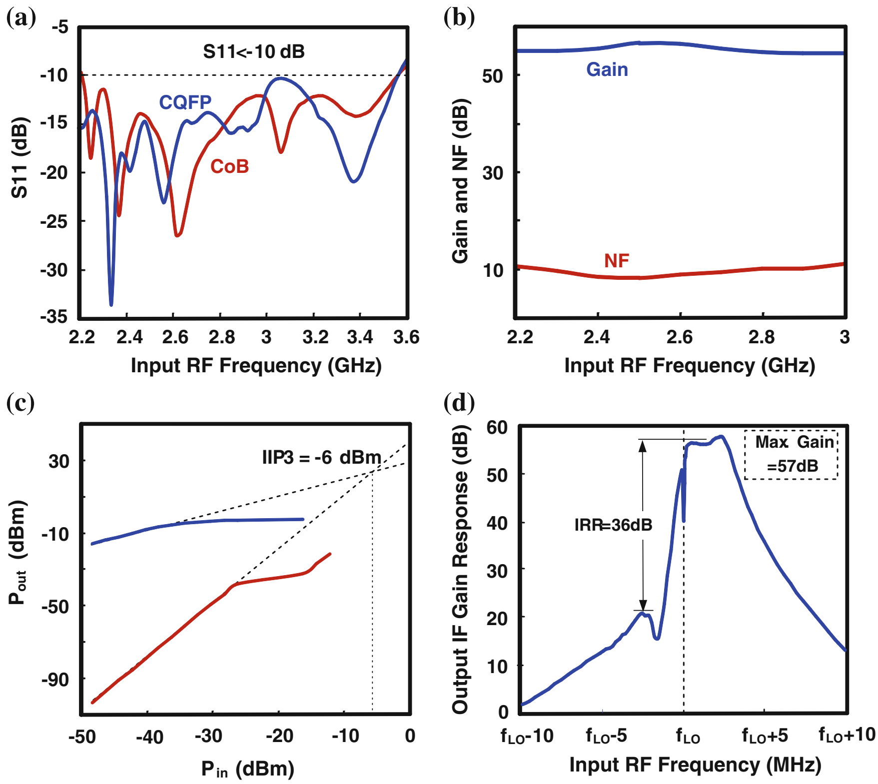

Fig. 3.16 Measured **a** S_{11}, **b** wide band gain and NF, **c** $IIP3_{out\text{-}band}$, and **d** low-IF filtering profile

$$\mathrm{SFDR} = \frac{2(P_{IIP3} + 174\mathrm{dBm} - \mathrm{NF} - 10\log\mathrm{BW})}{3} - \mathrm{SNR}_{min} \tag{3.5}$$

where SNR_{min} = 4 dB is the minimum signal-to-noise ratio required by the application, and BW = 2 MHz is the channel bandwidth.

The receiver was further tested at lower voltage supplies as summarized in Table 3.1. Only the NF degrades more noticeably, the IIP3, IRR and BB gain are almost secured. The better IIP3 for 0.6-V/1-V operation is mainly due to the narrower –3-dB bandwidth of the hybrid filter. For the 0.5-V/1-V operation, the degradation of $IIP3_{out\text{-}band}$ is likely due to the distortion generated by A_{GB}. Both cases draw very low power down to 0.8 mW, being comparable with other ULP designs such as [3, 4].

The LC-tank VCO was tested separately. Its power budget is related with its output swing and is a tradeoff with the phase noise, which measures –114 dBc/Hz at 3.5 MHz that has an enough margin to the specifications [22] (Fig. 3.17a). Porting it to the simulation results, it can be found that the corresponding VCO's output swing is 0.34 V_{pp} and the total LO-path power is 1.7 mW (VCO + dividers + BUFs). Such

Table 3.1 Key performances of the receiver at different supply voltages

Supply voltage (V)	0.6/1.2	0.6/1	0.5/1
Power (mW)	1.7	1.2	0.8
Gain (dB)	57	58	57.5
$IIP3_{out\text{-}band}$ (dBm)	–6	–4	–8
NF (dB)	8.5	11.3	12
IRR (dB)	36	38	35

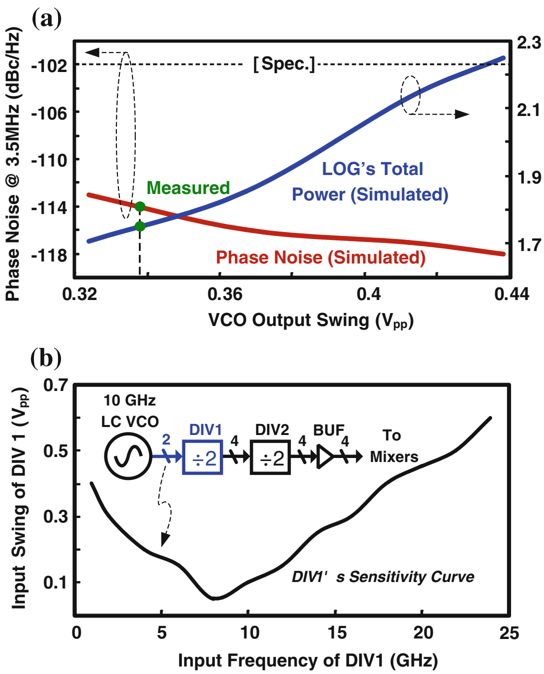

Fig. 3.17 **a** The measured phase noise has enough margin to the specifications. From simulations, it can be shown that it is a tradeoff with the power budget according to the VCO's output swing. **b** Simulated sensitivity curve of DIV1 showing its small input-voltage requirement at ~10 GHz

an output swing is adequate to lock DIV1 as shown in its simulated sensitivity curve (Fig. 3.17b).

The chip summary and performance benchmarks are given in Table 3.2, where [7, 8] are current-reuse architectures, [23] is a classical architecture with cascade of building blocks, and [5] is an ultra-low-voltage design. For this work, the results measured under a 10-GHz on-chip VCO are also included for completeness, but they are more sensitive to test uncertainties. The degraded NF and IRR are mainly due to the phase noise of the free-running VCO. In both cases, this work succeeds in advancing the IIP3out-band, power and area efficiencies, while achieving a wideband S_{11} with zero external components. Particularly, when comparing with the most recent work [5], this work achieves 8× less area and 15.5 dBm higher IIP3, together with stronger BB channel selectivity.

Table 3.2 Performance summary and benchmark with the state-of-the-art

	This work and ISSCC'13 [10]		JSSC'10 [7]	JSSC'10 [8]	JSSC'10 [23]	ISSCC'13 [5]
Application	ZigBee		ZigBee	GPS	ZigBee/Bluetooth	Energy harvesting
Architecture	Blixer + Hybrid-filter + Passive RC-CR PPF		LMV Cell + Complex filter	QLMV Cell + Complex filter	LNA + Mixer + Complex filter	LNA + Mixer + Frequency-translated IF filter
BB filtering	*1 Biquad + 4 complex poles*		3 complex poles	2 complex poles	3 complex poles	2 real poles
External I/P matching components	*zero*		1 inductor, 1 capacitor	1 passive balun	1 inductor, 1 capacitor	2 capacitors, 1 inductor
S_{11} ≤10 dB bandwidth (MHz)	*1300 (2.25–3.55 GHz)*		<300 (2.3–2.6 GHz)	100 (1.55–1.65 GHz)	>400 (<2.2–2.6 GHz)	>600 (<2–2.6 GHz)
Integrated VCO	No	Yes	Yes	Yes	No	Yes
Gain (dB)	57	55	75	42.5	67	83
Phase noise (dBc/Hz)	NA	–115 @ 3.5 MHz	–116 @ 3.5 MHz	–110 @ 1 MHz	NA	–112.8 @ 1 MHz
NF (dB)	8.5	9	9	6.5	16	6.1
$IIP3_{out\text{-}band}$ (dBm)	*–6*	*–6*	–12.5	N/A	–10.5	–21.5
IRR (dB)	36 (worst of 5 chips)	28	35	37	32	N/A
SFDR (dB)	*60.3*	*60*	55.5	N/A	53.6	51.6
LO-to-RF leak (dBm)	–61	–61	–60	–75	N/A	N/A

(continued)

Table 3.2 (continued)

	This work and ISSCC'13 [10]		JSSC'10 [7]	JSSC'10 [8]	JSSC'10 [23]	ISSCC'13 [5]
Power (mW)	*1.7*[1]	*2.7*	3.6	6.2 (inc. ADC)	20	1.6
Active area (mm^2)	*0.24*	*0.3*	0.35	1.5 (inc. ADC)	1.45	2.5
Supply voltage (V)	0.6/1.2		1.2	1	0.6	0.3
Technology	65 nm CMOS		90 nm CMOS	130 nm CMOS	65 nm CMOS	65 nm CMOS

[1]Breakdown: 1 mW: Blixer + Hybrid filter + BB circuitry, 0.7 mW: DIV1 + LO Buffers

3.5 Conclusions

A number of ULP circuits and optimization techniques have been applied to the design of a 2.4-GHz ZigBee receiver in 65-nm CMOS. The extensive-current-reuse RF-to-BB path is based on a Blixer + hybrid filter topology, which improves not only the power and area efficiencies, but also the out-band linearity due to more current-domain signal processing. Specifically, the Blixer features: (1) a low-Q input matching network realizing wideband S_{11} and robust passive pre-gain, (2) a balun-LNA with active-gain boosting and partial-noise-canceling improving the gain and NF, (3) I/Q-DBMs driven by a 4-phase 25 % LO inherently offering output balancing. For the hybrid filter, an IF-noise-shaping Biquad together with a complex-pole load synthesize 3rd-order channel selection and 1st-order image rejection. All of them render current-reuse topologies with great potential for developing ULP radios in advanced CMOS processes.

Appendix A: $S_{11} \leq 10$ dB Bandwidth Versus the Q Factor (Q_n) of the Input-Matching Network (Fig. 3.4a)

At the resonant frequency ω_0, L_M can resonate perfectly with C_{EQ} and R'_{in} for an exact 50 Ω. However, at a lower frequency $\omega = \omega_0 - \Delta\omega_L$ ($\Delta\omega_L > 0$), the imaginary part of $L_M//C_{EQ}$ is non-zero, making R'_{in} <50 Ω. This imaginary part is expressed as L_{eff} and derived as follows,

$$sL_M//sC_{EQ} = \frac{sL_M}{1 + s^2C_{EQ}L_M} \tag{A.1}$$

Let $\omega = \omega_0 - \Delta\omega_L$, where $\omega_0 = \frac{1}{\sqrt{L_MC_{EQ}}}$, and if substituted into (A.1), we will have,

$$\frac{j(\omega_0 - \Delta\omega_L)L_M}{1 - \frac{(\omega_0 - \Delta\omega_L)^2}{\omega_0^2}} \approx \frac{j(\omega_0 - \Delta\omega_L)L_M}{2\frac{\Delta\omega_L}{\omega_0}} = L_{eff} \tag{A.2}$$

where $\frac{\Delta\omega_L}{\omega_0} \ll 2$ is assumed. Here, the parallel of $|L_{eff}|||R_T$ is down-converted to $R'_{in} = 26\ \Omega$ by C_M and C_p, thus,

$$\frac{|L_{eff}|R_T}{|L_{eff}| + R_T}\left(\frac{C_M}{C_M + C_p}\right)^2 = 26\,\Omega \tag{A.3}$$

Substituting (A.2) into (A.3) and simplifying them, the normalized low-side frequency is obtained,

$$\frac{\Delta\omega_L}{\omega_0} = \frac{1}{1 + \frac{4aQ_n}{R_T - a}} \tag{A.4}$$

where $a = 26(\frac{C_M + C_p}{C_M})^2$. Then, the whole matching bandwidth is close to twice the value derived in (A.1) if the upper-side is included. (A.4) confirms that the S_{11} bandwidth can be significantly extended by designing a low Q_n.

Appendix B: NF of the Balun-LNA Versus the Gain ($G_{m,CS}$) of the CS Branch with A_{GB} (Fig. 3.4a)

The NF_{total} can be reduced by increasing $g_{m,AGB}$ with fixed $g_{m,CG}$ and $g_{m,CS}$, under matched input impedance. The noises from the I/Q-DBMs and their harmonic-folding terms, and the resistor R_p, are excluded for simplicity. Also, the conversion gain of the active mixers is assumed to be unity. Here $G_{m,CS}$ is upsized from $G_{m0,CS}$ to $G_{m,CS} = G_{m0,CS} + \Delta G_{m,CS}$, where G_{m0_CS} is the value for full noise cancellation of CG branch, i.e., $R_{in}G_{m0,CS} = 1$. The four major noise sources considered here are the thermal noises from R_S ($V^2_{n,Rs} = 4kTR_s$), M_1 ($I^2_{n,CG} = 4kT\gamma\, g_{m,CG}$), M_2 + A_{GB} ($I^2_{n,CS} = 4kT\gamma\, G_{m,CS}$) and $R_{L.}$, ($V^2_{n,L} = 4kTR_L$) where γ is the bias-dependent coefficient of the channel thermal noise. The noise contributed by the CG branch can be deduced as,

$$\begin{aligned} NF_{g_{m,CG}} &= \frac{V^2_{n,out,CG}}{V^2_{n,out,R_s}} = \frac{\frac{1}{4} I^2_{n,CG}\left[R_L - R_{in}\left(G_{m0,CS} + \Delta G_{m,CS}\right)R_L\right]^2}{4kTR_S A^2_{pre,amp} \times \frac{1}{4} \times \left[\frac{R_L}{R_{in}} + \left(G_{m0,CS} + \Delta G_{m,CS}\right)R_L\right]^2} \\ &= \frac{\gamma g_{m,CG}\left(R_{in}R_L\Delta G_{m,CS}\right)^2}{R_S A^2_{pre,amp}\left(\frac{2R_L}{R_{in}} + \Delta G_{m,CS}R_L\right)^2} \approx \frac{\gamma g_{m,CG} R^4_{in}\left(\Delta G_{m,CS}\right)^2}{4A^2_{pre,amp}R_S} \end{aligned} \tag{B.1}$$

where $\frac{2R_L}{R_{in}} \gg \Delta G_{m,CS}R_L$. If $\Delta G_{m,CS}$ is increased, the noise from M_1 also moves up. However, for the noise contribution of the CS branch, we can derive its TF to the output (V_{out}) as,

$$TF_{G_{m,CS}\to V_{out}} = \frac{R_L}{1+T}\left[\frac{T}{R_{in}\left(G_{m0,CS} + \Delta G_{m,CS}\right)} + 1\right] \approx R_L\left(1 - \Delta G_{m,CS}R_{in}\right)$$

where T is the loop gain $\gg$1. With it, the NF of $G_{m,CS}$ and NF of R_L can be derived,

$$\begin{aligned}\mathrm{NF}_{\mathrm{G_{m,CS}}} &= \frac{\mathrm{V}^2_{\mathrm{n,out,CS}}}{\mathrm{V}^2_{\mathrm{n,out,R_s}}} = \frac{4\mathrm{kT}\gamma\left(\mathrm{G_{m,CS}}+\Delta\mathrm{G_{m,CS}}\right)\left(\mathrm{TF}_{\mathrm{G_{m,CS}}\to\mathrm{V_{out}}}\right)^2}{4\mathrm{kTR_S}\mathrm{A}^2_{\mathrm{pre,amp}}\times\frac{1}{4}\times\left(\frac{2\mathrm{R_L}}{\mathrm{R_{in}}}+\Delta\mathrm{G_{m,CS}}\mathrm{R_L}\right)^2}\\ &\approx \frac{\gamma\mathrm{R}^2_{\mathrm{in}}\left(\mathrm{G_{m0,CS}}+\Delta\mathrm{G_{m,CS}}\right)\left(1-\Delta\mathrm{G_{m,CS}}\mathrm{R_{in}}\right)^2}{\mathrm{R_S}\mathrm{A}^2_{\mathrm{pre,amp}}} \approx \frac{\gamma\mathrm{R_{in}}\left(1-\Delta\mathrm{G_{m,cs}}\mathrm{R_{in}}\right)}{\mathrm{R_S}\mathrm{A}^2_{\mathrm{pre,amp}}}\end{aligned} \tag{B.2}$$

$$\begin{aligned}\mathrm{NF}_{\mathrm{R_L}} &= \frac{4\mathrm{kTR_L}}{4\mathrm{kTR_S}\mathrm{A}^2_{\mathrm{pre,amp}}\times\frac{1}{4}\times\left[\frac{\mathrm{R_L}}{\mathrm{R_{in}}}+\left(\mathrm{G_{m,CS}}+\Delta\mathrm{G_{m,CS}}\right)\mathrm{R_L}\right]^2}\\ &\approx \frac{4\mathrm{R_L}}{\mathrm{R_S}\mathrm{A}^2_{\mathrm{pre,amp}}}\frac{1}{\left(\frac{4\mathrm{R}^2_{\mathrm{L}}}{\mathrm{R}^2_{\mathrm{in}}}+\frac{2\Delta\mathrm{G_{m,CS}}\mathrm{R}^2_{\mathrm{L}}}{\mathrm{R_{in}}}\right)} \approx \frac{\mathrm{R}^2_{\mathrm{in}}}{\mathrm{R_L}\mathrm{R_S}\mathrm{A}^2_{\mathrm{pre,amp}}}\left(1-\frac{\Delta\mathrm{G_{m,CS}}\mathrm{R_{in}}}{2}\right)\end{aligned} \tag{B.3}$$

As expected, when $\Delta\mathrm{G_{m,CS}}$ increases the noise contribution of $\mathrm{G_{m,CS}}$ and $\mathrm{R_L}$ can be reduced. The optimal $\Delta\mathrm{G_{m,CS}}$ can be derived from $\frac{\partial\mathrm{NF_{total}}}{\partial\Delta\mathrm{G_{m,CS}}}=0$, where $NF_{\mathrm{total}} = 1+\mathrm{NF}_{\mathrm{G_{m,CG}}}+\mathrm{NF}_{\mathrm{G_{m,CS}}}+2\mathrm{NF}_{\mathrm{R_L}}$.

References

1. P. Choi, H. Park, S. Kim et al., An experimental coin-sized radio for extremely low-power WPAN(IEEE 802.15.4) application at 2.4-GHz. IEEE J. Solid-State Circ. **38**, 2258–2268 (2003)
2. C.-H. Li, Y.-L. Liu, C.-N. Kuo, A 0.6-V 0.33-mW 5.5-GHz receiver front-end using resonator coupling technique. IEEE Trans. Microw. Theory Tech. **59**(6), 1629–1638 (2011)
3. B.W. Cook, A. Berny, A. Molnar, S. Lanzisera, K. Pister, Low-power, 2.4-GHz transceiver with passive RX front-end and 400-mV supply. IEEE J. Solid-State Circ. **41**, 2767–2775 (2006)
4. A.C. Herberg, T.W. Brown, T.S. Fiez, K. Mayaram, A 250-mV, 352-µW GPS receiver RF front-end in 130-nm CMOS. IEEE J. Solid-State Circ. **46**, 938–949 (2011)
5. F. Zhang, K. Wang, J. Koo, Y. Miyahara, B. Otis, A 1.6 mW 300 mV supply 2.4 GHz receiver with –94 dBm sensitivity for energy-harvesting applications. ISSCC Dig. Tech. Papers, pp. 456–457, Feb 2013
6. S. Blaakmeer, E. Klumperink, D. Leenaerts, B. Nauta, The blixer, a wideband balun-LNA-I/Q-Mixer topology. IEEE J. Solid-State Circ. **43**, 2706–2715 (2008)
7. M. Tedeschi, A. Liscidini, R. Castello, Low-power quadrature receivers for ZigBee (IEEE 802.15.4) applications. IEEE J. Solid-State Circ. **45**, 1710–1719 (2010)
8. K.-W. Cheng, K. Natarajan, D. Allstot, A Current Reuse Quadrature GPS Receiver in 0.13 µm CMOS. IEEE J. of Solid-State Circ. **45**, 510–523 (2010)
9. D. Ghosh, R. Gharpurey, A power-efficient receiver architecture employing bias-current-shared RF and baseband with merged supply voltage domains and 1/f noise reduction. IEEE J. Solid-State Circ. **47**, 381–391 (2012)

10. Z. Lin, P.-I. Mak, R. P. Martins, A 1.7 mW 0.22 mm^2 2.4 GHz ZigBee RX exploiting a current-reuse blixer + hybrid filter topology in 65 nm CMOS, ISSCC Dig. Tech. Papers, pp. 448–449, Feb. 2013
11. S. Blaakmeer, E. Klumperink, D. Leenaerts, B. Nauta, Wideband balun-LNA with simultaneous output balancing, noise-canceling and distortion-canceling. IEEE J. Solid-State Circ. **43**, 1341–1350 (2008)
12. P.-I. Mak, R.P. Martins, A 0.46-mm^2 4-dB NF unified receiver front-end for full-band mobile TV in 65-nm CMOS. IEEE J. Solid-State Circ. **46**, 1970–1984 (2011)
13. F. Bruccoleri, E. Klumperink, B. Nauta, Wide-band CMOS low-noise amplifier exploiting thermal noise canceling. IEEE J. Solid-State Circ. **39**, 275–282 (2004)
14. A. Pirola, A. Liscidini, R. Castello, Current-mode, WCDMA channel filter with in-band noise shaping. IEEE J. Solid-State Circ. **45**, 1770–1780 (2010)
15. C.L. Ler, A.K. A'ain, A.V. Kordesh, CMOS source degenerated differential active inductor. IET Electr. Lett. **44**, 196–197 (2008)
16. Y. Chen, P.-I. Mak, L. Zhang, Y. Wang, A 0.07 mm^2, 2 mW, 75 MHz-IF, 4th-Order BPF using a source-follower-based resonator in 90 nm CMOS. IET Electr. Lett. **48**, 552–554 (2012)
17. J. Kaykovuori, K. Stadius, J. Ryynanen, Analysis and design of passive polyphase filters. IEEE Trans. Circ. Syst. I, Reg. Pap **55**, 3023–3037 (2008)
18. F. Behbahani, Y. Kishigami, J. Leete, A.A. Abidi, CMOS mixers and polyphase filters for large image rejection. IEEE J. Solid-State Circ. **36**, 873–887 (2001)
19. B. Razavi, K.F. Lee, R.H. Yan, Design of high-speed, low-power frequency dividers and phase-locked loops in deep submicron CMOS. IEEE J. Solid-State Circ. **30**, 101–109 (1995)
20. M. Camus, B. Butaye, L. Garcia, M. Sie, B. Pellat, T. Parra, A 5.4 mW/0.007 mm^2 2.4 GHz front-end receiver in 90 nm CMOS for IEEE 802.15.4 WPAN standard. IEEE J. Solid-State Circ. **43**, 1372–1383 (2008)
21. B. Razavi, *RF Microelectronics*, 2nd edn. (Prentice-Hall, New Jersey, 2011)
22. A. Liscidini, M. Tedeschi, R. Castello, A 2.4 GHz 3.6 mW 0.35 mm^2 quadrature front-end RX for ZigBee and WPAN applications. ISSCC Digest of Technical Papers, pp. 370–371, Feb. 2008
23. A. Balankutty, S.A. Yu, Y. Feng, P. Kinget, A 0.6 V Zero-IF/Low-IF receiver with integrated fractional-N synthesizer for 2.4 GHz ISM-band applications. IEEE J. Solid-State Circ. **45**, 538–553 (2010)

Chapter 4
Analysis and Modeling of a Gain-Boosted N-Path Switched-Capacitor Bandpass Filter

4.1 Introduction

The demand of highly-integrated multi-band transceivers has driven the development of blocker-tolerant software-defined radios that can avoid the cost (and loss) of the baluns and SAW filters [1–3]. The passive-mixer-first receivers [1, 2] achieve a high out-of-band (OB) linearity (IIP3 = +25 dBm) by eliminating the forefront low-noise amplifier (LNA). However, in the absence of RF gain, a considerable amount of power is entailed for the local oscillator (LO) to drive up the mixers that must be essentially large (i.e., small on-resistance, R_{sw}) for an affordable noise figure (NF <5 dB). The noise-cancelling receiver in [3] breaks such a NF-linearity tradeoff, by noise-cancelling the main path via a high-gain auxiliary path, resulting in better NF (1.9 dB). However, due to the wideband nature of all RF nodes, the passive mixers of the auxiliary path should still be large enough for a small R_{sw} (10 Ω) such that the linearity is upheld (IIP3 = +13.5 dBm). Indeed, it would be more effective to perform filtering at the antenna port.

An N-path switched-capacitor (SC) branch applied at the antenna port [4, 5] corresponds to direct filtering that enhances OB linearity, although the sharpness and ultimate rejection are limited by the capacitor size and non-zero R_{sw} that are tight tradeoffs with the area and LO power, respectively. Repeatedly adopting such filters at different RF nodes can raise the filtering order, but at the expense of power and area [5, 6].

Active-feedback frequency translation loop [7] is another technique to enhance the area efficiency (0.06 mm^2), narrowing RF bandwidth via signal cancellation, instead of increasing any RC time-constant. Still, the add-on circuitry (amplifiers and mixers) penalizes the power (62 mW) and NF (>7 dB). In [8], at the expense of more LO power and noise, the output voltages can be extracted from the capacitors via another set of switches, avoiding the effects of R_{sw} on the ultimate rejection, but the problem of area remains unsolved.

Z. Lin et al., *Ultra-Low-Power and Ultra-Low-Cost Short-Range Wireless Receivers in Nanoscale CMOS*, Analog Circuits and Signal Processing,
DOI 10.1007/978-3-319-21524-2_4

Recently, an ultra-low-power multi-band ZigBee receiver [9] was demonstrated, which features a novel gain-boosted N-path passive mixer to optimize the NF and OB linearity with power. The underlying principle is generalized here, leading to a *gain-boosted N-path SC bandpass filter (GB-BPF)* with a number of attractive features: (1) tunability of center frequency, passband gain and bandwidth without affecting the input-impedance matching; (2) lower LO power as the pitfall of big R_{sw} can be leveraged by other design freedoms, and (3) much smaller capacitors for a given bandwidth thanks to the gain-boosting effects.

This chapter is organized as follows: Sect. 4.2 introduces the proposed GB-BPF and describes its features via an ideal RLC model first. Linear periodically time-variant (LPTV) analysis is then followed to derive and examine the models of those R, L and C. The analysis of harmonic selectivity, harmonic folding and noise are detailed in Sect. 4.3, where an equivalent circuit model for studying the influence of non-idealities is included. In Sect. 4.4, a simulation design example is given. Finally, the conclusions are drawn in Sect. 4.5.

4.2 GB-BPF Using an Ideal RLC Model

The proposed GB-BPF is depicted in Fig. 4.1a. It features a transconductance amplifier (G_m) in the forward path, and an N-path SC branch driven by an N-phase non-overlapped LO in the feedback path. When one of the switches is ON, an

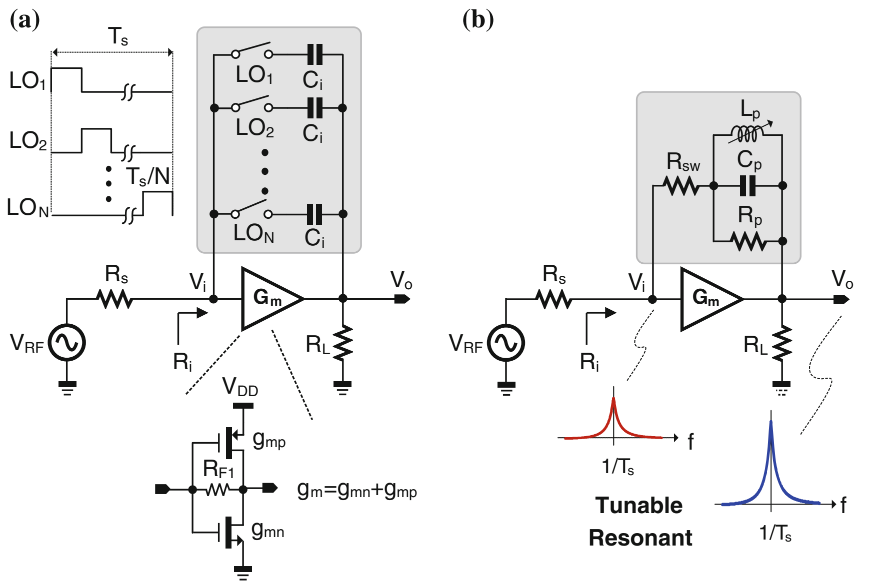

Fig. 4.1 **a** Proposed gain-boosted N-path SC bandpass filter (GB-BPF) and **b** Its equivalent RLC circuit with the LC resonant tunable by the LO. R_{sw} is the mixer switch's on-resistance

in-phase RF voltage V_{RF} will appear on the top plate of capacitor C_i, and induces an amplified anti-phase voltage into its bottom plate. When the switch is OFF, the amplified version of V_{RF} will be stored in C_i. There are three observations: (1) similar to the well-known capacitor-multiplying technique (i.e., Miller effect) in amplifiers, the effective capacitance of C_i at the input node V_i will be boosted by the loop gain created by G_m, while it is still C_i at the output node V_o. This feature, to be described later, reduces the required C_i when comparing it with the traditional passive N-path filter. (2) For the in-band signal, the voltages sampled at all C_i are in-phase summed at V_i and V_o after a complete LO switching period (T_s), while the OB blockers are cancelled to each other, resulting in double filtering at two RF nodes in one step. (3) As the switches are located in the feedback path, their effects to the OB rejection should be reduced when comparing it with the passive N-path filter.

For simplicity, G_m is assumed as an inverter amplifier with an effective transconductance of g_m. It is self-biased by the resistor R_{F1} and has a finite output resistance explicitly modeled as R_L. The parasitic effects will be discussed in Sect. 4.3.3. With both passband gain and resistive input impedance, the GB-BPF can be directly connected to the antenna port for matching with the source impedance R_S. Around the switching frequency (ω_s), the N-path SC branch is modeled as an R_p-L_p-C_p parallel network [10] in series with R_{sw}, where L_p is a function of ω_s and will resonate with C_p at ω_s (Fig. 4.1b). The expressions of R_p, L_p and C_p will be derived in Sect. 4.2.3. Here, the filtering behavior and –3-dB bandwidth at V_i and V_o will be analyzed.

4.2.1 *RF Filtering at V_i and V_o*

With V_{RF} centered at frequency $f_{RF} = f_s = \omega_s/2\pi$, L_P and C_p are resonated out, yielding an input resistance $R_i|_{@f_s}$ that can be sized to match R_S for the in-band signal,

$$R_i|_{@f_s} = \frac{(R_p + R_{sw})//R_{F1} + R_L}{1 + g_m R_L} = R_S. \tag{4.1}$$

For the OB blockers located at $f_{RF} = f_s \pm \Delta f_s$, either L_p or C_p will become a short circuit when Δf_s is large enough,

$$R_i|_{@f_s \pm \Delta f_s} = \frac{(R_{sw}//R_{F1}) + R_L}{1 + g_m R_L} \approx \frac{R_{sw} + R_L}{1 + g_m R_L} \approx \frac{R_{sw}}{g_m R_L} + \frac{1}{g_m}, \tag{4.2}$$

where $R_{F1} >> R_{sw}$ and $g_m R_L >> 1$ are applied and reasonable to simplify (4.2). To achieve stronger rejection of OB blockers at V_i, a small $R_i|_{@f_s \pm \Delta f_s}$ is expected.

Unlike the traditional passive N-path filter where the OB rejection is limited by R_{sw} [10, 11], this work can leverage it with three degrees of freedom: g_m, R_L and R_{sw}. As a GB-BPF at the forefront of a receiver, a large g_m is important to lower the NF of itself and its subsequent circuits. As an example, with g_m = 100 mS, the product of g_mR_L can reach 8 V/V with R_L = 80 Ω. Thus, if R_{sw} = 20 Ω is assumed, we obtain $R_i|_{@f_s \pm \Delta f_s} \approx 12.5$ Ω, which is only 62.5 % of R_{sw}. If g_m is doubled (implying more power) while maintaining the same g_mR_L, then $R_i|_{@f_s \pm \Delta f_s}$ will be reduced to 7.5 Ω. Another way to trade the OB rejection with power is to adopt a multi-stage amplifier as G_m, which can potentially decouple the limited g_mR_L-product of a single-stage amplifier in nanoscale CMOS.

OB filtering not only happens at V_i, but also V_o. Hence, with one set of switches, double filtering is achieved in this work, leading to higher power and area efficiency than the traditional cascade design (i.e., two SC branches separately applied for V_i and V_o) as described in [5]. Likewise, the gain at V_o at the resonance can be found as,

$$A_{vo}|_{@f_s} = \frac{V_o}{V_{RF}} = \frac{R_L(1 - g_mR_T)}{2R_S(1 + g_mR_L)} \approx \frac{R_L(1 - g_mR_T)}{2R_Sg_mR_L}, \quad (4.3)$$

where $R_T = R_{F1}//(R_p + R_{sw})$ and $g_mR_L >> 1$ are applied. In terms of stability, (4.3) should be negative or zero, i.e., $g_mR_T \geq 1$. Similarly, the gain at V_o at $f_s \pm \Delta f_s$ is derived when L_p or C_p is considered as a short circuit,

$$\frac{V_o}{V_{RF}}|_{@f_s \pm \Delta f_s} = \frac{1 - g_mR_{sw}}{1 + g_mR_S + \frac{R_S}{R_L} + \frac{R_{sw}}{R_L}}. \quad (4.4)$$

Interestingly, if $g_mR_{sw} = 1$, the OB filtering is infinite. This is possible because the feedback network is frequency selective, implying that the in-band signal and OB blockers can see different feedback factors. This fact differentiates this circuit from the traditional resistive-feedback wideband LNAs such as [12] that cannot help to reject the OB blockers.

To exemplify, the circuit of Fig. 4.1a is simulated for N = 4, using PSS and PAC analyses in Spectre RF. The parameters are: R_{sw} = 20 Ω, R_L = 80 Ω, R_S = 50 Ω, C_i = 5 pF and f_s = 1 GHz. As expected, higher selectivity at V_i (Fig. 4.2a) and V_o (Fig. 4.2b) can be observed when g_m (100–800 mS) and R_{F1} (500–8 kΩ) are concurrently raised, while preserving the in-band S_{11} ≤ 20 dB (Fig. 4.2c). Alternatively, when R_{sw} goes up from 10 to 50 Ω, with other parameters unchanged, it can be observed that the influence of R_{sw} to the OB rejection is relaxed at both V_i (Fig. 4.3a) and V_o (Fig. 4.3b), being well-consistent with (4.2) and (4.4). When R_{sw} = 10 Ω, a much stronger OB rejection is due to $g_mR_{sw} = 1$ in (4.4).

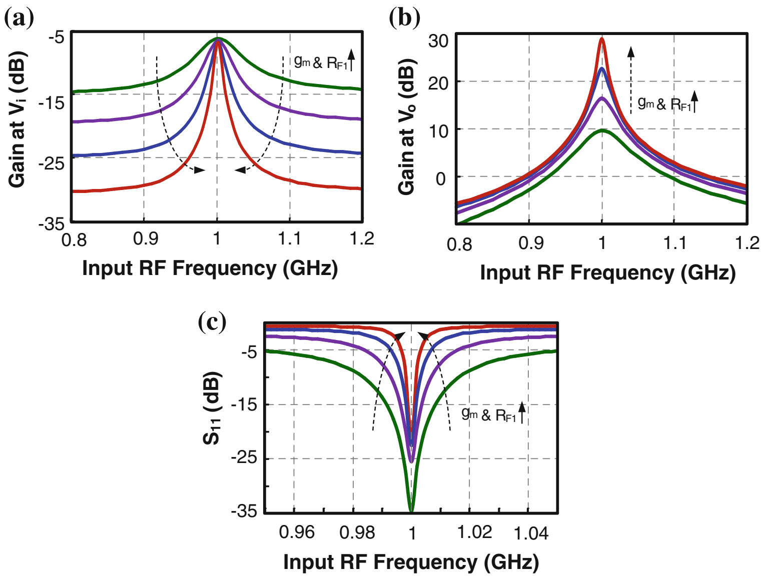

Fig. 4.2 Simulated **a** gain at V_i, **b** gain at V_o and **c** S_{11}, showing how g_m and R_{F1} tune the in-band gain and bandwidth while keeping the in-band S_{11} well below –20 dB

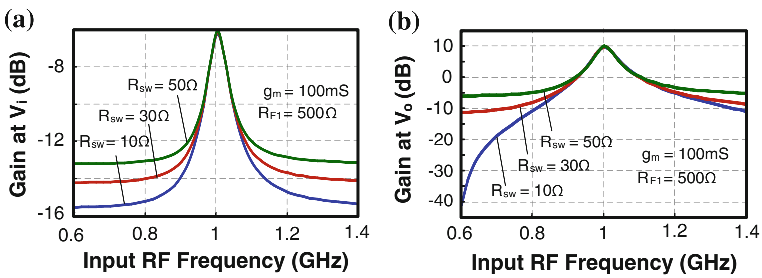

Fig. 4.3 Simulated **a** gain at V_i, **b** gain at V_o under R_{sw} = 10, 30 and 50 Ω

4.2.2 –3-dB Bandwidth at V_i and V_o

At frequency $f_{RF} = f_s$, we can write $\frac{V_i}{V_{RF}}|_{@f_s} = 1/2$ when $R_i = R_s$. The –3-dB bandwidth is calculated by considering that the L_pC_p tank only helps shifting the centre frequency of the circuit from DC to f_s, keeping the same bandwidth as it is without L_p. If R_{sw} is neglected and the Miller approximation is applied, the –3-dB passband bandwidth $(2\Delta f_{i3dB})$ at V_i can be derived,

$$2\Delta f_{i3dB} = \frac{1}{\pi R_s C_i}; \quad C_i \approx (1 + A_{vi})C_p, \tag{4.5}$$

where

$$A_{vi} = \frac{V_o}{V_i} = \frac{R_L(1 - g_m R_T)}{R_S(1 + g_m R_L)}.$$

Obviously, C_p is boosted by a gain factor A_{vi}, which should be 15–20 dB in practice. Thus, a large A_{vi} can be used to improve the area efficiency, consistent with the desire of higher selectivity OB filtering, as shown in Fig. 4.2a, b. Passive N-path filters [10] do not exhibit this advantageous property and the derived C_p is also different. In Sect. 4.3.3, an intuitive equivalent circuit model of Fig. 4.1a will be given for a more complete comparison with the traditional architecture.

At V_o, the –3-dB passband bandwidth $(2\Delta f_{o3dB})$ can be derived next, assuming R_{sw} = 0 for simplicity. The gain from V_{RF} to V_o at frequency $f_s - \Delta f_{o3dB}$ is given by,

$$A_{vo}|_{@f_s - \Delta f_{o3dB}} = \frac{V_o}{V_{RF}} = \frac{R_L(1 - g_m Z_T)}{2R_S(1 + g_m R_L)}, \tag{4.6}$$

where

$$Z_T = jL_{eff}//R_{F1}//R_p \text{ and } L_{eff} \approx \frac{\omega_s - \Delta\omega_{o3dB}}{2\frac{\Delta\omega_{o3dB}}{\omega_s}} L_p. \tag{4.7}$$

From the definition of –3-dB passband bandwidth,

$$\frac{|A_{vo|_{@f_s}}|}{|A_{vo|@f_s - \Delta f_{o3dB}}|} = \frac{|1 - g_m R_{FP}|}{|1 - g_m Z_T|} = \sqrt{2}, \tag{4.8}$$

where $A_{vo|_{@f_s}}$ is the voltage gain at the resonant frequency, while R_{FP} = $R_{F1}//R_P$. Substituting (4.6), (4.7) into (4.8), (4.9) is obtained after simplification,

$$L_{eff} = \frac{\sqrt{g_m^2 R_{FP}^2 - 2g_m R_{FP} - 1} \times R_{FP}}{g_m R_{FP} - 1} \approx R_{FP}. \tag{4.9}$$

Substituting (4.9) into (4.7), $\Delta\omega_{o3dB}$ becomes,

$$\Delta\omega_{o3dB} = \frac{\omega_s^2}{2\frac{L_{eff}}{L_p} + \omega_s} \approx \frac{\omega_s^2}{2\frac{L_{eff}}{L_p}} = \frac{1}{2L_{eff}C_p} = \frac{1}{2R_{FP}C_p}. \tag{4.10}$$

Finally, $2\Delta f_{o3dB}$ at V_o can be approximated as,

$$2\Delta f_{o3dB}|_{@V_o} \approx \frac{1}{\pi\, R_{FP}C_p}.$$

4.2.3 Derivation of the R_p-L_p-C_p Model Using the LPTV Analysis

The GB-BPF (Fig. 4.1a) can be classified as a LPTV system. This section derives the R_p-L_p-C_p model of the gain-boosted N-path SC branch. Similar to [13, 14], the voltage on the SC branch is defined as $V_{Ci}(j\omega)$,

$$V_{Ci}(j\omega) = \sum_{n=-\infty}^{\infty} H_{n,RF}(j\omega)V_{RF}(j(\omega - n\omega_s)). \tag{4.11}$$

Here n indicates a harmonic number of f_s, and $H_{n,RF}(j\omega)$ is the nth harmonic transfer function associated with the frequency nf_s. With $V_{ci}(j\omega)$, the voltages at $V_i(j\omega)$ and $V_o(j\omega)$ can be related to the input RF signal $V_{RF}(j\omega)$,

$$\begin{aligned} V_i(j\omega) = {} & \underbrace{V_{RF}(j\omega)\frac{1}{\gamma}\left(\beta\frac{R_L}{R_S} + H_{0,RF}(j\omega)\right)}_{V_{i,de}} \\ & + \underbrace{\frac{1}{\gamma}\sum_{n=-\infty,n\neq 0}^{\infty} H_{n,RF}(j\omega)V_{RF}(j(\omega - n\omega_s))}_{V_{i,un}} \end{aligned} \tag{4.12}$$

and

$$\begin{aligned} V_o(j\omega) = {} & \underbrace{\frac{R_{F1}R_L\left(1 - g_mR_{sw} + \frac{R_{sw}}{R_{F1}}\right)}{R_{F1}R_{SW} + (R_{F1} + R_{sw})(R_s + g_mR_LR_s + R_L)}}_{V_{o,de}} \\ & \times \underbrace{\left[V_{RF}(j\omega) - \frac{H_{0,RF}(j\omega)V_{RF}(j\omega)(1 + g_mR_s)}{\left(1 - g_mR_{sw} + \frac{R_{sw}}{R_{F1}}\right)}\right]}_{V_{o,de}} \\ & - \underbrace{\frac{R_{F1}R_L(1 + g_mR_s)}{R_{F1}R_{SW} + (R_{F1} + R_{sw})(R_s + g_mR_LR_s + R_L)}}_{V_{o,un}} \\ & \times \underbrace{\sum_{n=-\infty,n\neq 0}^{\infty} H_{n,RF}(j\omega)V_{RF}(j(\omega - n\omega_s)).}_{V_{o,un}} \end{aligned} \tag{4.13}$$

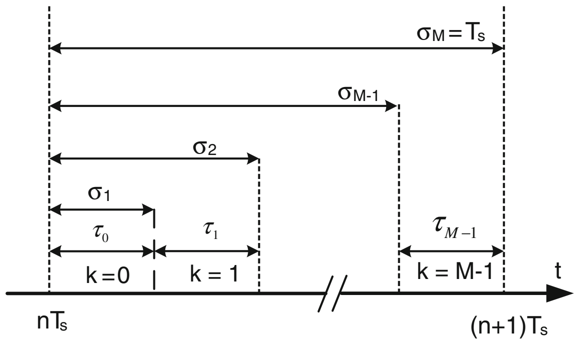

Fig. 4.4 Time intervals for the state-space analysis

where

$$\alpha = 1 - g_m R_{sw} + \frac{R_{sw}}{R_{F1}}, \quad \beta = 1 + \frac{R_{sw}}{R_L} + \frac{R_{sw}}{R_{F1}}$$
$$\text{and} \quad \gamma = \alpha + \beta\left(\frac{R_L}{R_S} + g_m R_L\right).$$

Equations (4.12) and (4.13) can be divided into two parts: (1) the desired frequency selectivity (i.e., $V_{i,de}$ and $V_{o,de)}$ that provides filtering without frequency translation at the desired input frequency, and (2) the undesired harmonic folding components that might fall in the desired band (i.e., $V_{i,un}$ and $V_{o,un}$).

To find $H_{n,RF}(j\omega)$, a state-space analysis is conducted. The timing diagram for the analysis is shown in Fig. 4.4. The timing interval $nT_s < t < nT_s + T_s$ is divided into M portions (M is the number of the states) and each portion, identified by k, can be represented as $nT_s + \sigma_k < t < nT_s + \sigma_{k+1}$, $k = 0,\ldots, M-1$ and $\sigma_0 = 0$. During each interval there is no change in the state of the switches, and the network can be considered as a LTI system. During the k interval, linear analysis applied to Fig. 4.1a reveals that the switch on interval k has the following state-space description,

$$\begin{cases} \frac{C_i d\upsilon_{Ci}(t)}{dt} + \frac{\upsilon_i(t) - \upsilon_o(t)}{R_{F1}} = \frac{\upsilon_o(t)}{R_L} + g_m \upsilon_i(t) \\ \frac{\upsilon_{RF}(t) - \upsilon_i(t)}{R_S} = \frac{\upsilon_o(t)}{R_L} + g_m \upsilon_i(t) \\ \upsilon_i(t) = \upsilon_{Ci}(t) + \upsilon_o(t) + R_{sw} \frac{C_i d\upsilon_{Ci}(t)}{dt}. \end{cases} \tag{4.14}$$

From (4.14), we obtain

$$\frac{d\upsilon_{Ci}(t)}{dt} = \frac{\upsilon_{RF}(t)}{C_i R_1} - \frac{\upsilon_{Ci}(t)}{C_i R_2}, \tag{4.15}$$

where

$$R_1 = \frac{1 + \frac{R_{sw}}{R_{F1}} + \frac{R_{sw}+R_S}{R_L} + \frac{R_{sw}R_S}{R_{F1}R_L} + g_m R_S + \frac{g_m R_{sw} R_S}{R_{F1}}}{\frac{1}{R_L} + g_m}$$

$$R_2 = \frac{1 + \frac{R_{sw}}{R_{F1}} + \frac{R_{sw}+R_S}{R_L} + \frac{R_{sw}R_S}{R_{F1}R_L} + g_m R_S + \frac{g_m R_{sw} R_S}{R_{F1}}}{\frac{1}{R_{F1}} + \frac{1}{R_L} + \frac{R_S}{R_{F1}R_L} + \frac{g_m R_S}{R_{F1}}}.$$

By applying the state-space analysis for the circuit in Fig. 4.1a, the harmonic transfer function can be derived as,

$$\begin{aligned} H_{n,RF}(j\omega) &= \sum_{m=0}^{N-1} e^{-jn\omega_s\sigma_m} H_{n,m}(j\omega) \\ H_{n,m}(j\omega) &= \frac{\omega_{rc,B}}{\omega_{rc,A} + j\omega} \times \frac{1 - e^{-jn\omega_s\tau_m}}{j2\pi n} \\ &\quad + \frac{1 - e^{j(\omega - n\omega_s)(T_S - \tau_m) - jn\omega_s\tau_m}}{\omega_{rc,A} + j\omega} G(j\omega) f_s \end{aligned} \tag{4.16}$$

where

$$G(j\omega) = \frac{e^{j(\omega - n\omega_s)\tau_m} - e^{-\omega_{rc,A}\tau_m}}{e^{j2\pi(\omega - n\omega_s)/\omega_s} - e^{-\omega_{rc,A}\tau_m}} \times \frac{1}{\frac{\omega_{rc,A}}{\omega_{rc,B}} + \frac{j(\omega - n\omega_s)}{\omega_{rc,B}}},$$

$\omega_{rc,A} = 1/R_2C_i$ and $\omega_{rc,B} = 1/R_1C_i$. The above $H_{n,RF}(j\omega)$ is undefined for $n = 0$, and, for this value, (4.16) will be defined by the limit when n tends to zero, implying that,

$$H_{0,RF}(j\omega) = \frac{\omega_{rc,B}}{\omega_{rc,A} + j\omega} + \frac{1 - e^{j\omega(T_S - \tau_m)}}{\omega_{rc,A} + j\omega} G(j\omega) f_s N \tag{4.17}$$

where

$$G(j\omega) = \frac{e^{j\omega\tau_m} - e^{-\omega_{rc,A}\tau_m}}{e^{j2\pi\omega/\omega_s} - e^{-\omega_{rc,A}\tau_m}} \times \frac{1}{\frac{\omega_{rc,A}}{\omega_{rc,B}} + \frac{j\omega}{\omega_{rc,B}}}.$$

To find R_p, $H_{0,RF}(j\omega)$ is calculated in Appendix A at $\omega = nf_s$ with $\omega_s \gg \omega_{rc,A}, \omega_{rc,B}$, yielding,

$$H_{0,RF}(jn\omega_s) = \frac{2N(1-\cos 2\pi nD)}{4D(n\pi)^2} \times \frac{\omega_{rc,B}}{\omega_{rc,A}}, \tag{4.18}$$

where D = 1/N is the duty cycle of the LO. Furthermore, (4.18) is similar to (4.15) in [10], except for the added term $\omega_{rc,B}/\omega_{rc,A}$.

If n = 1, N = 4 and D = 0.25, for a 25 %-duty-cycle 4-path LO, (4.18) becomes,

$$H_{0,RF}(j\omega_s) = \frac{8}{\pi^2} \times \frac{R_2}{R_1}. \tag{4.19}$$

Assuming that L_p is resonant with C_p at ω_s, it implies,

$$\begin{cases} \dfrac{V_i - H_{0,RF}(j\omega_s)V_{RF} - V_o}{R_{sw}} = \dfrac{H_{0,RF}(j\omega_s)V_{RF}}{R_p} \\ \dfrac{V_i - H_{0,RF}(j\omega_s)V_{RF} - V_o}{R_{sw}} + \dfrac{V_i - V_o}{R_{F1}} = g_m V_i + \dfrac{V_o}{R_L} \\ \dfrac{V_{RF} - V_i}{R_s} = g_m V_i + \dfrac{V_o}{R_L} \end{cases} \tag{4.20}$$

Solving (4.20), it leads to the desired R_P,

$$R_p = \frac{\eta H_{0,RF} R_{sw}}{\left(\frac{R_L R_{FL}}{R_s} + \frac{H_{0,RF}}{R_{sw}}\right)\left(1 + \frac{R_L}{R_s} + g_m R_L\right) - (H_{0,RF} + \frac{R_L}{R_s})\eta},$$

where

$$R_{FL} = \frac{1}{R_L} + \frac{1}{R_{F1}} + \frac{1}{R_{sw}}$$

$$\eta = \frac{1}{R_{sw}} + \frac{1}{R_{F1}} - g_m + \frac{R_L R_{FL}}{R_s} + g_m R_L R_{FL}.$$

Finally, placing the pole around ω_s in (4.17), with a value equal to the poles of the transfer function from V_{RF} to V_{Cp} of Fig. 4.1b, it will lead to the expressions of C_p and L_p (Appendix B),

$$C_p = \frac{\gamma_1 + R_p}{2D\omega_{rc,A}\gamma_1 R_p} \tag{4.21}$$

$$L_p = \frac{\gamma_1 R_p}{D\omega_{rc,A}(\gamma_1 + R_p) - (D^2\omega_{rc,A}^2 - \omega_s^2)\gamma_1 R_p C_p} \tag{4.22}$$

where

$$\alpha_1 = \frac{1}{R_{sw}} + \frac{1}{R_{F1}} - g_m, \gamma_1 = -\frac{\alpha_1 \beta_1 R_{sw}^2}{\beta_1 - 1 - \alpha_1 \beta_1 R_{sw}},$$

$$\beta_1 = \frac{\frac{1}{R_L} + \frac{1}{R_{F1}} + \frac{1}{R_{sw}} + \frac{\alpha_1 R_s}{R_L(1 + g_m R_s)}}{\frac{1}{R_L} + g_m}.$$

From (4.21) to (4.22), C_p is irrelevant to the LO frequency ω_s, while L_p is tunable with ω_s. Moreover, the term $D\omega_{rc,A}(\gamma_1 + R_p) - \left(D^2\omega_{rc,A}^2 - \omega_s^2\right)\gamma_1 R_p C_p$ in the denominator of (4.22) renders that the $L_p//C_p$ resonant frequency shifts slightly away from the center frequency ω_s. For $\omega_s \gg \omega_{rc,A}$, $L_p \approx \frac{R_p}{\omega_s^2 C_p}$ is obtained and will resonate out with C_p at ω_s. Then, the frequency responses can be plotted using the derived expressions, and compared with the simulated curves of Fig. 4.5a, b; showing a good fitting around ω_s, and confirming the previous analysis. The small discrepancy arises from the approximation that L_p will resonate out with C_p at ω_s when deriving R_p in (4.20). This effect is smaller at V_i than at V_o, due to the gain of the GB-BPF.

4.3 Harmonic Selectivity, Harmonic Folding and Noise

4.3.1 Harmonic Selectivity and Harmonic Folding

Using the harmonic selectivity function $H_{0,RF}(j\omega)$ from (4.18), the relative harmonic selectivity is calculated by combining (4.13) and (4.18) for V_i and V_o. For example, when N = 4,

$$\frac{V_0(\omega_s)}{V_0(n\omega_s)} = \frac{1 - \frac{8}{\pi^2} \times \frac{R_2}{R_1} \times \text{Constant}}{1 - \frac{8}{(n\pi)^2} \times \frac{R_2}{R_1} \times \text{Constant}} \approx n^2,$$

which matches with the 4-path passive mixer [10]. Likewise, using (4.12) and (4.18), the harmonic selectivity at V_i is derived as,

$$\frac{V_i(\omega_s)}{V_i(n\omega_s)} \approx \frac{R_L + \frac{8}{\pi^2} \times R_{F1}}{R_L + \frac{8}{(n\pi)^2} \times R_{F1}} < n^2.$$

Obviously, the harmonic selectivity at V_i is smaller than that at V_o with the design parameters used here.

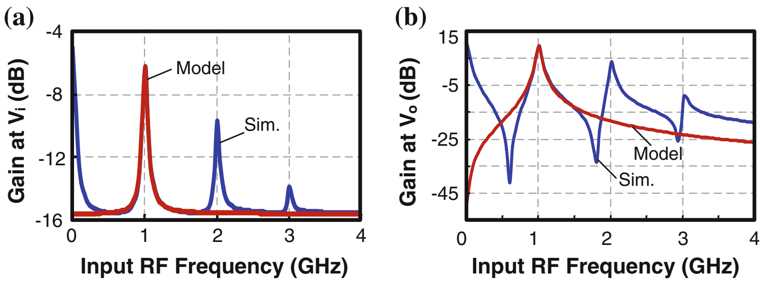

Fig. 4.5 Comparison between the simulation and the analytic derived model using (4.21), (4.22): **a** gain at V_i, and **b** gain at V_o. The parameters are $R_{sw} = 10\ \Omega$, $R_L = 80\ \Omega$, $R_S = 50\ \Omega$, $C_i = 5$ pF, $g_m = 100$ mS, $R_{F1} = 500\ \Omega$, $f_s = 1$ GHz and $N = 4$

The above analysis has ignored the even-order harmonic selectivity which should be considered in single-ended designs. The harmonic selectivity for N = 4 and N = 8 with a fixed total value of capacitance and $g_m R_{sw} = 1$ are shown in Fig. 4.6a, b, respectively. For N = 4, $V_o(3\omega_s)/V_o(\omega_s) = 18.67$ dB and $V_i(3\omega_s)/V_i(\omega_s) = 7.6$ dB, close to the above analysis. Moreover, the relative harmonic selectivity can be decreased by raising N. Furthermore, as derived in (4.4), $g_m R_{sw} = 1$ results in a stronger OB attenuation at far out frequencies that are irrelevant to N. Finally, the bandwidth at V_i and V_o can be kept constant if the total amount of capacitors is fixed under different N. This will be quite explicit when the equivalent circuit will be presented later in Sect. 4.3.3.

For N = 4, the simulated harmonic folding at V_i and V_o are shown in Fig. 4.7a, b, respectively, which obey well (4.12), (4.13) and (4.16) (not plotted). Similar to the N-path passive mixers, the input frequencies around $k(N \pm 1)f_s$ will be folded onto the desired frequency around f_s. The strongest folding term is from 3 f_s when k = 1, and will become smaller if k (integer number) is increased. The relative harmonic folding $\Delta HF_i = 20\log[V_{i,de}(j\omega)] - 20\log[V_{i,un}(j\omega)]$ and $\Delta HF_o = 20\log[V_{o,de}(j\omega)] - 20\log[V_{o,un}(j\omega)]$ are plotted in Fig. 4.8a, b, respectively. The relative harmonic folding is smaller at V_i than at $V_{o,}$ which is preferable because harmonic folding at V_i cannot be filtered.

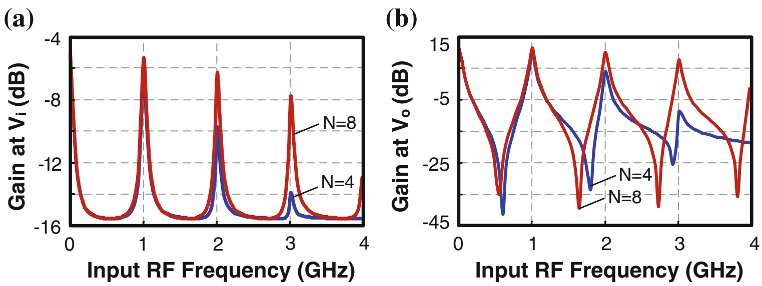

Fig. 4.6 Simulated responses under N = 4 and N = 8: **a** gain at V_i, and **b** gain at V_o. The responses are consistent with Eq. (4.17) (not plotted)

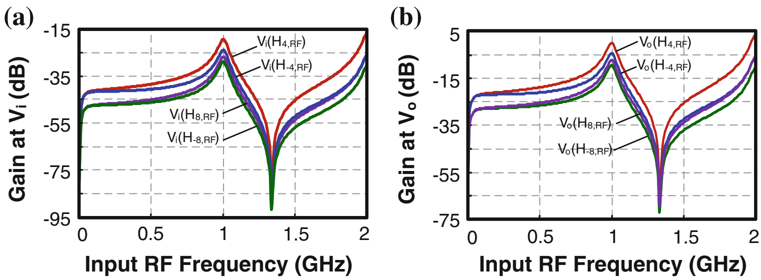

Fig. 4.7 Simulated harmonic folding effects under N = 4: **a** gain at V_i, and **b** gain at V_o. The responses are consistent with Eq. (4.16) (not plotted)

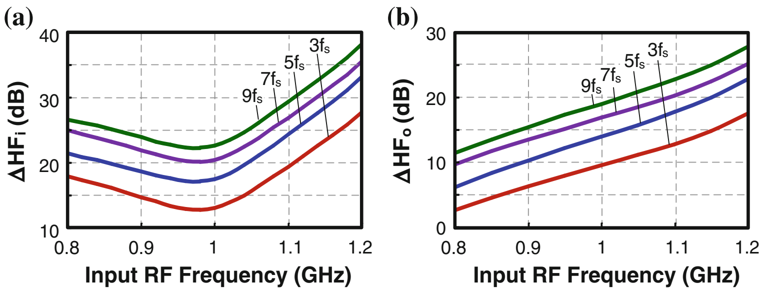

Fig. 4.8 Simulated harmonic folding gain (normalized) under N = 4: **a** at V_i and **b** at V_o

4.3.2 *Noise*

The output noises under consideration are the thermal noises from R_s, R_{sw} and G_m. Since the power spectral density (PSD) of these noise sources are wideband, harmonic folding noise should be considered. The model to derive those noise transfer functions is shown in Fig. 4.9.

Fig. 4.9 Equivalent noise model of the GB-BPF

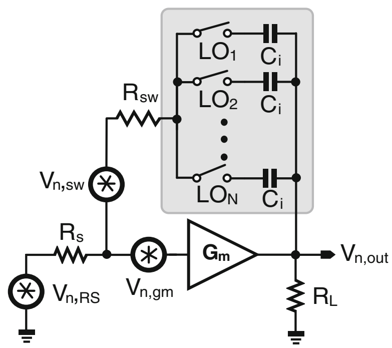

To calculate the noise from R_s to V_o (4.13) needs to be revised in order to obtain,n,

$$\overline{V^2_{n,out,RS}} = \underbrace{\left|\frac{R_{F1}R_L\left(1 - g_m R_{sw} + \frac{R_{sw}}{R_{F1}}\right)}{R_{F1}R_{SW} + (R_{F1} + R_{sw})(R_s + g_m R_L R_s + R_L)}\right|^2}_{\text{Part A}}$$
$$\underbrace{\times \left|V_{n,RS}(j\omega)\right|^2 \times \left|1 - \frac{H_{0,RF}(j\omega)(1 + g_m R_s)}{\left(1 - g_m R_{sw} + \frac{R_{sw}}{R_{F1}}\right)}\right|^2}_{\text{PartA}}$$
$$+ \underbrace{\left|\frac{R_{F1}R_L(1 + g_m R_s)}{R_{F1}R_{SW} + (R_{F1} + R_{sw})(R_s + g_m R_L R_s + R_L)}\right|^2}_{\text{Part B}}$$
$$\underbrace{\times \sum_{n=-\infty, n\neq 0}^{\infty} \left|H_{n,RF}(j\omega)\; V_{n,RS}(j(\omega - n\omega_s))\right|^2}_{\text{Part B}}. \tag{4.23}$$

In (4.23), Part A is the output noise PSD due to R_s without frequency translation, while Part B is due to harmonic folding. Similarly, linear analysis of $v_{n,sw}(t)$ results in the state-space description,

$$\frac{d\upsilon_{Ci}(t)}{dt} = \frac{\upsilon_{n,sw}(t)}{C_i R_1} - \frac{\upsilon_{Ci}(t)}{C_i R_2} \tag{4.24}$$

where

$$R_1 = \frac{-(1 + \alpha_2 R_{sw})}{\alpha_2}, R_2 = -R_1,$$
$$\alpha_2 = \frac{\left(\frac{1}{R_{F1}} + \frac{1}{R_S} + \frac{R_L}{R_{F1}R_S} + \frac{g_m R_L}{R_{F1}}\right)}{\left(1 + g_m R_L + \frac{R_L}{R_S}\right)}.$$

with a minus sign in R_1. Combining (4.24) with (4.16) and (4.17), the output noise PSD transfer function of R_{sw} from $V_{n,sw}$ to V_{ci} [i.e., $H_{0,sw}(j\omega)$] and its harmonic folding [i.e., $H_{n,sw}(j\omega)$] can be derived, leading to the final output noise of PSD to V_o expressed as,

$$\overline{V^2_{n,out,sw}} = \underbrace{\frac{\left|V_{n,sw}(j\omega)\right|^2\left|(1+H_{0,sw})\right|^2}{\left|\left(-\frac{R_S}{\gamma_2 R_L} - 1 - \frac{R_{sw}}{\gamma_2 R_L} - \frac{R_{sw}}{R_{F1}} - \frac{R_{sw}R_S}{\gamma_2 R_L R_{F1}}\right)\right|^2}}_{\text{Part A}} + \underbrace{\sum_{n=-\infty, n\neq 0}^{\infty}\left|\frac{H_{n,sw}(j\omega)V_{n,sw}(j\omega - jn\omega_s)}{-\frac{R_S}{\gamma_2 R_L} - 1 - \frac{R_{sw}}{\gamma_2 R_L} - \frac{R_{sw}}{R_{F1}} - \frac{R_{sw}R_S}{\gamma_2 R_L R_{F1}}}\right|^2}_{\text{Part B}} \quad (4.25)$$

where

$$\gamma_2 = 1 + g_m R_s.$$

In (4.25), Part A is the noise transfer function without harmonic folding, while Part B corresponds to the harmonic folding. Similarly, linear analysis of $\upsilon_{n,gm}(t)$ has the state-space description

$$\frac{d\upsilon_{Ci}(t)}{dt} = \frac{\upsilon_{n,gm}(t)}{C_i R_1} - \frac{\upsilon_{Ci}(t)}{C_i R_2} \quad (4.26)$$

where

$$R_1 = \frac{\alpha_3 + \frac{R_s}{R_L}}{\alpha_3\beta_3 + \beta_3\frac{R_s}{R_L} - \gamma_3 g_m R_s}, R_2 = \frac{\alpha_3 + \frac{R_s}{R_L}}{\alpha_3\gamma_3}$$

$$\alpha_3 = 1 + g_m R_s,\ \beta_3 = \frac{g_m}{\alpha_3}\left(\frac{R_s}{R_{F1}} + 1\right)$$

$$\gamma_3 = \frac{1}{R_L} + \frac{1}{R_{F1}} - \frac{g_m R_s}{\alpha_3 R_L} + \frac{R_s}{\alpha_3 R_L R_{F1}}.$$

From (4.26) together with (4.16) and (4.17), the output noise PSD transfer function of G_m stage from $V_{n,gm}$ to V_{ci} [i.e., $H_{0,gm}(j\omega)$] and its harmonic folding [i.e., $H_{n,gm}(j\omega)$] can be derived. Finally, the output noise PSD to V_o is,

$$\overline{V^2_{n,out,gm}} = \underbrace{\frac{\left|V_{n,gm}(j\omega)\right|^2\left|g_m + H_{0,gm}g_m + \frac{H_{0,gm}}{R_S}\right|^2}{\left|\frac{1}{R_s} + \frac{1}{R_L} + g_m\right|^2}}_{\text{Part A}} + \underbrace{\sum_{n=-\infty, n\neq 0}^{\infty}\left|g_m\frac{H_{n,gm}(j\omega)V_{n,gm}(j\omega - jn\omega_s)}{\frac{1}{R_s} + \frac{1}{R_L} + g_m}\right|^2}_{\text{Part B}}. \quad (4.27)$$

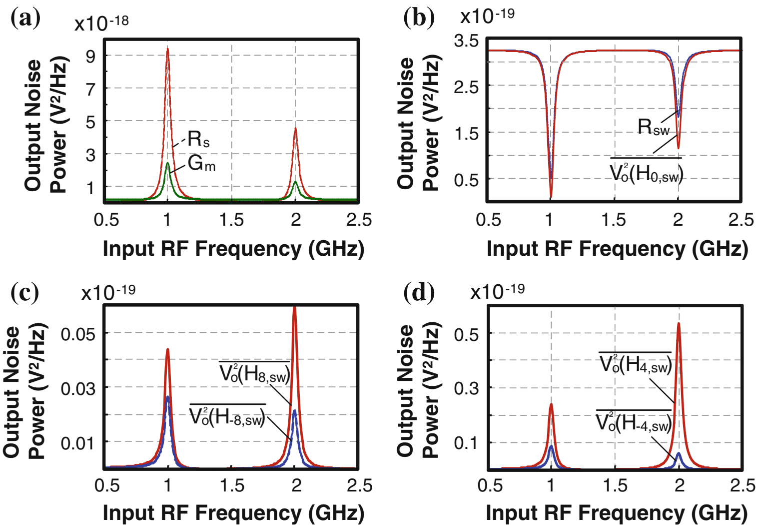

Fig. 4.10 Simulated output noise power at V_o due to: **a** R_S and G_m, and **b** R_{sw}. The results are consistent with Eqs. (4.23), (4.25) and (4.27) (not plotted). The output noise power $\overline{V_o^2(H_0(j\omega))}$ with notch shape of R_{sw} is plotted in **b** using Eq. (4.25) Part A. The harmonic folding parts $\overline{V_o^2(H_{\pm 4}(j\omega))}$ and $\overline{V_o^2(H_{\pm 8}(j\omega))}$ using Eq. (4.25) Part B are plotted in **c** and **d**. The parameters are $R_{sw} = 30\ \Omega$, $R_L = 80\ \Omega$, $R_S = 50\ \Omega$, $C_i = 5$ pF, $g_m = 100$ mS, $R_{F1} = 500\ \Omega$, $f_s = 1$ GHz, $N = 4$, $\overline{V_{n,sw}^2} = 4kTR_{sw} = 4.968 \times 10^{-19}\left(V^2/Hz\right)$, $\overline{V_{n,Rs}^2} = 4kTR_s = 8.28 \times 10^{-19}\left(V^2/Hz\right)$ and $\overline{V_{n,gm}^2} = 4kT/g_m = 1.656 \times 10^{-19}\left(V^2/Hz\right)$

The simulated output noises at V_o due to $\upsilon_{n,RS}(t)$ and $\upsilon_{n,gm}(t)$ are shown in Fig. 4.10a, whereas Fig. 4.10b, c show the output noise due to $\upsilon_{n,sw}(t)$ and its key harmonic folding terms, respectively. Similar to the signal transfer function, the output noises from R_S and G_m are alike a comb, and can be considered as narrowband around $n\omega_s$. Unlike the traditional wideband LNAs that have wideband output noise, here the output noise around the LO harmonics is much less than that at the LO 1st harmonic. Thus, a wideband passive mixer follows the GB-BPF for downconversion, with the noise due to harmonic folding being much relaxed. Besides, the noise transfer function of R_{sw} is a notch function, while its harmonic folding terms are bandpass with much smaller amplitude. This is also true for the conventional N-path passive mixer as analyzed in [15, Eq. 45] with a difference method. Around $n\omega_s$ where the in-band signal exists, the main contribution to its noise is the folding from higher harmonics, which is much less than the OB noise. The noise from R_{sw} is thus greatly suppressed, and a larger R_{sw} is allowed to relax the LO power. In other words, by re-sizing g_m, smaller switches can be used for the SC branch while keeping a high OB selectivity filtering profile.

4.3.3 Intuitive Equivalent Circuit Model

As shown in Fig. 4.5a, b, the filtering behavior at both V_i and V_o are similar to that of a single-ended passive mixer, which motivates the re-modeling of the circuit in Fig. 4.1a with two sets of single-ended passive mixers: one at V_i and one at V_o, as shown in Fig. 4.11a. With the proposed intuitive equivalent circuit, it is convenient to include the parasitic capacitances at both V_i and V_o by using a known theory developed in [11, 16] as shown in Fig. 4.11b. The non-idealities due to LO phase/duty cycle mismatch can be analyzed similar to [16], while the variation of g_m to the in-band gain is similar to the condition of a simple inverter since the two sets of passive mixer are of high impedance at the clock frequency. Inside, we re-model the switch's on-resistance as R_{swi} at V_i with capacitance C_{ie}, and R_{swo} at V_o with capacitance C_{oe}.

$$\begin{cases} R_{swi} = \frac{(R_{sw}//R_{F1})+R_L}{1+g_m R_L} \approx \frac{R_{sw}+R_L}{1+g_m R_L} \\ C_{ie} = \left|\frac{(1-g_m R_{F1})R_L}{R_L+R_{F1}}\right| \times C_i \\ R_{swo} = \frac{(R_{sw}//R_{F1})+R_s}{1+g_m R_s} \\ C_{oe} = C_i. \end{cases} \tag{4.28}$$

R_{swi} described in (4.28) equals to (4.2). Thus, for far-out blockers, $R_{swi}//R_{ie}$ is smaller than R_i, which results in better ultimate rejection (Fig. 4.11a). The value of C_{ie} is obvious, it equals the gain of the circuit multiplied by C_i, but without the SC branch in the feedback. It can be designated as the open-SC gain, and it can be enlarged to save area for a specific –3-dB bandwidth. As an example, with $R_L = 80\ \Omega$, $R_{sw} = 30\ \Omega$, $R_S = 50\ \Omega$, $C_i = 5$ pF, $g_m = 100$ mS and $R_{F1} = 500\ \Omega$, C_{ie} is calculated to be 33.79 pF, which is $\sim$6× smaller than C_i in the traditional design [10], thus the area saving in C_i is significant. For R_{swo}, it equals the output resistance with R_{sw} in the feedback. This is an approximated model without considering the loading from R_{swi} to R_{swo}.

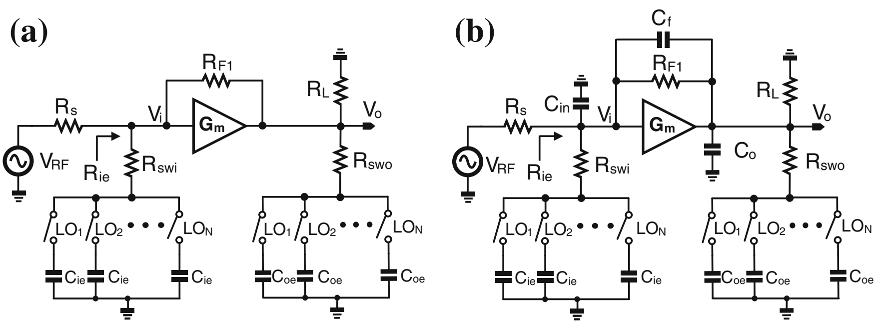

Fig. 4.11 Intuitive equivalent circuit of the GB-BPF: **a** a typical G_m, and **b** a non-ideal G_m with parasitic capacitances C_{in}, C_o and C_f

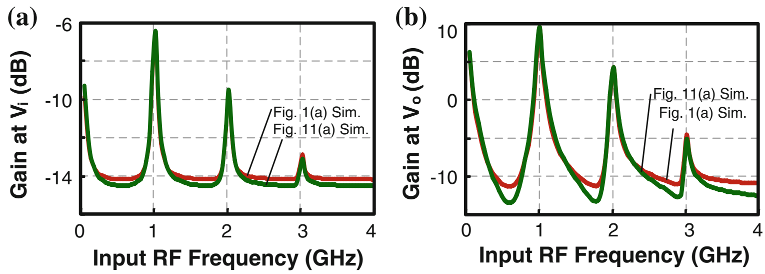

Fig. 4.12 Simulation comparison of Figs. 4.1a and 4.11a: **a** gain at V_i and **b** gain at V_o. The parameters are $R_{sw} = 30\ \Omega$, $R_L = 80\ \Omega$, $R_S = 50\ \Omega$, $C_i = 5$ pF, $g_m = 100$ mS, $R_{F1} = 500\ \Omega$, $f_{Lo} = 1$ GHz and $N = 4$

To verify it, the frequency responses of Figs. 4.1a and 4.11a are plotted together in Fig. 4.12a, b for comparison. It is observed that their –3-dB bandwidth and gain around ω_s fit well with each other, since the loading from the mutual coupling between the SC for IB signal is less an issue than that of OB blockers. As expected, the ultimate rejection in Fig. 4.11a is better than that in Fig. 4.1a. Note that the parasitic capacitances C_{in} at V_i and C_o at V_o have been included in Fig. 4.11b. Also, to account C_{gs} of the G_m's two MOSFETs (Fig. 4.1a), a parasitic capacitance C_f is placed in parallel with R_{F1}. Still, the accuracy of the equivalent circuit is acceptable around f_s, as shown in Fig. 4.13a, b. It is noteworthy that the gain at around ω_s fits better with each other than that of $2\omega_s$, $3\omega_s$, etc. For the influence of C_{in} and C_o, it mainly lowers the IB gain and slightly shifts the resonant frequency [4, 16]. For C_f, it induces Miller equivalent capacitances at V_i and V_o, further lowering the gain and shifting the center frequency. With (4.28) and the RLC model, the –3-dB bandwidth at V_i is derived as,

$$2\Delta f_{i3dB} = \frac{1}{4\pi(R_s // \frac{R_{F1}+R_L}{1+g_m R_L})C_{i.e.}}.$$

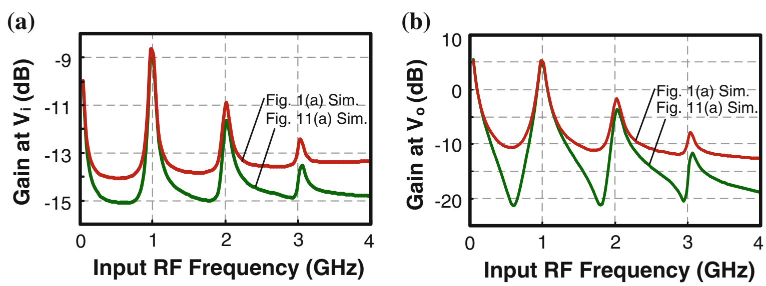

Fig. 4.13 Simulation comparison of Fig. 4.11a, b: **a** gain at V_i and **b** gain at V_o. The parameters are the same as Fig. 4.12, with the additional $C_{in} = 1$ pF, $C_o = 1$ pF and $C_f = 500$ fF

4.4 Design Example

A 4-path GB-BPF suitable for full-band mobile-TV or IEEE 802.11af cognitive radio is designed and simulated with 65-nm GP CMOS technology. The circuit parameters are summarized in Table 4.1. The transistor sizes for the self-biased inverter-based G_m are: $(W/L)_{PMOS} = (24/0.1) \times 4$ and $(W/L)_{NMOS} = (12/0.1) \times 4$. The 0.1-µm channel length is to raise the gain for a given power and g_m value. The switches are NMOS with $(W/L)_{sw} = 25/0.06$. C_i is realized with MiM capacitor.

As shown in Fig. 4.14a, the passband is LO-defined under f_s = 0.5, 1, 1.5 and 2 GHz and $S_{11} \leq 15$ dB in all cases. The –3-dB BW ranges between 41 and 48 MHz, and is achieved with a total MiM capacitance of 20 pF. The calculated C_{ie} based on (4.28) is thus ~40 pF, and the required C_{ie} for 4 paths is 160 pF. The –3-dB BW at 2 GHz is larger due the parasitic capacitor that reduces the Q of the GB-BPF. The gain is 12.5 dB at 0.5-GHz RF, which drops to 11 dB at 2-GHz RF with an increase of NF by <0.1 dB as shown in Fig. 4.14b. The IIP3 improves from IB (–2 dBm) to OB (+21.5 dBm at 150-MHz offset) as shown in Fig. 4.14c. For the circuit non-idealities, 10 % of LO duty cycle mismatch only induce a small variation of IB gain by around 0.05 dB. For a g_m variation of 10 %, the IB gain variation is 0.07 dB at 500-MHz LO frequency. The performance summary is given in Table 4.2.

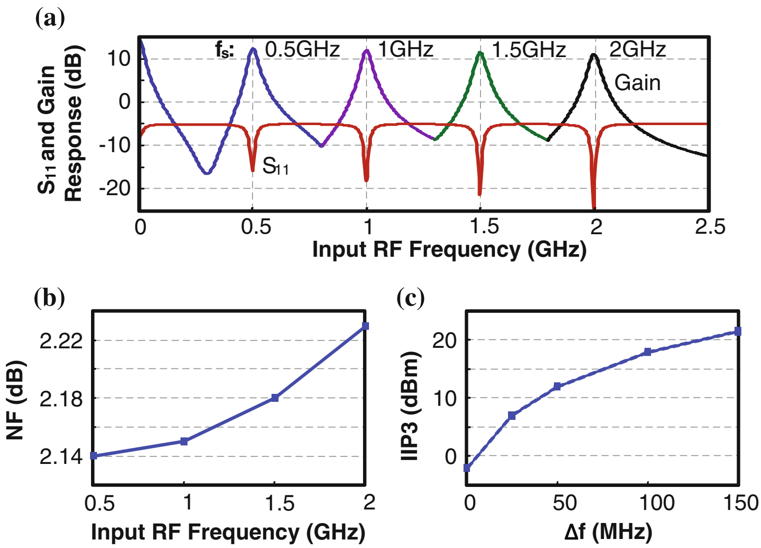

Fig. 4.14 Simulated **a** voltage gain and S_{11} with different f_s showing the LO-defined bandpass responses. **b** NF versus input RF frequency. **c** IB and OB IIP3

Table 4.1 Key parameters in the design example

g_m (mS)	R_{sw} (Ω)	R_{F1} (Ω)	R_L (Ω)	C_i (pF)
76	20	1 k	120	5

Table 4.2 Simulated performance summary in 65-nm CMOS

Tunable RF (GHz)	0.5–2
Gain (dB)	11–12.5
NF (dB)	2.14–2.23
$IIP3_{IB}$ (dBm)[1] $IIP3_{OB}$ (dBm) (Δf = +25 MHz)[1] $IIP3_{OB}$ (dBm) (Δf = +50 MHz)[1] $IIP3_{OB}$ (dBm) (Δf = +100 MHz)[1] $IIP3_{OB}$ (dBm) (Δf = +150 MHz)[1]	−2 +7 +12 +18 +21.5
BW (MHz)	41–48
Power (mW) @ Supply (V)	7 @ 1

[1] f_s = 500 MHz, two tones at f_s + Δf + 2 MHz and f_s + 2Δf + 4 MHz

4.5 Conclusions

This chapter has described the analysis, modeling and design of a GB-BPF that features a number of attractive properties. By using a transconductance amplifier (G_m) as the forward path and an N-path SC branch as its feedback path, double RF filtering at the input and output ports of the G_m is achieved concurrently. Moreover, when designed for input impedance matching, both in-band gain and bandwidth can be customized due to the flexibility created by G_m. Both the power and area efficiencies are improved when compared with the traditional passive N-path filter due the loop gain offered by G_m. All gain and bandwidth characteristics have been verified using a RLC model first, and later with the LPTV analysis to derive the R, L and C expressions. The harmonic selectivity, harmonic folding and noise have been analyzed and verified by simulations, revealing that the noise of the switches is notched at the output, benefitting the use of small switches for the SC branch, saving the LO power without sacrificing the selectivity. The design example is a 4-path GB-BPF. It shows >11 dB gain, <2.3-dB NF over 0.5-to-2-GHz RF, and +21-dBm out-of-band IIP3 at 150-MHz offset, at just 7 mW of power. The developed models also backup the design of the ultra-low-power receiver in [9] for multi-band sub-GHz ZigBee applications.

Appendix A: The Derivation of Eq. (4.18)

Here we rewrite Eq. 4.17 as follows:

$$H_{0,RF}(j\omega) = \frac{\omega_{rc,B}}{\omega_{rc,A} + j\omega} + \frac{1 - e^{j(\omega)(T_{S-}\tau_m)}}{\omega_{rc,A} + j\omega} G_{SE}(j\omega) f_s N \tag{A.1}$$

$$G_{SE}(j\omega) = \frac{e^{j\omega\tau_m} - e^{-\omega_{rc,A}\tau_m}}{e^{j2\pi\omega/\omega_s} - e^{-\omega_{rc,A}\tau_m}} * \frac{1}{\frac{\omega_{rc,A}}{\omega_{rc,B}} + \frac{j\omega}{\omega_{rc,B}}}$$

Let $\omega = n\omega_s$ and assume $\omega_{rc,B}$ and $\omega_{rc,A} \ll \omega_s$, we have

$$\frac{\omega_{rc,B}}{\omega_{rc,A} + j\omega} = \frac{\omega_{rc,B}}{\omega_{rc,A} + jn\omega_s} \approx \frac{\omega_{rc,B}}{jn\omega_s} \approx 0 \tag{A.2}$$

$$\frac{1 - e^{j\omega(T_S - \tau_m)}}{\omega_{rc,A} + j\omega} = \frac{1 - e^{jn\omega_s(T_S - DT_S)}}{\omega_{rc,A} + jn\omega_s} \approx \frac{1 - e^{jn\omega_s T_S(1-D)}}{jn\omega_s} = \frac{1 - e^{-j2\pi nD}}{jn\omega_s} \tag{A.3}$$

$$\begin{aligned}
&\frac{e^{j\omega\tau_m} - e^{-\omega_{rc,A}\tau_m}}{e^{j2\pi\omega/\omega_s} - e^{-\omega_{rc,A}\tau_m}} * \frac{1}{\frac{\omega_{rc,A}}{\omega_{rc,B}} + \frac{j\omega}{\omega_{rc,B}}} \approx \frac{e^{jn\omega_s\tau_m} - e^{-\omega_{rc,A}\tau_m}}{e^{j2\pi n} - e^{-\omega_{rc,A}\tau_m}} * \frac{\omega_{rc,B}}{jn\omega_s} \\
&= \frac{e^{jn\omega_s DT_S} - e^{-\omega_{rc,A}DT_S}}{e^{j2\pi n} - e^{-\omega_{rc,A}DT_S}} * \frac{\omega_{rc,B}}{jn\omega_s} = \frac{e^{jn\omega_s DT_S + \omega_{rc,A}DT_S} - 1}{e^{j2\pi n + \omega_{rc,A}DT_S} - 1} * \frac{\omega_{rc,B}}{jn\omega_s} \\
&= \frac{e^{jn\omega_s DT_S + \frac{\omega_{rc,A}D2\pi}{\omega_s}} - 1}{e^{j2\pi n + \frac{\omega_{rc,A}D2\pi}{\omega_s}} - 1} * \frac{\omega_{rc,B}}{jn\omega_s} \approx \frac{e^{jn\omega_s DT_S} - 1}{e^{\frac{\omega_{rc,A}D2\pi}{\omega_s}} - 1} * \frac{\omega_{rc,B}}{jn\omega_s} \\
&\approx \frac{e^{jn\omega_s DT_S} - 1}{\frac{\omega_{rc,A}D2\pi}{\omega_s}} * \frac{\omega_{rc,B}}{jn\omega_s} = \frac{e^{jn\omega_s DT_S} - 1}{\omega_{rc,A}D2\pi} * \frac{\omega_{rc,B}}{jn}
\end{aligned} \tag{A.4}$$

Substitute (A.2)–(A.4) into (A.1), we get

$$\begin{aligned}
H_{0,RF}(n\omega_s) &\approx \frac{1 - e^{-j2\pi nD}}{jn\omega_s} * \frac{e^{jn\omega_s DT_S} - 1}{\omega_{rc,A}D2\pi} * \frac{\omega_{rc,B}}{jn} * f_s N \\
&= \frac{1 - e^{-j2\pi nD}}{jn\omega_s} * \frac{e^{j2\pi nD} - 1}{\omega_{rc,A}D2\pi} * \frac{\omega_{rc,B}}{jn} * f_s N \\
&= -\frac{N\omega_{rc,B}(e^{j2\pi nD} - 2 + e^{-j2\pi nD})}{\omega_{rc,A}D(n2\pi)^2} \\
&= \frac{2N(1 - \cos 2\pi nD)}{4D(n\pi)^2} * \frac{\omega_{rc,B}}{\omega_{rc,A}}
\end{aligned}$$

Around the clock frequency ω_s, n should be equal to 1.

Appendix B: The Derivation of L_p and C_p

First, the relationship between V_p and V_{RF} should be derived, where V_p is the voltage across L_p. From Fig. 4.1b, we have

$$\begin{cases} V_1 = V_p + V_0 \\ \frac{V_i - V_1}{R_{sw}} + \frac{V_i - V_0}{R_F} = g_m V_i + \frac{V_0}{R_L} \\ \frac{V_{RF} - V_i}{R_S} = g_m V_i + \frac{V_0}{R_L} \end{cases} \tag{B.1}$$

Simplified (B.1), we get

$$V_p = \frac{V_{RF}}{\frac{\epsilon_1}{R_{sw}} + \beta_1 \epsilon_1 * \gamma_1} \tag{B.2}$$

where

$$\beta_1 = \frac{\frac{1}{R_L} + \frac{1}{R_{F1}} + \frac{1}{R_{sw}} + \frac{\alpha_1 R_s}{R_L(1 + g_m R_s)}}{\frac{1}{R_L} + g_m}$$

$$\alpha_1 = \frac{1}{R_{sw}} + \frac{1}{R_{F1}} - g_m$$

$$\gamma_1 = -\frac{\alpha_1 \beta_1 R_{sw}^2}{\beta_1 - 1 - \alpha_1 \beta_1 R_{sw}}$$

$$\epsilon_1 = \frac{1 + g_m R_s}{\alpha_1}$$

Since V_p should be the same either it is derived from the $R_pL_pC_p$ model or from the LPTV analysis. That is $V_p = V_{Ci}$, where V_{Ci} is the voltage across C_i in LPTV analysis. Let the denominator of (B.2) equal to zero, that is

$$\frac{\epsilon_1}{R_{sw}} + \beta_1 \epsilon_1 * \gamma_1 = 0 \tag{B.3}$$

From (B.3), we have

$$Z_p = \frac{\alpha_1 \beta_1 R_{sw}^2}{\beta_1 - 1 - \alpha_1 \beta_1 R_{sw}} = -\gamma_1 = \frac{sR_pL_p}{R_p + sL_p + s^2 L_p R_p C_p} \tag{B.4}$$

where $Z_p = sL_p//(1/sC_p)//R_p$.

Besides, from Eq. 4.17, we recognize that when $s = -\frac{1}{N} * \omega_{rcA} \pm j\omega_s$, V_{Ci} will be infinity. Thus, substitute the above s value into (B.4), we have

$$\gamma_1 R_p + \left(-\frac{1}{N} * \omega_{rca} \pm j\omega_s\right)\left(\gamma_1 L_p + L_p R_p\right) + \left(-\frac{1}{N} * \omega_{rca} \pm j\omega_s\right)^2 \gamma_1 L_p R_p C_p = 0 \tag{B.5}$$

For (B.5) to be satisfied, both of its imaginary part and real part should equal to zero simultaneously. Thus, we get

$$C_p = \frac{\gamma_1 + R_p}{2D\omega_{rc,A}\gamma_1 R_p}$$

$$L_p = \frac{\gamma_1 R_p}{D\omega_{rc,A}\left(\gamma_1 + R_p\right) - \left(D^2\omega_{rc,A}^2 - \omega_s^2\right)\gamma_1 R_p C_p}$$

where D = 1/N is the duty cycle of the LO.

References

1. C. Andrews, A. Molnar, A passive mixer-first receiver with digitally controlled and widely tunable RF interface. IEEE J. Solid-State Circ. **45**, 2696–2708 (2010)
2. C. Andrews, A. Molnar, Implications of passive mixer transparency for impedance matching and noise figure in passive mixer-first receivers. IEEE Trans. Circ. Syst. I, Reg. Pap. **57**, 3092–3103 (2010)
3. D. Murphy, H. Darabi, A. Abidi, A. Hafez, A. Mirzaei, M. Mikhemar, M. Chang, A blocker-tolerant, noise-cancelling receiver suitable for wideband wireless applications. IEEE J. Solid-State Circ. **47**(12), 2943–2963 (2012)
4. M. Darvishi, R. van der Zee, B. Nauta, Design of active N-Path filters. IEEE J. Solid-State Circ. **48**(12), 2962–2976 (2013)
5. A. Mirzaei, H. Darabi, A. Yazdi, Z. Zhou, E. Chang, P. Suri, A 65 nm CMOS quad-band SAW-less receiver SOC for GSM/GPRS/ EDGE. IEEE J. Solid-State Circ. **46**(4), 950–964 (2011)
6. A. Mirzaei, H. Darabi, D. Murphy, A low-power process- scalable superheterodyne receiver with integrated High-Q filters, ISSCC Dig. Tech. Papers, pp. 60–61, Feb. 2011
7. S. Youssef, R. van der Zee, B. Nauta, Active feedback technique for RF channel selection in front-end receivers *IEEE*. J. Solid-State Circ. **47**, 3130–3144 (2012)
8. M. Darvishi, R. van der Zee, E. Klumperink, B. Nauta, Widely tunable 4th order switched G_m-C band-pass filter based on N-Path filters. IEEE J. Solid-State Circ. **47**(12), 3105–3119 (2012)
9. Z. Lin, P.-I. Mak, R.P. Martins, A 0.5 V 1.15 mW 0.2 mm^2 Sub- GHz ZigBee receiver supporting 433/860/915/960 MHz ISM bands with zero external components. ISSCC Dig. Tech. Papers, pp. 164–165, Feb. 2014
10. A. Ghaffari, E. Klumperink, M. Soer, B. Nauta, Tunable High-Q N-path band-pass filters: modeling and verification. IEEE J. Solid State Circ. **46**(5), 998–1010 (2011)
11. A. Mirzaei, H. Darabi, J. Leete et al., Analysis and optimization of direct-conversion receivers with 25 % duty-cycle current-driven passive mixers. IEEE Trans. Circ. Syst. I, Reg. Pap. **57**, 2353–2366 (2010)
12. B. Razavi, *RF Microelectronics*, 2nd edn. (Prentice-Hall, New Jercy, 2011)

13. M. Soer, E. Klumperink, P. deBoer, F. vanVliet, B. Nauta, Unified frequency domain analysis of switched-series-RC passive mixers and samplers. IEEE Trans. Circuits Syst. I, Reg. Papers, vol. 57, no. 10, pp. 2618–2631, Oct. 2010
14. A. Ghaffari, E. Klumperink, M. Soer, B. Nauta, Tunable N-Path notch filters for blocker suppression: modeling and verification. IEEE J. Solid-State Circ. **48**, 1370–1382 (2013)
15. A. Mirzaei, H. Darabi, D. Murphy, Architectural evolution of integrated M-Phase High-Q bandpass filters. IEEE Trans. Circuits Syst. I, Reg. Papers, vol. 59, no. 1, pp. 52–65, Jan. 2012
16. A. Mirzaei, H. Darabi, Analysis of imperfections on performance of 4-Phase passive-mixer-based High-Q bandpass filters in SAW-less receivers. IEEE Trans. Circ. Syst. I, Reg. Pap. **58**(5), 879–892 (2011)

Chapter 5
A Sub-GHz Multi-ISM-Band ZigBee Receiver Using Function-Reuse and Gain-Boosted N-Path Techniques for IoT Applications

5.1 Introduction

Internet of Things (IoT) represents a competitive and large market for short-range ultra-low-power (ULP) wireless connectivity [1, 2]. According to [3], by 2020 the IoT market will be close to hundreds of billion dollars (annually $\sim$16 billions). To bring down the hardware cost of such massive inter-connections, sub-GHz ULP wireless products compliant with the existing wireless standard such as the IEEE 802.15.4c/d (ZigBee) will be of great demand, especially for those that can cover all regional ISM bands [e.g., China (433 MHz), Europe (860 MHz), North America (915 MHz) and Japan (960 MHz)]. Together with the obvious goals of small chip area, minimum external components and ultra-low-voltage (ULV) supply (for possible energy harvesting), the design of such a receiver poses significant challenges.

The tradeoffs among multi-band operation, power, area and noise figure (NF) are described in Fig. 5.1. A multi-band receiver (Fig. 5.1a) can be resorted from multiple low-noise amplifiers (LNAs) with shared I/Q mixers and baseband (BB) lowpass filters (LPFs). As such, each LNA and its input matching network can be specifically optimized for one band using passive-LC resonators, improving the NF, selectivity and gain. Although a single wideband LNA with zero LC components is preferred to reduce the die size (Fig. 5.1b), the NF and power requirements of the LNA are much higher. Moreover, when the output noise of the LNA is wideband, more harmonic-folding noise will be induced by its subsequent mixers (under hard switching). All these facts render wideband receivers [4] generally more power hungry than its narrowband counterparts [5–7].

In contrast, a wide-range-tunable narrowband RF front-end is of greater potential to realize a multi-band ULP receiver. While sub-GHz passive LC resonators are

Z. Lin et al., *Ultra-Low-Power and Ultra-Low-Cost Short-Range Wireless Receivers in Nanoscale CMOS*, Analog Circuits and Signal Processing,
DOI 10.1007/978-3-319-21524-2_5

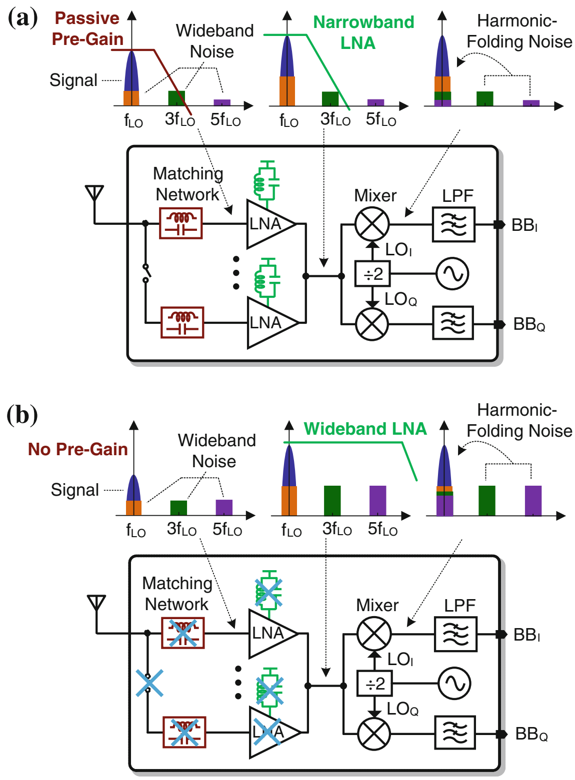

Fig. 5.1 Multi-band receiver **a** Using multiple LNAs and matching networks for pre-gain and pre-filtering, or **b** Using one wideband LNA to save the die area but demanding more power to lower the NF and nonlinearity due to no pre-gain, no pre-filtering and more harmonic-folding noise

area hungry, the N-path switched-capacitor (SC) network [8, 9] appears as a prospective alternative to replace them. It behaves as a tunable lossy LC resonator with its center frequency accurately defined by the clock. Inspired by it, this book introduces a function-reuse RF front-end with signal orthogonality [10], and a gain-boosted N-path SC network [11] for tunable RF filtering and input impedance matching. External components are avoided, while multi-band operation, stronger RF filtering, smaller physical capacitor size, and lower LO power are concurrently achieved when compared with the traditional designs [8, 9]. Together with a low-voltage current-reuse VCO-filter, the described multi-band receiver [12] exhibits comparable performances with respect to other single-band-optimized designs [5–7, 13–16].

Section 5.2 overviews the state-of-the-art ULP techniques. The gain-boosted N-path SC network is detailed in Sect. 5.3, which leads to three receiver architectures having several core properties fundamentally differing from the conventional. Section 5.4 details the design of the current-reuse VCO-filter. Measurement results and performance benchmarks are given in Sect. 5.5, and conclusions are drawn in Sect. 5.6.

5.2 ULP Techniques: Current Reuse, ULV and Proposed Function Reuse + Gain-Boosted N-Path SC Network

Entered into the nanoscale CMOS regime, the transistors feature sufficiently high f_T and low V_T favoring the use of a current-reuse architecture. Moreover, by conveying the signal in the current domain, both the RF bandwidth and linearity can be improved. Our previous work [15, 16] was inspired by those facts; it unifies most RF-to-BB functions in one cell for current-mode signal processing at a typical 1.2-V supply, resulting in a high IIP3 (–6 dBm) at small power (2.7 mW) and area (0.3 mm^2). Yet, for power savings, another 0.6-V supply was still required for the rest of the circuitries, complicating the power management. The 2.4-GHz ULV receiver in [13, 14] facilitates single 0.3-V operation of the entire receiver at 1.6 mW for energy harvesting, but the limited voltage headroom and transistor f_T call for bulky inductors and transformers to assist the biasing and tune out the parasitics, penalizing the area (2.5 mm^2). Finally, since both of them target only the 2.4-GHz band, a fixed LC network (on-chip in [15, 16] and off-chip in [13, 14]) can be employed for input matching and passive pre-gain (save power). This technique is however costly and inflexible for multi-band designs.

The described multi-band receiver is based on a *function-reuse* RF front-end implemented with a gain-boosted N-path SC network. The cost is low and die area is compact (0.2 mm^2) as on/off-chip inductors and transformers are all avoided except the VCO. The power is squeezed by recycling a set of inverter-based amplifiers for concurrent RF (common mode) and BB (differential mode) amplification, resulting in low-voltage (0.5 V) and low-power (1.15 mW) operation.

5.3 Gain-Boosted N-Path SC Networks

The proposed gain-boosted N-path SC network can generate an RF output when it is considered as a LNA or bandpass filter [11], or BB outputs when it is considered as a receiver (this work). We describe three alternatives to realize and study such a network. With the linear periodically time-variant (LPTV) analysis, the BB signal transfer function (STF) and noise transfer function (NTF) are derived and analyzed. Besides, three intuitive functional views are given to model their gain responses.

5.3.1 N-Path Tunable Receiver

According to [9], by having an N-path SC network as the feedback path of a gain stage (labeled with the symbol $4G_m$), an N-path tunable LNA (or bandpass filter) can be realized with the RF output taken at V_o (Fig. 5.2). This topology has a number of core benefits when compared with the existing N-path filtering [8, 9].

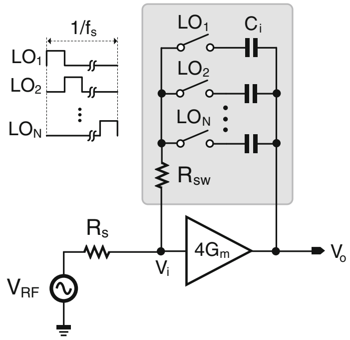

Fig. 5.2 N-path tunable LNA or bandpass filter [11]. It can provide input impedance matching at V_i

First, double-RF filtering at V_i and V_o is achieved with one N-path SC network. Second, tunable input impedance matching is possible at V_i. Third, the loop gain associated with $4G_m$ reduces the impact of R_{sw} (mixer's ON resistance) to the ultimate out-of-band (OB) rejection. Fourth, similar to the continuous-time Miller capacitor, for a given RF bandwidth (BW), the required C_i can be reduced by the loop gain associated with $4G_m$. Fifth, the NTF of R_{sw} to V_o is a notch function around the clock frequency f_s. Thus, small switches are allowed without degrading the NF, saving the LO power. Finally, the output noise at V_o is narrowband with a comb-filter shape, reducing the harmonic-folding noise when it is followed by a wideband passive mixer.

Interestingly, if such an operation principle is extended to Fig. 5.3a–d, the N-path tunable LNA can be viewed as a passive-mixer receiver, with all capacitors C_i driven by a $4G_m$ stage. The BB outputs are taken at $V_{B1\text{-}N}$. Unlike the original passive-mixer-first receiver [17, 18] that offers no gain at $V_{B1\text{-}N}$, this receiver has a

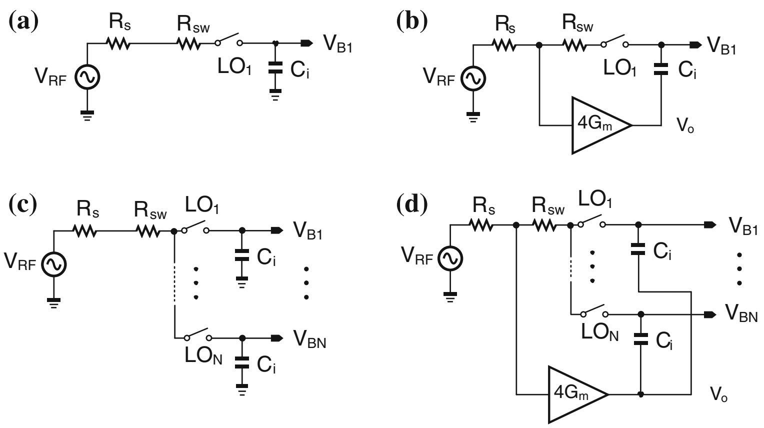

Fig. 5.3 The N-path tunable LNA in Fig. 5.2 can be re-arranged as an N-path tunable receiver by taking the BB outputs at $V_{B1\text{-}N}$ on top of C_i, like a single-path passive mixer with gain boosting as shown in **a**, **b**, or an N-path passive mixer with gain boosting as shown in **c**, **d**

relatively large BB gain at $V_{B1\text{-}N}$ surmounting the NF limitation. The frequency-translational RF filtering at V_i and V_o are realized by LO_1-LO_N to up-convert the BB signals $V_{B1\text{-}N}$ to RF, and in-phase summed together.

To establish a basic operation theory, the analysis below follows the LPTV method [11, 19]. For simplicity, N = 4 is employed to allow basic I/Q downconversion with LO_1-LO_4 as 25 %-duty-cycle non-overlapping clocks. The timing diagram of LO_1 is shown in Fig. 5.4a. $4G_m$ can be based on a self-biased inverter amplifier with g_{m1} as the transconductance, R_L as the output resistance and R_{F1} as the feedback resistor. $LO_{2\text{-}4}$ are similar to LO_1 with a time delay. The analysis is conducted for V_{B1} while for $V_{B2\text{-}4}$, when f_{RF} is around qf_s, the phase relation between the BB voltages V_{Bi} $(1 \le i \le 4)$ can be described by $V_{Bm} = V_{Bn}\, e^{\frac{jq\pi(m-n)}{2}}$, $(1 \le (m,n) \le 4)$. Thus, V_{B1} and V_{B3} (V_{B2} and V_{B4}) are either out-of-phase or in-phase with each other, depending on the input frequency. When LO_1 is high (K = 1), linear analysis reveals the following state-space description,

$$\frac{d\upsilon_{Ci}(t)}{dt} = \frac{\upsilon_{RF}(t)}{C_i R_1} - \frac{\upsilon_{Ci}(t)}{C_i R_2} \tag{5.1}$$

where

$$R_1 = \frac{1 + \frac{R_{sw}}{R_{F1}} + \frac{R_{sw}+R_S}{R_L} + \frac{R_{sw}R_S}{R_{F1}R_L} + g_{m1}R_S + \frac{g_{m1}R_{sw}R_S}{R_{F1}}}{\frac{1}{R_L} + g_{m1}} \tag{5.2}$$

$$R_2 = \frac{1 + \frac{R_{sw}}{R_{F1}} + \frac{R_{sw}+R_S}{R_L} + \frac{R_{sw}R_S}{R_{F1}R_L} + g_{m1}R_S + \frac{g_{m1}R_{sw}R_S}{R_{F1}}}{\frac{1}{R_{F1}} + \frac{1}{R_L} + \frac{R_S}{R_{F1}R_L} + \frac{g_{m1}R_S}{R_{F1}}} \tag{5.3}$$

When LO_1 is low (K = 2), we have

$$\frac{d\upsilon_{Ci}(t)}{dt} = 0 \tag{5.4}$$

From (5.1) to (5.4), the harmonic transfer functions (HTFs) for the intervals K = 1 and K = 2 are derived in (5.5) and (5.6), respectively,

$$H_{n,1,RF}(j\omega) = \frac{\omega_{rc,B}}{\omega_{rc,A} + j\omega} \times \frac{1 - e^{-jn\omega_s\tau_1}}{j2\pi n} + \frac{1 - e^{j\omega\tau_2}}{\omega_{rc,A} + j\omega} G(j\omega) f_s \tag{5.5}$$

$$H_{n,2,RF}(j\omega) = -\frac{1 - e^{j\omega\tau_2}}{j\omega} G(j\omega) f_s \tag{5.6}$$

where,

$$G(j\omega) = \frac{e^{j(\omega - n\omega_s)\tau_1} - e^{-\omega_{rc,A}\tau_1}}{e^{j2\pi(\omega - n\omega_s)/\omega_s} - e^{-\omega_{rc,A}\tau_1}} \times \frac{1}{\frac{\omega_{rc,A}}{\omega_{rc,B}} + \frac{j(\omega - n\omega_s)}{\omega_{rc,B}}} \tag{5.7}$$

$\omega_{rc,A} = 1/R_2C_i$, $\omega_{rc,B} = 1/R_1C_i$, $\tau_1 = \frac{T_s}{4}$ and $\tau_2 = \frac{3T_s}{4}$. Here, $G(j\omega)$ represents the switching moment transfer function as defined and calculated in [11, 19]. By combining (5.5–5.7), the harmonics transfer function from V_{RF} to C_i is derived,

$$H_{n,RF}(j\omega) = \frac{V_{Ci}(j\omega)}{V_{RF}(j\omega)} = H_{n,1,RF}(j\omega) + H_{n,2,RF}(j\omega) \tag{5.8}$$

For the BB signal around f_s, the voltages sampling at C_i are differential, and V_o is thus the virtual ground and the state of the circuit $V_{Ci}(j\omega)$ (voltage across C_i) is equal to $V_{Bm}(j\omega)$, where $1 \leq m \leq 4$. Although the results from the LPTV analysis are exact, they are lacking in conceptual intuition that can be of more practical value for designers. To compare with the usual receiver concept that is based on cascade of blocks, a functional view of a 4-path tunable receiver is given in Fig. 5.4b to model the gain response. An ideal buffer amplifier (infinite input impedance and

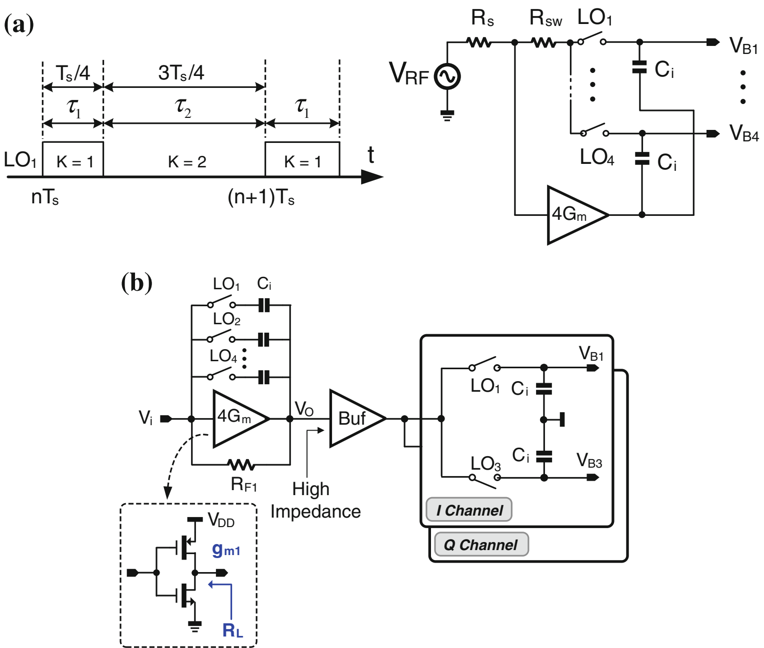

Fig. 5.4 **a** Timing diagram of LO_1 and the 4-path tunable receiver. **b** Functional view of a 4-path tunable receiver to model the gain response

zero output impedance) is introduced into the model implying that the passive mixer has no loading effect to the front-end $4G_m$ stage. Note that the model is inapplicable for studying the noise, since the noise sources from the functional view are separated, and thus considered as uncorrelated. Differently with the noise sources of the proposed receiver, they are considered as correlated. From this functional view, the mixers are reused for two roles: double-RF filtering (i.e., as two N-path filters at both input and output of the gain stage) and frequency down-conversion (i.e., as an N-path mixer). For the associated capacitors, they are also reused for both double-RF filtering (associated with the 4-path SC network) and BB filtering at $V_{B1\text{-}4}$. These properties lower the LO power and chip area while providing stronger RF filtering. For the RF gain at V_o, although it has been studied in [11] by the LPTV analysis, it can also be derived by the upconversion of $V_{B1\text{-}4}$ and summed together at V_o as given by,

$$\upsilon_o(t) = \sum_{m=1}^{4} \upsilon_{Bm}(t) LO_m(t) \tag{5.9}$$

After applying Fourier series analysis to (5.9) around f_s, we have,

$$V_o(j\omega) = \frac{2\sqrt{2}}{\pi} V_{B1}(j\omega) = \frac{\sqrt{2}}{\pi} V_{B1,3}(j\omega) \tag{5.10}$$

which is an approximation as the influence of R_{sw} is ignored. Here $V_{B1,3} = V_{B1} - V_{B3}$. To verify it, the BB and RF STFs of the N-path tunable receiver are plotted together in Fig. 5.5. The RF gain is $\sim$8 dB smaller than that of the BB gain, close to the prediction by (5.10). Also, the BB gain from the functional view is plotted, which fits well with the original gain-boosted in-band (IB) signal.

The power spectral density (PSD) of the BB output noise is derived in Appendix A, while the PSD of the RF output noise at V_o has been studied in [11].

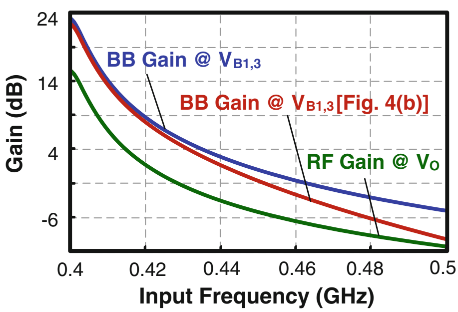

Fig. 5.5 Simulated BB gain and RF gain of the 4-path tunable receiver (Fig. 5.4a), and the simulated BB gain from the functional view in Fig. 5.4b

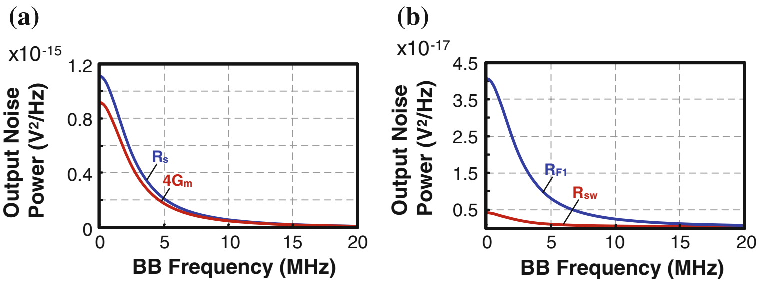

Fig. 5.6 **a** Simulated output-noise PSD at the differential BB outputs ($V_{B1,3}$) due to **a** R_s and $4G_m$. **b** R_{sw} and $R_{F1.}$ The simulation parameters are $R_L = 800\ \Omega$, $R_s = 50\ \Omega$, $R_{sw} = 30\ \Omega$, $g_{m1} = 20.55$ mS, $C_i = 12.5$ pF, $f_s = 400$ MHz, $R_{F1} = 5\ k\Omega$, $\overline{V^2_{n,sw}} = 4kTR_{sw} = 4.968 \times 10^{-19}$ (V^2/Hz), $\overline{V^2_{n,Rs}} = 4kTR_s = 8.28 \times 10^{-19}$ (V^2/Hz), $\overline{V^2_{n,gm1}} = 4kT/g_{m1} = 8.058 \times 10^{-19}$($V^2$/Hz) and $\overline{V^2_{n,RF1}} = 4kTR_{F1} = 828 \times 10^{-19}$ (V^2/Hz)

The simulated results are given in Fig. 5.6 (using the model of Fig. 5.17 in Appendix A). From simulations, the differential output noise power from R_{sw} and R_{F1} are much smaller (around two orders of magnitude) than that from R_s to $4G_m$. Thus, the noise contributions from R_{sw} to R_{F1} are greatly suppressed, making small mixer's switches and large R_{F1} possible (constrained by input impedance matching and the required RF filtering). Unlike the passive-mixer-first receiver [17, 18] where the BB NF from R_{sw} is approximately ($R_{sw}/R_s + \gamma$), here γ is a factor from the harmonic folding. Thus, for the passive-mixer-first design, the BB NF due to R_{sw} is usually of a similar order of magnitude as R_s. Besides, a small R_{sw} and additional LO paths are required to minimize such effect.

We also show the simulated BB NF for $V_{B1,3}$ and RF NF at V_o (Fig. 5.7), where $V_{B1,3} = V_{B1}–V_{B3}$ and similar notations such as $V_{X1,3} = V_{X1}–V_{X3}$ have the same implication in the following text. Interestingly, the BB NF is smaller than the

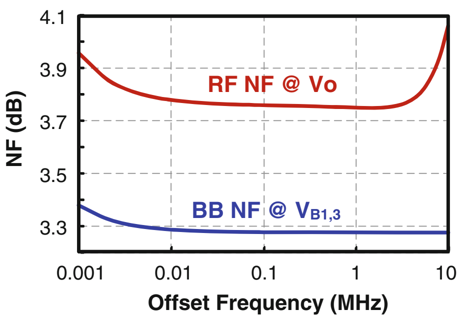

Fig. 5.7 Simulated NF of the N-path tunable receiver with the RF output (RF NF @ V_o) or BB outputs (BB NF @ $V_{B1,3}$)

RF NF at the LNA's output V_o, since the BB gain (or noise) and RF gain (or noise) are concurrent but happened under different STF (or NTFs). This characteristic underlines a fundamentally different concept when compared with the traditional receiver that is based on the cascade of blocks, where the RF NF should be smaller than the BB NF. Note that for the BB NF, the even-harmonic-folding noise due to the LO contributes only common-mode noise at the BB outputs, which will be rejected differentially. However, it will contribute to the RF noise at V_o due to its single-ended nature. This is one of the senses that the BB NF can be smaller than the RF NF. The authors are still pursuing deeper exploration of this topic and this book serves as the foundation. Furthermore, the 1/f noise around DC from the transconductance devices are upconverted to f_s with little influence to the total output noise at DC [as shown in (A.1)]. This was verified by simulations (Fig. 5.7) where the BB NF at 1 kHz has increased by only 0.15 dB. Thus, short channel-length devices can be employed without degrading the BB low-frequency noise.

5.3.2 AC-Coupled N-Path Tunable Receiver

Another alternative to implement such a gain-boosted N-path SC network is shown in Fig. 5.8a. The mixers are placed on the feedback path while the input is AC-coupled by capacitors that simplify the cascading of itself for a higher order of filtering. Without considering the memory effect of capacitor C_i, the operation of this architecture can be explained as follows: Initially, at RF frequency, the capacitor C_i can be assumed as a short circuit. The input signal V_{RF} is thus directly coupled to each gain stage G_m (G_m has a transconductance of g_{m2}, output resistance of $4R_L$, and feedback resistor of R_{F2}) and is amplified along path A (Fig. 5.8a) while the signal along the feedback path is downconverted to BB and summed at V_o, which will be zero since LO_1 and LO_3 are 180° out-of-phase with each other (the same is true for $LO_{2,4}$). After that, the amplified RF signal at V_o is immediately down-converted to BB by the 4-path I/Q passive mixers along path B (Fig. 5.8b). The BB signals at $V_{B1,I+}$ and $V_{B1,I-}$ are differential (the same is true for $V_{B1,Q+}$ and $V_{B1,Q-}$). Thus, node V_i is a virtual ground. The I/Q BB signals will be amplified and summed together again at V_o, which should be zero. This process is explicitly modeled in Fig. 5.8c. Similar to Fig. 5.4b, an ideal buffer amplifier is inserted between the front-end gain stage (with small signal transconductance g_{m1} and feedback resistor $R_{F2}/4$ for the $4G_m$ stage, as the 4 paths are parallelized) and I/Q passive mixers. When the memory effect of C_i is accounted, the 4-path SC network can be modeled at the feedback path of the $4G_m$ stage, providing double-RF filtering at both its input and output nodes.

With sufficiently large R_{F2}, the voltages (i.e., the circuit states) sampling at C_i are independent [19]. Around the clock frequency, in the steady state, the BB voltages sampling at C_i are $\upsilon_{Ci}(t)$, $j\upsilon_{Ci}(t)$, $-\upsilon_{Ci}(t)$ and $-j\upsilon_{Ci}(t)$ respectively for $LO_{1\text{-}4}$. When LO_1 is high, linear analysis shows the following state-space description,

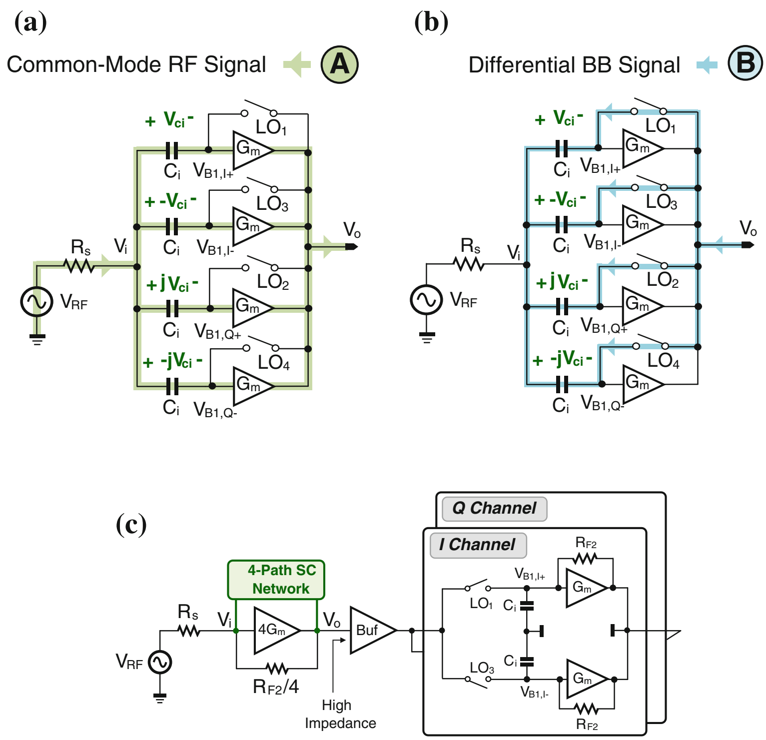

Fig. 5.8 **a** AC-coupled 4-path tunable receiver and its operation for RF signal, **b** BB signals and **c** its functional view to model the gain response

$$
\begin{cases}
\frac{C_i d\upsilon_{Ci}(t)}{dt} = \frac{\upsilon_o(t)}{R_L} + (\upsilon_{B1,I+}(t) + \upsilon_{B1,I-}(t) + \upsilon_{B1,Q+}(t) \\
\quad + \upsilon_{B1,Q-}(t))g_{m2} \\
\frac{\upsilon_{RF}(t) - \upsilon_i(t)}{R_S} = \frac{C_i d\upsilon_{Ci}(t)}{dt} \\
\upsilon_i(t) = \upsilon_{Ci}(t) + \upsilon_o(t) + R_{sw}\frac{C_i d\upsilon_{Ci}(t)}{dt} \\
\upsilon_i(t) - \upsilon_{B1,I+}(t) = \upsilon_{Ci}(t) \\
\upsilon_i(t) - \upsilon_{B1,I-}(t) = -\upsilon_{Ci}(t) \\
\upsilon_i(t) - \upsilon_{B1,Q+}(t) = j\upsilon_{Ci}(t) \\
\upsilon_i(t) - \upsilon_{B1,Q-}(t) = -j\upsilon_{Ci}(t).
\end{cases}
\tag{5.11}
$$

Simplifying (5.11), the same equation as in (5.1) is obtained, with $R_{F1} = \infty$ for R_1 and R_2. When LO_1 is low, it is in the hold mode, which can be described by (5.4). Thus, the same BB voltages $V_{B1,I\pm}$ ($V_{B1,Q\pm}$) as in GB-SC are expected. For the RF voltage at V_o, it can be evaluated by (5.10), rendering the same RF voltage gain as in Fig. 5.2. For the BB NTF from G_m, R_{sw}, R_s and R_{F2}, they are also similar to those of Fig. 5.2.

If R_{F2} is small, the voltage sampling at C_i during each LO cycle will be leaked to the ground through R_{F2}, or coupled with other states at the output V_o. The effect of charge leakage or sharing will decrease both the BB and RF gains. In the proposed gain-boosted SC network, however, there is no such a problem since the charge stored at the capacitors is constant. Thus, this architecture has smaller gain than the gain-boosted N-path SC network under a finite feedback resistor with all other parameters unchanged. In a similar way, the AC-coupled N-path tunable receiver blocks the DC response, since at DC the charge stored at the capacitors C_i has infinite time to disappear.

5.3.3 *Function-Reuse Receiver Embedding a Gain-Boosted N-Path SC Network*

Unlike the AC-coupled N-path tunable LNA, the proposed function-reuse receiver with a gain-boosted 4-path SC network (Fig. 5.9a) separates the output of each gain

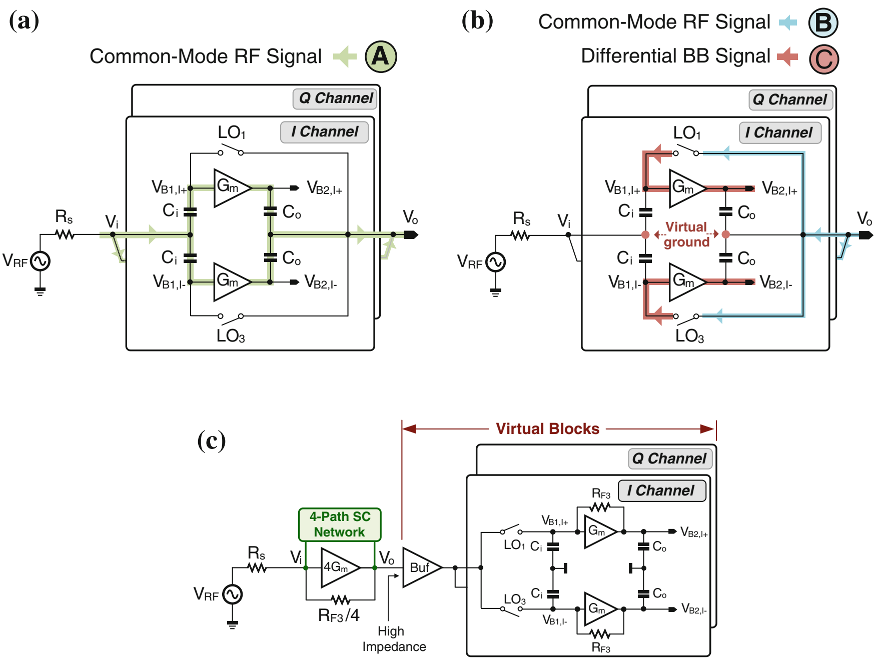

Fig. 5.9 **a** Function-reuse receiver embedding a gain-boosted 4-path SC network and its operation for RF signal, **b** BB signals and **c** its functional view to model the gain response. For simplicity, the front-end gain stage $4G_m$ and its 4-path SC network follow the structure of Fig. 4b

stage G_m (G_m has a transconductance of g_{m3}, output resistance of $4R_L$, and feedback resistor of R_{F3}) with capacitor C_o that is an open circuit at BB. The I/Q BB signals at $V_{B1,I\pm}$ and $V_{B1,Q\pm}$ are further amplified along the Path C (Fig. 5.9b) by each G_m stage. With the memory effect of the capacitors, the functional view of the gain response is shown in Fig. 5.9c. In order to achieve current-reuse between the RF LNA and BB amplifiers without increasing the supply, the circuit published in [10] with an active mixer has a similar function. However, the BB NF behavior and the RF filtering behavior are different from the N-path passive mixer applied here that is at the feedback path. For the BB amplifiers, it is one G_m with one R_{F3}, balancing the BB gain and OB-IIP3. After considering that the BB amplifiers have been absorbed in the LNA, the I/Q passive mixers and capacitors absorbed by the 4-path SC network, the blocks after the LNA can be assumed virtual. These virtual blocks reduce the power, area and NF. Similar to the AC-coupled N-path tunable LNA, with a relative small R_{F3}, the voltage sampling at C_i in different phases will either leak to the ground, or couple with each other, lowering the BB and RF gains.

To validate the above analysis, the gain and noise performances under two sets of R_{F3} are simulated. Here, the virtual blocks in Fig. 5.9c are implemented with physical transistors and capacitors for the BB amplifiers and the mixers while the buffer is ideal. Thus, the power of the modeled receiver is at least 2 × larger than the proposed receiver. For the IB BB gain at $V_{B2,I\pm}$ ($V_{B2,Q\pm}$) between the proposed function-reuse receiver and its functional view, the difference is only 1 dB at a large R_{F3} of 150 kΩ (Fig. 5.10a). For a small R_{F3}, the gain error goes up to 2 dB (Fig. 5.10b), which is due to the gain difference between the model of the N-path tunable LNA (Fig. 5.9c) and the implementation of the function-reuse receiver that has AC-coupling. For the NF difference (ΔNF), with a large (small) R_{F3}, it is ~0.8 dB (3.5 dB) as compared in Fig. 5.11a, b. This is due to the lower gain at the LNA's output, forcing the input-referred noise from the downconversion passive mixers and the BB amplifiers to increase with a small R_{F3}. Either with a small or large R_{F3}, it is noteworthy that the variation of BB NF is small (i.e. for R_{F3} = 20 kΩ it is 3.6 dB while for R_{F3} = 150 kΩ it is 3.4 dB), because the BB NTF has a weak relation with R_{F3}. It also indicates that the BB NTF is weakly related with the

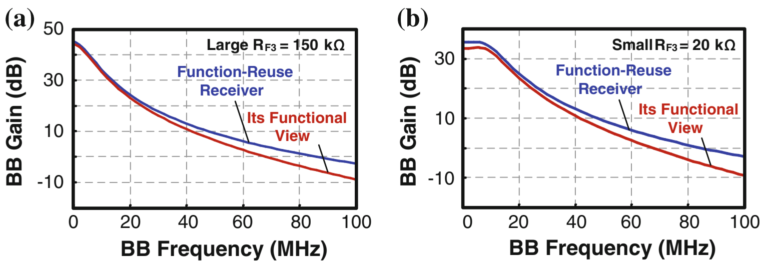

Fig. 5.10 Simulated BB gain response of the function-reuse receiver and its functional view with **a** a large R_{F3} and **b** a small R_{F3}

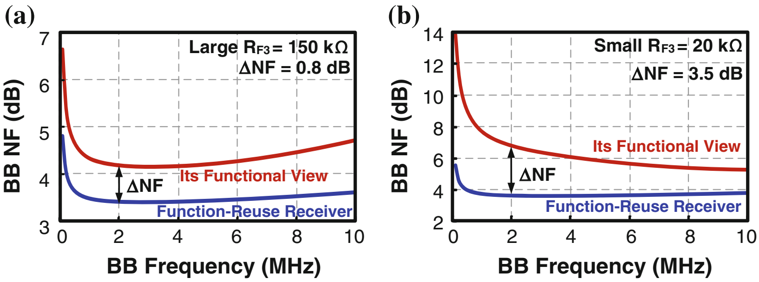

Fig. 5.11 Simulated BB NF of the function-reuse receiver and its functional view with **a** a large R_{F3} and **b** a small R_{F3}

gain at the LNA's output, which is dissimilar to the usual receiver where the NF should be small when the LNA's gain is large. Similarly, the NF at the LNA's output (now shown) can be larger than that at BB due to the different NTFs. The BB gain and the output noise at $V_{B2,I\pm}$ ($V_{B2,Q\pm}$) are further discussed in Appendix B.

For the RF gain at V_o, the simulations results are shown in Fig. 5.12a for the three realizations. With relatively small feedback resistors R_{F1} = 5 kΩ,

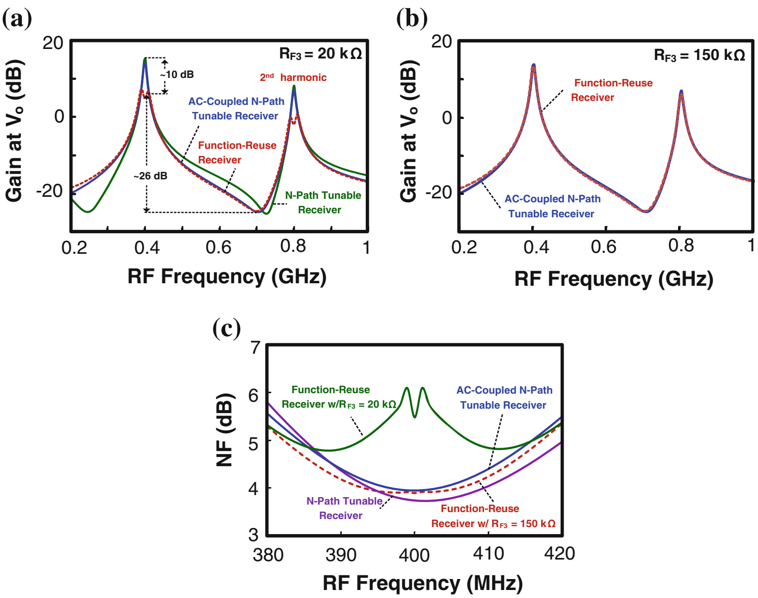

Fig. 5.12 Simulated **a**, **b** RF gain responses at V_O and **c** RF NF at V_O for the three architectures: 4-path tunable receiver, AC-coupled 4-path tunable receiver and function-reuse receiver with a gain-boosted 4-path SC network. The simulation parameters are R_L = 800 Ω, Rs = 50 Ω, $g_{m1} = 4g_{m2} = 4g_{m3}$ = 20.55 mS, C_i = 12.5 pF, f_s = 400 MHz, R_{F1} = 5 kΩ and R_{F2} = 20 kΩ

$R_{F2} = R_{F3} = 20$ kΩ, the function-reuse receiver has about 10 dB smaller IB gain than the other two. Also, there is a gain response appearing at the 2nd harmonic, which is due to the single-ended realization. The IB gain loss of the function-reuse receiver can be compensated by increasing R_{F3} from 20 to 150 kΩ, with all other parameters unchanged. The corresponding RF gain responses are plotted in Fig. 5.12b. All results are consistent to each other (and this is also true for the BB gain). The NFs at the LNA's output V_o are plotted in Fig. 5.12c. With a small $R_{F1\text{-}3}$, the RF NF of the function-reuse receiver is higher due to a lower IB gain (the RF NF is also much higher than the BB NF, as shown in Fig. 5.11b). However, with a large R_{F3}, the RF NF for the three architectures is almost equal since they have similar RF and BB gains as shown in Fig. 5.12a, b. From Figs. 5.11 and 5.12, it can be conclude that, although the RF gain of the function-reuse receiver has ~10 dB difference, the difference in the BB NF is small (0.2 dB). However, for the functional view model, the BB NF has about 2-dB difference. The NTF from the RF input to the LNA's output V_o can be derived similarly to [11] by LPTV analysis.

5.4 Low-Voltage Current-Reuse VCO-Filter

In order to further optimize the power, the VCO is designed to current-reuse with the BB complex low-IF filter (Fig. 5.13). The negative transconductor of the VCO is divided into multiple M_v cells. The aim is to distribute the bias current of the VCO to all BB gain stages (A_1, A_2…A_{18}) that implement the BB filter. For the VCO, M_V operates at the frequency of $2f_s$ or $4f_s$ for a div-by-2 or div-by-4 circuit. Thus, the VCO signal leaked to the source nodes of M_V ($V_{F1,I+}$, $V_{F1,I-}$) is pushed to very high frequencies (4 f_s or 8 f_s) and can be easily filtered by the BB capacitors. For the filter's gain stages such as A_1, M_b (g_{Mb}) is loaded by an impedance of ~$1/2g_{Mv}$ when L_p can be considered as a short circuit at BB. Thus, A_1 has a ratio-based voltage gain of roughly g_{Mb}/g_{Mv}, or as given by $4Tg_{Mb}/G_{mT}$, where G_{mT} is the total transconductance for the VCO tank. The latter shows how the distribution factor T can enlarge the BB gain, but is a tradeoff with its input-referred noise and can add more layout parasitics to $V_{vcop,n}$ (i.e., narrower VCO's tuning range). The –R cell using cross-coupled transistors is added at $V_{F1,I+}$ and $V_{F1,I-}$ to boost the BB gain without loss of voltage headroom. For the BB complex poles, $A_{2,5}$ and C_{f1} determine the real part while $A_{3,6}$ and C_{f1} yield the imaginary part. There are 3 similar stages cascaded for higher channel selectivity and image rejection ratio (IRR). R_{blk} and C_{blk} were added to avoid the large input capacitance of $A_{1,4}$ from degrading the gain of the front-end.

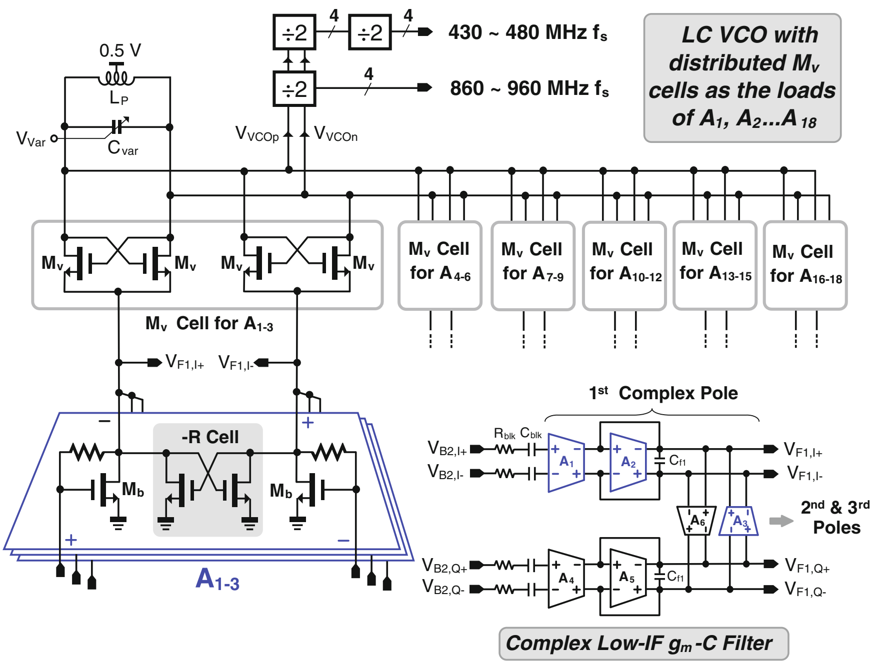

Fig. 5.13 Proposed low-voltage current-reuse VCO-filter

5.5 Experimental Results

Two versions of the multi-ISM-band sub-GHz ZigBee receiver were fabricated in 65-nm CMOS (Fig. 5.14) and optimized with a single 0.5-V supply. With (without) the LC tank for the VCO, the die area is 0.2 mm^2 (0.1 mm^2). Since the measurement results of both are similar, only those measured with VCO in Fig. 5.15a–d are reported here. From 433 to 960 MHz, the measured BB gain is 50 ± 2 dB. Following the linearity test profile of [20], two tones at [f_s + 12 MHz, f_s + 22 MHz] are applied, measuring an OB-IIP3 of –20.5 ± 1.5 dBm at the maximum gain. The IRR is 20.5 ± 0.5 dB due to the low-Q of the VCO-filter. The IIP3 is mainly limited by the VCO-filter. The measured NF is 8.1 ± 0.6 dB. Since the VCO is current-reuse with the filter, it is interesting to study its phase noise with the BB signal amplitude. For negligible phase noise degradation, the BB signal swing should be <60 mV_{pp}, which can be managed by variable gain control. If a 60-mV_{pp} BB signal is insufficient for demodulation, a simple gain stage (e.g., inverter amplifier) can be added after the filter to enlarge the gain and output swing. The total power of the receiver is 1.15 mW (0.3 mW for the LNA + BB amplifiers and 0.65 mW for VCO-filter and 0.2 mW for the divider), while the phase noise is –117.4 ± 1.7 dBc/Hz at 3.5-MHz frequency offset. The S_{11} is below –8 dB across the

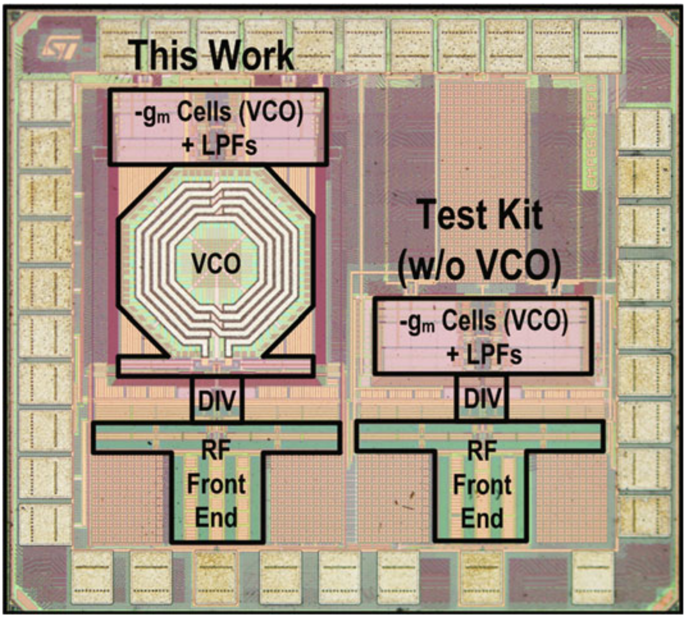

Fig. 5.14 Chip micrograph of the function-reuse receiver with a LC-tank for the VCO (*left*) and without it (*right*)

whole band. The asymmetric IF response shows 24-dB (41-dB) rejection at the adjacent (alternate) channel.

To study the RF filtering behavior, the P_{1dB} and blocker NF are measured. For the in-band signal, the P_{1dB} is –55 dBm while with a frequency offset frequency of 20 MHz, it increases to –35 dBm, which is mainly due to the double-RF filtering (Fig. 5.16a). For an offset frequency of 60 MHz, the P_{1dB} is –20 dBm, limited by the current-reuse VCO-filter. For the blocker NF, with a single tone at 50 MHz, the blocker NF is almost unchanged for the blocker ≤35 dBm. With a blocker power of –20 dBm, the NF is increased to ~14 dB (Fig. 5.16b).

The chip summary and performance benchmarks are given in Table 5.1, where [15] and [20] are current-reuse architectures while [14] is the classical cascade architecture with ULV supply for energy harvesting. For this work, the results measured under an external LO are also included for completeness. In both cases, this work succeeds in advancing the power and area efficiencies with multi-band convergence, while achieving tunable S_{11} with zero external components. Particularly, when comparing with the most recent ULV design [14], this work saves more than 10× of area while supporting multi-band operation with zero external components.

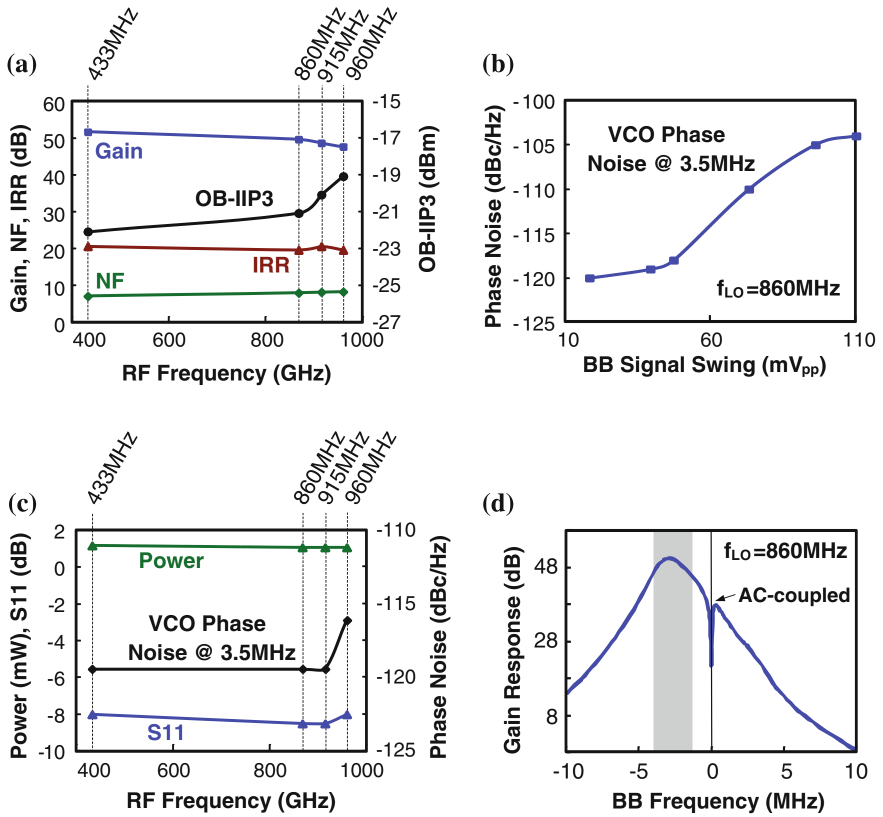

Fig. 5.15 Measured key performance metrics: **a** gain, NF, IRR and OB-IIP3. **b** VCO phase noise versus BB signal swing. **c** S_{11}, power and VCO phase @ 3.5-MHz offset. **d** BB complex gain response centered at –2-MHz IF

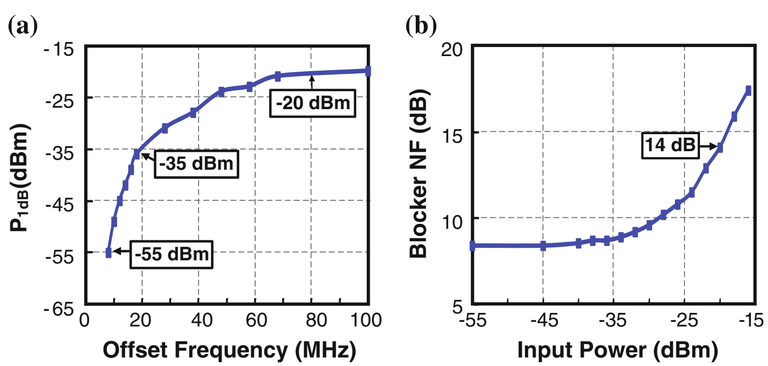

Fig. 5.16 Measured **a** P1 dB versus input offset frequency and **b** blocker NF versus input power

Table 5.1 Performance summary and benchmark with the state-of-the-art

	This work	ISSCC'13 [15] (w/VCO)	ISSCC'13 [14]	JSSC'10 [20]
Application	**433/860/915/960 MHz (ZigBee/IEEE802.15.4c/d)**	2.4 GHz (ZigBee/IEEE 802.15.4)	2.4 GHz (Energy Harvesting)	2.4 GHz (ZigBee/IEEE 802.15.4)
Architecture	Function-reuse RF front-end + N-path tunable LNA + Current-reuse VCO-filter	Blixer + Hybrid Filter + Passive RC-CR Filter +LC VCO	CG LNA + Passive mixers + N-Path SC IF filter + LC VCO	LNA-Mixer-VCO merged cell + Complex filter
BB Filter	3 Complex poles	1 Biquad, 4 Complex poles	2 Real poles	3 Complex poles
Input matching technique	**On-chip N-path SC (tunable by LO, high Q)**	On-chip LC (fixed, low Q)	Off-chip LC (fixed, low Q)	Off-chip LC (fixed, high Q)
External components	**zero**	zero	2 Caps, 1 Inductor	1 Caps, 1 Inductor
Input matching BW and tunability	**433–960 MHz (tunable by LO)**	2.25–3.55 GHz (fixed)	~2–2.6 GHz (fixed)	2.3–2.6 GHz (fixed)
Active area (mm^2)	**0.2 (*0.1)**	0.3	2.5	0.35
Power (mW) @V_{DD}	**1.15 ± 0.05 @ 0.5 V**	2.7 @ 0.6/1.2 V	1.6 @ 0.3 V	3.6 @ 1.2 V
Gain (dB)	50 ± 2 ([1]51 ± 3)	55	83	75
NF (dB)	8.1 ± 0.6 ([1]8 ± 1)	9	6.1	9
OB-IIP3 (dBm)	–20.5 ± 1.5 ([1]–23 ± 1)	–6	–21.5	–12.5
IRR (dB)	20.5 ± 0.5 ([1]21 ± 0.5)	28	N/A	35
VCO phase noise (dBc/Hz)	–117.4 ± 1.7 @ 3.5 MHz	–115 @ 3.5 MHz	–112 @ 1 MHz	–116 @ 3.5 MHz
Technology	65 nm CMOS	65 nm CMOS	65 nm CMOS	90 nm CMOS

[1]Results measured from the test kit that has no VCO

5.6 Conclusions

A function-reuse receiver embedding a gain-boosted N-path SC network has been proposed to realize a sub-GHz multi-ISM-band ULP ZigBee radio at a single 0.5-V supply. The featured improvements are fourfold: (1) unlike the usual receiver concept that is based on cascade of blocks, this receiver reuses one set of amplifiers for concurrent RF and BB amplification by arranging an N-path SC network in the feedback loop. Interestingly, this scheme decouples the BB STF (or NTF) from its RF STF (or NTF), allowing a lower BB NTF possible while saving power and area. This new receiver concept is good foundation for a deeper exploration of the topic. (2) The output BB NTF due to R_{sw} and R_F are greatly reduced, lowering the required size of the mixer switches and LO power. (3) Double-RF filtering is performed with one N-path SC network, improving the OB-IIP3 and tolerability of OB blockers. (4) A current-reuse VCO-filter further optimizes the power at just 0.5 V. All of these characteristics affirm the receiver as a potential candidate for emerging ULP radios of IoT applications that should support multi-band operation, being friendly to a single ULV supply allowing energy harvesting, and compact enough to save cost in nanoscale CMOS.

Appendix A: Output-Noise PSD at BB for the N-Path Tunable Receiver

The derivation of the output-noise PSD at BB due to R_S, $4G_m$, R_{sw} and R_{F1} is presented here. The model used to obtain the NTFs is shown in Fig. 5.17. For all output-noise PSDs, there are two parts: one is the direct transfer from input RF to BB, while another is from harmonics folding noise. For the latter, increasing the path number N can reduce such contribution. The differential output-noise PSD for

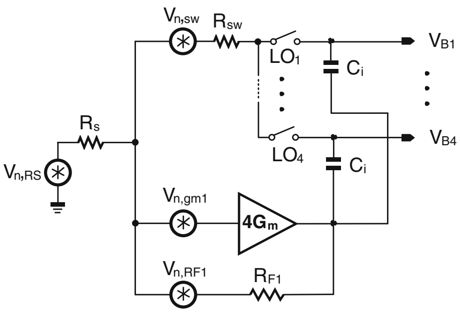

Fig. 5.17 Equivalent noise model of the N-path tunable receiver (Fig. 5.3d) for BB output-noise PSD calculation and simulation. N = 4 is used. The noise sources g_{m1} and R_{F1} from the $4G_m$ are explicitly shown

R_s, $4G_m$, R_{sw} and R_{F1} with $\overline{V_{n,R_S}^2} = 4KTR_s$, $\overline{V_{n,4Gm}^2} = {}^{4KT}/_{g_{m1}}$, $\overline{V_{n,Rsw}^2} = 4KTR_{sw}$ and $\overline{V_{n,R_{F1}}^2} = 4KTR_{F1}$ are given as (A.1)–(A.4),

$$\overline{V_{n,out,R_S}^2} = \left\{ \underbrace{\left|H_{-1,R_S}(j\omega)V_{n,R_S}(j\omega+\omega_s)\right|^2}_{\text{Part A}} + \underbrace{\sum_{n=-\infty,n\neq-1}^{\infty} \left|H_{n,R_S}(j\omega)V_{n,R_S}(j(\omega-n\omega_s))\right|^2}_{\text{Part B}} \right\} \times 4 \tag{A.1}$$

$$\overline{V_{n,out,4Gm}^2} = \left\{ \underbrace{\left|H_{-1,4Gm}(j\omega)V_{n,4Gm}(j\omega+\omega_s)\right|^2}_{\text{Part A}} + \underbrace{\sum_{n=-\infty,n\neq-1}^{\infty} \left|H_{n,4Gm}(j\omega)V_{n,4Gm}(j(\omega-n\omega_s))\right|^2}_{\text{Part B}} \right\} \times 4 \tag{A.2}$$

$$\overline{V_{n,out,R_{sw}}^2} = \left\{ \underbrace{\left|H_{-1,R_{sw}}(j\omega)V_{n,R_{sw}}(j\omega+\omega_s)\right|^2}_{\text{Part A}} + \underbrace{\sum_{n=-\infty,n\neq-1}^{\infty} \left|H_{n,R_{sw}}(j\omega)V_{n,R_{sw}}(j(\omega-n\omega_s))\right|^2}_{\text{Part B}} \right\} \times 4 \tag{A.3}$$

$$\overline{V_{n,out,R_{F1}}^2} = \left\{ \underbrace{\left|H_{-1,R_{F1}}(j\omega)V_{n,R_{F1}}(j\omega+\omega_s)\right|^2}_{\text{Part A}} + \underbrace{\sum_{n=-\infty,n\neq-1}^{\infty} \left|H_{n,R_{F1}}(j\omega)V_{n,R_{F1}}(j(\omega-n\omega_s))\right|^2}_{\text{Part B}} \right\} \times 4 \tag{A.4}$$

For the above NTFs, the even order terms (including zero) of n are excluded. The single-ended HTFs for R_S, $4G_m$, R_{sw} and R_{F1} are $H_{n,R_S}(j\omega), H_{n,4Gm}(j\omega)$, $H_{n,R_{sw}}(j\omega)$ and $H_{n,R_{F1}}(j\omega)$, respectively. Further details were covered in [11].

Appendix B: Derivation and Modeling of BB Gain and Output Noise for the Function-Reuse Receiver

When considering the memory effect of the capacitor C_i and C_o with R_{F3} sufficiently large, the voltages (i.e., the circuit states) at C_i are independent [19]. In the steady-state, around the clock frequency, the voltages sampling at C_i are $\upsilon_{Ci}(t)$, $j\upsilon_{Ci}(t)$, $-\upsilon_{Ci}(t)$, $-j\upsilon_{Ci}(t)$, while the voltage sampling at C_o is $\upsilon_{CO}(t)$, $j\upsilon_{CO}(t)$, $-\upsilon_{CO}(t)$,

$-j\upsilon_{CO}(t)$, for LO_{1-4}, respectively. When LO_1 is high (K = 1), linear analysis shows the following state-space description for capacitor C_i,

$$\begin{cases} \begin{cases} \dfrac{C_i d\upsilon_{Ci}(t)}{dt} = \big(\upsilon_{B1,I+}(t) + \upsilon_{B1,I-}(t) + \upsilon_{B1,Q+}(t) + \upsilon_{B1,Q-}(t)\big) g_{m3} \\ \qquad\qquad +\upsilon_{B1,Q-}(t)\big)g_{m3} \\ \qquad + \big(\upsilon_{B2,I+}(t) + \upsilon_{B2,I-}(t) + \upsilon_{B2,Q+}(t)\big) \\ \qquad\qquad +\upsilon_{B2,Q-}(t)\big) \frac{1}{4R_L} \end{cases} \\ \dfrac{\upsilon_{RF}(t) - \upsilon_{Ci}(t)}{R_s} = \dfrac{C_i d\upsilon(t)}{dt} \\ \upsilon_i(t) = \upsilon_{Ci}(t) + \upsilon_o(t) + R_{sw}\dfrac{C_i d\upsilon(t)}{dt} \\ \upsilon_i(t) - \upsilon_{B1,I+}(t) = \upsilon_{Ci}(t) \\ \upsilon_i(t) - \upsilon_{B1,I-}(t) = -\upsilon_{Ci}(t) \\ \upsilon_i(t) - \upsilon_{B1,Q+}(t) = j\upsilon_{Ci}(t) \\ \upsilon_i(t) - \upsilon_{B1,Q-}(t) = -j\upsilon_{Ci}(t) \\ \upsilon_o(t) + \upsilon_{co}(t) = \upsilon_{B2,I+}(t) \\ \upsilon_o(t) - \upsilon_{co}(t) = \upsilon_{B2,I-}(t) \\ \upsilon_o(t) + j\upsilon_{co}(t) = \upsilon_{B2,Q+}(t) \\ \upsilon_o(t) - j\upsilon_{co}(t) = \upsilon_{B2,Q-}(t) \end{cases} \tag{B.1}$$

Equation (B.1) can be simplified similar to (5.1). Likewise, when LO_1 is low, it can be described by (5.4). Thus, it has the same BB HTFs as in gain-boosted N-path SC network [shown also in (5.8)].

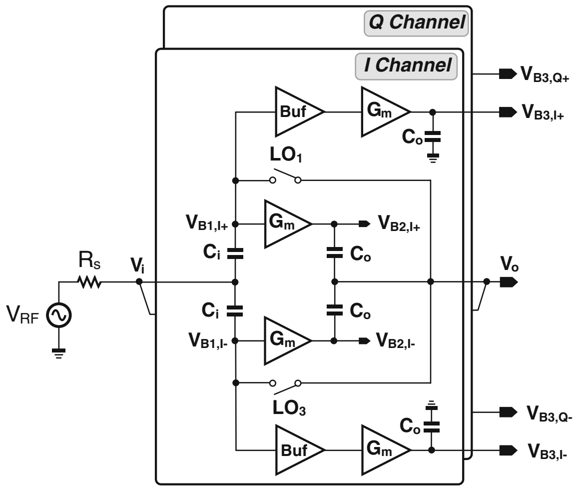

Fig. 5.18 Schematic to model the BB NF of the functional-reuse receiver at $V_{B2,I\pm}$

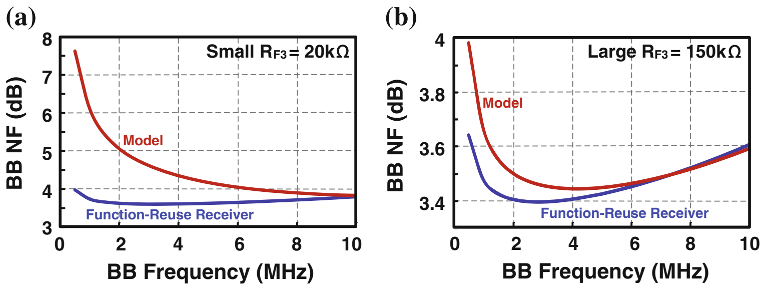

Fig. 5.19 Simulated BB NF from the model and functional-reuse receiver with **a** a small R_{F3} and **b** a larger R_{F3}

The BB NF at $V_{B2,I\pm}$ ($V_{B2,Q\pm}$) is approximately modeled in Fig. 5.18. The BB output noise at $V_{B1,I\pm}$ ($V_{B1,Q\pm}$) are further amplified by two separate BB amplifiers, while in the function-reuse receiver they are amplified by the same BB amplifiers. From simulations, with a large R_{F3}, the model has a good accuracy, while for a small R_{F3}, the error increases for the low-frequency part. This is because the BB gain at $V_{B1,I\pm}$ ($V_{B1,Q\pm}$) gets smaller under a small R_{F3}, and the independent noise sources from the model's G_m contribute additional noise (Fig. 5.19a, b). The function-reuse receiver has a smaller NF and requires lower power than the separated G_m situation. For the BB gain, this model has a high accuracy (not shown).

References

1. J.A. Stankovic, Research directions for the internet of things. IEEE Int. Things J. **1**(1), 3–9 (2014)
2. A. Zanella, N. Bui, A. Castellani, L. Vangelista, M. Zorzi, Internet of things for smart cities. IEEE Int. Things J. **1**(1), 22–32 (2014)
3. Pike Research on Smart Cities. [Online]. http://www.pikeresearch.com/research/smart-cities
4. J. Sinderen, G. Jong, F. Leong, et al., Wideband UHF ISM-Band transceiver supporting multichannel reception and DSSS modulation. ISSCC Dig. Tech. Papers, pp. 454–455, Feb. 2013
5. A. Wong, M. Dawkins, G. Devita, et al., A 1 V 5 mA multimode IEEE 802.15.6/bluetooth low-energy WBAN transceiver for biotelemetry applications. ISSCC Dig. Tech. Papers, pp. 300–301, Feb. 2012
6. B.W. Cook, A. Berny, A. Molnar, S. Lanzisera, K. Pister, Low-power, 2.4-GHz transceiver with passive RX front-end and 400-mV supply. IEEE J. Solid-State Circ. **41**, 2767–2775 (2006)
7. Z. Lin, P.-I. Mak, R.P. Martins, A 0.14-mm^2 1.4-mW 59.4-dB-SFDR 2.4 GHz ZigBee/WPAN receiver exploiting a 'Split-LNTA + 50 % LO' topology in 65-nm CMOS. IEEE Trans. Microw. Theory Techn. **62**(7), 1525–1534 (2014)
8. A. Mirzaei, H. Darabi, Analysis of imperfections on performance of 4-phase passive-mixer-based high-Q bandpass filters in SAW-less receivers. IEEE Trans. Circ. Syst. I, Reg. Pap. **58**(5), 879–892 (2011)

9. A. Ghaffari, E. Klumperink, M. Soer, B. Nauta, Tunable High-Q N-path band-pass filters: modeling and verification. IEEE J. Solid-State Circ. **46**(5), 998–1010 (2011)
10. J. Han, R. Gharpurey, Recursive receiver down-converters with multiband feedback and gain-reuse. IEEE J. Solid-State Circ. **43**, 1119–1131 (2008)
11. Z. Lin, P.-I. Mak, R.P. Martins, Analysis and modeling of a gain-boosted N-path switched-capacitor bandpass filter. IEEE Trans. Circ. Syst. I, Reg. Pap. **9**, 2560–2568 (2014)
12. Z. Lin, P.-I. Mak, R. P. Martins, A 0.5 V 1.15 mW 0.2 mm^2 Sub-GHz ZigBee receiver supporting 433/860/915/960 MHz ISM bands with zero external components. ISSCC Dig. Tech. Papers, pp. 164–165, Feb. 2014
13. F. Zhang, Y. Miyahara, B. Otis, Design of a 300-mV 2.4-GHz receiver using transformer-coupled techniques. IEEE J. Solid-State Circ. **48**, 3190–3205 (2013)
14. F. Zhang, K. Wang, J. Koo, Y. Miyahara, B. Otis, A 1.6 mW 300 mV supply 2.4-GHz receiver with –94 dBm sensitivity for energy-harvesting applications. ISSCC Dig. Tech. Papers, pp. 456–457, Feb. 2013
15. Z. Lin, P.-I. Mak, R.P. Martins, A 1.7 mW 0.22 mm^2 2.4 GHz ZigBee RX exploiting a current-reuse blixer + Hybrid filter topology in 65 nm CMOS. ISSCC Dig. Tech. Papers, pp. 448–449, Feb. 2013
16. Z. Lin, P.-I. Mak, R.P. Martins, A 2.4-GHz ZigBee receiver exploiting an RF-to-BB-current-reuse blixer + hybrid filter toploly in 65-nm CMOS. IEEE J. Solid-State Circ. **49**, 1333–1344 (2014)
17. C. Andrews, A. Molnar, Implications of passive mixer transparency for impedance matching and noise figure in passive mixer-first receivers. IEEE Trans. Circ. Syst. I, Reg. Pap. **57**, 3092–3103 (2010)
18. C. Andrews, A. Molnar, A passive mixer-first receiver with digitally controlled and widely tunable RF interface. IEEE J. Solid-State Circ. **45**, 2696–2708 (2010)
19. M. Soer, E. Klumperink, P. de Boer, F. van Vliet, B. Nauta, Unified frequency domain analysis of switched-series-RC passive mixers and samplers. IEEE Trans. Circ. Syst. I, Reg. Pap. **57**(10), 2618–2631 (2010)
20. M. Tedeschi, A. Liscidini, R. Castello, Low-power quadrature receivers for ZigBee (IEEE 802.15.4) applications. IEEE J. Solid-State Circ. **45**, 1710–1719 (2010)

Chapter 6
Conclusion

6.1 General Conclusions

In Chap. 1, the motivations of ULP and ULC short-range radios have been studied, followed by the general definition of short-range wireless communications. Three popular short-range wireless standards for ULP and ULC applications have been briefly reviewed, and their pros and cons have been analyzed and compared. The conclusion is that for ULP applications, the RX should meet similar metrics. After that, the design considerations of ULP and ULC short-range wireless RXs were discussed, which included the supply voltage, carrier frequency and the selection of NB versus UWB. Finally, the main targets and organization of the book were presented.

In Chap. 2, a 2.4-GHz RX using a split-LNTA + 50 %-duty-cycle LO has been proposed. When there is 6-dB passive pre-gain, the split-LNTA shows only <1 dB higher NF when compared with the typical RX that uses a single-LNA + 25 %-duty-cycle LO. Thus, it should be a promising ULP architecture since the 50 %-duty-cycle I/Q LO can be implemented with a low-power two stages RC-CR network without using a power-hungry frequency divider or other logics to generate a 25 %-duty-cycle I/Q LO. Besides, a capacitive impedance-boosted technique was used to connect the passive network to the VCO tank without degrading its Q, and therefore saving the VCO's power. The RX fabricated in 65-nm CMOS exhibits 32-dB voltage gain, 8.8-dB NF and −7-dBm OB IIP3 that correspond to 59.4-dB spurious-free dynamic range. The VCO measures −111.4-dBc phase noise at 3. 5-MHz offset. The achieved power (1.4 mW) and area (0.14 mm^2) efficiencies are favorably comparable with the state-of-the-art.

In Chap. 3, an extensive RF-to-BB current-reuse 2.4-GHz RX was described. It reuses the bias current among the RF balun-LNA, the double-balanced active mixer and the BB 3rd-order current-mode hybrid filter for channel selection.

Z. Lin et al., *Ultra-Low-Power and Ultra-Low-Cost Short-Range Wireless Receivers in Nanoscale CMOS*, Analog Circuits and Signal Processing,
DOI 10.1007/978-3-319-21524-2_6

As such, those out-of-band blockers are heavily filtered in the current mode before inducing large distortion at the output, improving OB IIP3. It also benefits the image rejection, which can be realized by a high-order passive RC-CR network instead of high-order active complex filter that is more power hungry. The high IRR relaxes the LO phase error to $\sim 4°$, saving the LO's power. Together with an LO-amplitude optimization technique, an in-band noise-shaping technique for the current-mode filter, and a low-Q tapped-capacitor pre-gain technique in the LNA input, the RX measures 8.5-dB NF, 57-dB gain and −6-dBm IIP3 out-band at 1. 7-mW power and 0.24-mm^2 die size. The S_{11}-bandwidth (<–10 dB) covers 2.25–3. 55 GHz being robust to packaging variations. Most performance metrics compare favorably with the prior art.

In Chap. 4, the analysis, modeling and design of a novel GB-BPF were described. First, the RF gain, input impedance, filter bandwidth and ultimate filter rejection were analyzed using an ideal RLC model. It was shown that both power and area efficiencies are improved when compared with the traditional passive N-path filter due to the loop gain offered by gain-boosting. Then, the R, L, and C expressions are derived with LPTV analysis. The harmonic selectivity, harmonic folding and output noise are also analyzed in the same way and verified by simulations. It was shown that the switches' noise is notched at the output, benefitting the use of small switches for the SC branch, saving the LO's power without sacrificing the selectivity. Furthermore, an intuitive equivalent circuit to model the in-band gain is given. Finally, a design example of a 4-path GB-BPF is simulated. It shows >11-dB gain, <2.3-dB NF over 0.5–2 GHz RF, and +21-dBm out-of-band IIP3 at 150-MHz offset, at just 7-mW power. The developed models backup the analysis of the ULP receiver for multi-band sub-GHz ZigBee applications in Chap. 5.

In Chap. 5, a function-reuse RX with an embedded gain-boosted N-path SC network embedded in the LNA is proposed. It realized a sub-GHz multi-ISM-band ULP ZigBee receiver at a single 0.5-V supply. Unlike the current-reuse technique in Chap. 3, the function-reuse RX can fully reuse the bias current without stacking devices and thus can be implemented at a low supply voltage. The embedded gain-boosted N-path SC network preserves all benefits of the GB-BPF that was discussed in Chap. 4. Besides, the exact expressions of STF and NTF at BB are derived following the analysis of Chap. 4. Due to the lack of intuition for such an analysis, an intuitive functional view is given to model the BB gain. Also, the BB NF and RF NF are studied by simulations, showing an interesting property of this architecture. That is, the BB NF can be smaller than the RF NF. This can be explained by considering that the BB output noise (or gain) is concurrently achieved with the RF output noise (or gain). The BB output noise due to R_{sw} (=30 Ω) and R_F (=5 kΩ) are also studied by simulations, showing that they contribute with much less noise than that of the source resistance R_s and the transconductance stage G_m. Thus, it would be possible to utilize mixer switches of small size without degrading the BB NF, saving the LO power. To further optimize the power, a low-voltage current-reuse VCO-filter is proposed. It nullifies the power of the BB complex filter. The RX measures 8.1 ± 0.6 dB NF, 50 ± 2 dB gain and—20.5 ± 1.

5 dBm out-of-band IIP3 at 1.15 ± 0.05 mW power, at 0.5 V over the four ISM bands. The VCO phase noise is –117.4 ± 1.7 dBc/Hz at 3.5-MHz offset. The 2 MHz IF gain response shows 18-dB (38-dB) rejection at the adjacent (alternate) channel. The active area is 0.2 mm^2 in 65-nm CMOS. The small area, very low supply-voltage and multi-band LO tunable matching renders this RX as a good candidate for emerging ULP and ULC short-range radios for IoT applications. It is also a promising solution for potential energy harvesting that will lead to autonomous operation.

6.2 Suggestions for Future Work

ULP and ULC radios are an interesting topic. In this book, the research on such kind of application is defined which has a stringent requirement in both power and cost. In fact, it can be extended to other kinds of radios design. Hopefully, this book will inspire more innovative ideas. Below, some suggestions are given for future work.

(1) LO generation can consume significant power and area when approaching multi-band operation. For example, if a universal ULP RX covering the 2.4 GHz and sub-GHz ISM bands is required, the VCO tuning range should be 57 % if a 2.4-GHz VCO is selected and it is followed by a div-by-4 circuit. Such a wide tuning range should consume more power than the single-band design. In fact, from area and tuning range's viewpoint, a ring oscillator should be more attractive. However, to meet the required phase noise, ULP consumption is still challenging.

(2) The proposed N-path gain-boosted receiver (Chaps. 4 and 5) still has a lot of unexplored features, even if the BB NF and RF NF can be derived by LPTV analysis, the expressions still lack of enough intuition. Thus, a quantitative proof is still missing for the BB NF that can be smaller than the RF NF. If possible, a simple expression for the BB NF and RF NF should be derived. Also, with the simple NF expression, for the given power, the NF can be easily optimized.

(3) For the gain-boosted bandpass filter, the filtering profile around the harmonic frequency is a function of R_F, R_{sw}, G_m, R_s and $R_{L.}$ This means that there are some combinations which can achieve a smaller peaking or even a notch around the harmonic frequencies. In fact, this has been proved by Matlab simulations. How these combinations affect the impedance matching, filter selectivity and NF can be further explored.

(4) For the function-reuse receiver, the BB signal and RF signal exist at the same time, how the large BB signal affects the small RF signal in terms of IIP3 still needs to be studied. Also, the parasitic capacitance from the AC-coupling capacitors at the input and output of the transconductance stages should be large, this effect should be considered into the RLC model. Although the

intuitive equivalent circuit can model the IB gain and OB rejection, the accuracy of this model should be enhanced. Thus, to accurately model this effect, the mutual coupling from each set of switches should be considered.

Index

Z. Lin et al., *Ultra-Low-Power and Ultra-Low-Cost Short-Range Wireless Receivers in Nanoscale CMOS*, Analog Circuits and Signal Processing,
DOI 10.1007/978-3-319-21524-2